

NEUTRON MEASUREMENTS AND
REACTOR ANTINEUTRINO SEARCH
WITH THE SNO+ DETECTOR IN THE WATER PHASE

by

YAN LIU

A thesis submitted to the
Department of Physics, Engineering Physics and Astronomy
in conformity with the requirements for
the degree of Doctor of Philosophy

Queen's University
Kingston, Ontario, Canada

June 2020

Copyright © Yan Liu, 2020

Abstract

The SNO+ experiment is a large-scale liquid scintillator neutrino experiment with a wide range of physics objectives. SNO+ has adopted a staged approach where the detector was first filled with ultra-pure water before substituting with liquid scintillator and the target isotope ^{130}Te for neutrinoless double beta decay. During the SNO+ water phase, an $^{241}\text{Am}^9\text{Be}$ source is deployed across the detector volume to calibrate the detector's energy response and its response to neutrons. The $^{241}\text{Am}^9\text{Be}$ source emits a unique coincidence signal with the prompt event being a 4.4 MeV γ and the delayed a neutron capture signal (2.2 MeV γ).

A novel, minimalistic, statistical analysis of the $^{241}\text{Am}^9\text{Be}$ calibration data was designed and used to measure the capture time constant τ , capture cross-section $\sigma_{H,t}$, and the neutron detection efficiency E_{center} at the center of the detector:

$$\begin{aligned}\tau &= 202.35 \pm 0.42 \text{ (stat.) } {}^{+0.38}_{-0.31} \text{ (syst.) } \mu\text{s}, \\ \sigma_{H,t} &= 336.3 {}^{+1.2}_{-1.5} \text{ mb}, \\ E_{\text{center}} &= (50.8 \pm 0.6)\%.\end{aligned}\tag{1}$$

Additionally, with the help of Monte Carlo simulations, a volume-weighted neutron detection efficiency across the detector is evaluated to be $E_{\text{detector}} = (46.5 \pm 0.5 \text{ (stat. only)})\%$. The simulation is also central to an energy calibration using the

4.4 MeV γ to measure the energy resolution and energy scale of the detector.

Finally, with ~ 115 days of early water data, an upper limit, $\hat{\Phi}_{\bar{\nu}_e, \text{ult}} = (1.76 \pm 0.29) \times 10^6 \bar{\nu}/(\text{cm}^2 \cdot \text{s})$, on the reactor antineutrino flux for SNO+ is obtained using a maximum likelihood approach. The limit is about a factor of 9 higher than the expected signal in SNO+, which can be calculated using available reactor output power data.

Acknowledgements

It would not be prudent to say that I can make due acknowledgement to all the assistance that I have received throughout my graduate studies; that list would have been too long. Nonetheless, I would like to thank everyone that I had the pleasure to work with.

I own sincere thanks to my supervisor, Prof. Mark Chen, for the insightful guidance, the plentiful resources, and most importantly the precious freedom to explore my research interests.

Alex Wright introduced me to SNO+ and was super patient in answering all my questions. Peter Skensved has always amazed me for his hospitality. I can not say how much I have enjoyed the endless drives to and from Sudbury with him, countless arguments in his office and of course things not-to-be-mentioned in the DCR. Sofia Andringa has been instrumental to my research on the AmBe calibration and reactor antineutrino data analyses.

I extend my appreciation to the Queen's SNO+ group, Ryan, Szymon, Lianpeng, Xin, Satoko, Ted, Ian, Caleb, Liz, Ben, Ingrida, Mark A., and Brian for making my graduate study memorable and time in Kingston joyful. I would also like to thank Brian, Sandra, and Jake for helping my projects as summer students. In particular, work done by Brian and Jake has directly contributed to this thesis.

Christine and Erica were very helpful for my frequent travels and long-term stay in Sudbury. I am grateful for many people who offered me rides from Kingston to Sudbury as well as within Sudbury. Thanks to Dimpal, Patrick, Andy, Matt, Zack, and many others that have made life in Sudbury delightful.

I want to highlight my sincere gratitude to Jose and Sofia, who invited me to Lisbon as a visiting scholar. Thanks also go to Valentina, Gesende, Fernando, Stefan, and Ana Sofia for making living in Lisbon one of my favorite memories.

I have had the pleasure to work with many wonderful people in the SNO+ collaboration. I would like to thank Jose, Simon, Carsten, Aksel, Ryan and Peter from the calibration group, Sofia, Kalpana, Logan, and Stefan from the antineutrino group, Gersende, Lisa, Erica and Stefan from the run selection group for their constant support of my work.

I would like to pay my most sincere appreciation to Elaine Yuan, without whom this thesis would be impossible, both figuratively and literally. For without the overnight drive to Sudbury after landing in the Toronto airport, the AmBe calibration that this entire thesis based on would not have taken place. Thank you also for proofreading part of the thesis and providing a sheltered place in HK for me while working on the thesis during this unusual time.

Finally, I would like to thank my parents for unconditional support for my work and life. You are the best parents I can ever hope for.

Statement of Originality

I certify that to my best knowledge, the content in this thesis is my own and has not previously been submitted to any other institute for any purpose. All the work presented here is the product of my own work and any received assistance or used sources have been properly acknowledged.

Statement of Contribution

The results and discussion presented in Chapter 1 are a review of the literature and experimental results available at the time of writing.

Chapter 2 presents an overview of the SNO+ detector, which is inherited from the SNO experiment. The author has contributed to the general construction of the liquid scintillator purification plant and the Telluric Acid purification plant through frequent weekly travels and several months of on-site work. The author has also contributed to the testing and refurbishing of SNO PMTs. The author has been an active member of the detector calibration group and played an important role in the commissioning of the calibration source manipulator system, and the laserball, ^{16}N , and ^8Li calibrations.

The author has played a central role in the $^{241}\text{Am}^8\text{Be}$ calibration. The author was a main proponent of the $^{241}\text{Am}^8\text{Be}$ calibration in the SNO+ water phase, designed and fabricated the new encapsulation, and coordinated the $^{241}\text{Am}^8\text{Be}$ source deployments. B. Krar provided AutoCAD help and C. Hearns did the machinery work. The author was also the first to propose the external deployment of the $^{241}\text{Am}^8\text{Be}$ source and carried out the feasibility study.

The idea of the minimalistic analysis was first conceived by F. Barao, but the fit function and main body of the analysis were derived by S. Andringa and the author.

The toy MC model and the systematic study (except for data cleaning sacrifice and temperature variation) are the sole work of the author. The idea of converting the capture time constant to the capture cross-section was first proposed by R. Svoboda.

The remainder of the thesis is the sole work of the author with the following exceptions:

RAT is the work of the SNO+ collaboration.

The trigger efficiency model was constructed by T. Kaptanoglu.

The neutron cutoff in the Monte Carlo simulations was devised by M. Nirkko.

Data for comparison with the MC was obtained by S. Andringa and the author.

The coincidence processor was written by S. Nae and S. Andringa.

The idea of how to conduct energy calibration was from M. Dunford and later improvements were made by L. Lebanowski but the author independently rewrote the whole code.

The energy spectrum of 4.4 MeV γ s used for energy calibration was derived by J. Erickson under the supervision of the author.

The dataset used for the antineutrino search was selected by the run selection (of which the author is a member) and the nucleon decay working groups. Data cleaning and live time calculation were done by the data cleaning group. Trigger threshold evaluation was performed by A. Latorre.

Contents

Abstract	i
Acknowledgements	iii
Statement of Originality	v
Statement of Contribution	vi
Contents	viii
List of Tables	xii
List of Figures	xiv
Chapter 1: Neutrino Physics	1
1.1 Neutrinos	1
1.2 The Source: Reactor Antineutrino Spectrum	3
1.3 The Propagation: Neutrino Oscillation	6
1.3.1 The PMNS Matrix	6
1.3.2 Vacuum Oscillation	8
1.3.3 Neutrino Oscillation Experiments	10
1.4 The Detection: Inverse Beta Decay	12
1.5 Reactor Antineutrino with SNO+	14
1.5.1 Reactor Antineutrinos in SNO+ Water Phase	16
1.6 Organization of the Thesis	16
Chapter 2: The SNO+ Experiment	18
2.1 Detector Overview	18
2.1.1 Staged Approach	19
2.2 Detection Principle in the Water Phase	21
2.2.1 Cherenkov Radiation	21
2.2.2 The Photomultiplier Tube	22

2.2.3	The Trigger System	24
2.3	Calibrations in the Water Phase	25
2.3.1	The Laserball Calibration	29
2.3.2	The ^{16}N Calibration	30
2.3.3	The ^8Li Calibration	31
2.3.4	ELLIE	32
2.4	Software and Data Stream	33
Chapter 3: The $^{241}\text{Am}^9\text{Be}$ Calibration		35
3.1	The $^{241}\text{Am}^9\text{Be}$ Source	35
3.2	The New Encapsulation	39
3.2.1	Design and Fabrication	39
3.2.2	Pre-deployment Tests and Cleaning	42
3.3	The Source Deployment	45
3.3.1	Internal Deployment	45
3.3.2	External Deployment	49
Chapter 4: Minimalistic $^{241}\text{Am}^9\text{Be}$ Data Analysis		53
4.1	Analysis Method	53
4.1.1	Derivation and Interpretation of the Fit Function	55
4.1.2	Validation of the Fit Function with a Toy MC Model	59
4.2	Application to a One-hour Central $^{241}\text{Am}^9\text{Be}$ Calibration Data	62
4.2.1	The Fit Result	62
4.2.2	Varying the Nhits Cuts for Prompt and Delayed Candidates	65
4.3	Application to the Global Dataset	68
4.3.1	The Neutron Capture Time Constant τ	69
4.3.2	The Neutron Detection Efficiency	71
4.4	Systematic Considerations	71
4.4.1	Systematics From the Fit Function	72
4.4.2	Data Cleaning Sacrifice	77
4.4.3	Initial Neutron Energy Spectrum	82
4.4.4	Source Encapsulation	83
4.4.5	Temperature Variations	85
4.4.6	Summary of Corrections and Uncertainties	86
4.5	Final Results	88
4.5.1	Neutron Capture Time Constant and Neutron Detection Efficiency	88
4.5.2	Thermal neutron-hydrogen capture cross-section	88
Chapter 5: The Monte Carlo Simulation for the $^{241}\text{Am}^9\text{Be}$ Calibration		91

5.1	Monte Carlo with the $^{241}\text{Am}^9\text{Be}$ Source	92
5.1.1	The $^{241}\text{Am}^9\text{Be}$ Source Geometry	92
5.1.2	The $^{241}\text{Am}^9\text{Be}$ Source Event Generator	95
5.1.3	Determination of Source Positions and the AV/PSUP Offset	96
5.1.4	Modeling the Trigger Efficiency	96
5.1.5	Neutrons Transport in Water	97
5.1.6	Data Structure for the $^{241}\text{Am}^9\text{Be}$ Simulation	98
5.2	Comparison between Data and Monte Carlo	99
5.2.1	Data-MC Comparison for a Central Run: 109134	99
5.2.2	Data-MC Comparison Across the Detector	104
5.3	Volume-weighted Neutron Detection Efficiency	114
Chapter 6: Energy Calibration with The $^{241}\text{Am}^9\text{Be}$ Calibration Data		122
6.1	Energy Calibration using a Central $^{241}\text{Am}^9\text{Be}$ Run	124
6.1.1	Event Processing and Selection	124
6.1.2	Cherenkov photon spectrum for the prompt γ s	126
6.1.3	Simulations of the Electrons	127
6.1.4	The Electron Equivalent Energy Spectrum of the 4.4 MeV γ s	129
6.1.5	4.4 MeV γ s Reconstructed Energy Spectrum from Calibration	131
6.1.6	Fit Results	135
6.2	Spatial Variation of the Energy Scale and Energy Resolution	138
Chapter 7: Searching for Reactor Antineutrinos in Water		140
7.1	Dataset	141
7.1.1	Run Selection and Live Time	142
7.1.2	Detector Event Rate	143
7.1.3	Trigger Thresholds	145
7.2	Selection Algorithm for Antineutrino Candidates	145
7.3	Background Characteristics	147
7.3.1	Time difference distribution	148
7.3.2	Distance distribution	150
7.4	Signal Characteristics	151
7.5	Hypothesis Testing	152
7.6	Systematic Considerations	156
7.7	IBD Interaction Rate	159
7.8	Reactor Antineutrino Flux	160
Chapter 8: Conclusions		161
Bibliography		163

Appendix A: Drawings for Parts Used in the $^{241}\text{Am}^9\text{Be}$ Encapsulation 175

Appendix B: Acronyms 179

List of Tables

1.1	Most commonly used nuclei for inverse beta decay detection.	14
3.1	The duration and and source position of all internal $^{241}\text{Am}^9\text{Be}$ runs. The runs are subdivided into four groups (indicated by the solid lines). The first three runs are collected with the source at the center of the detector; the second group is a y-axis scan; the third group is a diagonal scan in the y-z plane; and the last group is a z-axis scan.	46
4.1	The fitted capture time constant and true value for the median and upper & lower RMS values of event rate parameters μ and σ	75
4.2	Neutron capture time constant for different neutron energy bins. . . .	83
4.3	Fitted neutron capture time constants and selection efficiencies from four different simulations. Efficiencies are excluded from the bottom two rows because their differences are estimated analytically to be smaller than the precision that is practically achievable with the simulation.	84
4.4	Systematic corrections and uncertainties for the $^{241}\text{Am}^9\text{Be}$ analysis. Values for τ are relative and those for E are absolute.	87

7.1 Summary of selection criteria in sequential order for the water dataset. Even though the nominal energy and nhits cuts for the delayed candidates are 1.0 MeV and 10 nhits, due to the processing threshold the effective thresholds are substantially higher. No time difference and distance cuts are applied. 147

List of Figures

1.1	The expected reactor antineutrino energy spectrum in SNO+. The reactor information is from IAEA[26] 2017 data and the oscillation parameters are best global fit from PDG 2016[27]. We expect 110 anti-neutrino event per year assuming 0.58×10^{32} target protons. The expected geo antineutrino contribution are stacked on top of the reactor spectrum.	15
2.1	Left: the SNO+ detector. The cavity is filled with ~ 7000 -tonnes ultra pure water to attenuate radiogenic backgrounds from the rock. Right: picture taken from a camera mounted on the PSUP [36]. The PMT hexagon panels, hold-down ropes, and the bottom of the neck are clearly seen.	20
2.2	A schematic of the Hamamatsu R1408 PMT. The two dashed lines shows the focussing grid and the nine solid lines are layers of the dynodes. The bottom of the PMT is filled with silicone gel for airtightness. Dimensions are in cm. Figure is from [42].	23

2.3	A schematic of the SNO+ calibration source manipulator system. A new design was made for the side rope boxes: instead of attaching to the ceiling, the boxes are now mounted directly on the UI. The UI also has a modified design where it is now mounted on the AV instead of the deck. Figure is from [42].	27
2.4	A side view of the scintillator phase URM, which preserves the essential design of the water phase URM. When not in use, the umbilical is stored between the two big pulleys in white. The central rope is mounted on the column in the right box, next to a block and tackle system. The compressed air system in brown provides power for playing out/in the umbilical. The system is calibrated with shaft encoders and load cells, shown in the right side of the figure. Figure is from [44].	28
2.5	Left: Top view of the UI. Three gate valves, four neck PMTs, and four side rope boxes occupy most of the space on the UI. Right: Isometric view of the UI. Four glove box ports are available on the side of the UI for source handling. Figure is from [45].	29
2.6	A schematic of the laserbox and laserball. Figure is from [42].	30
2.7	The ^{16}N source as implemented in the SNO+ simulation package. The blue box to the right represents the decay chamber. It is observed by a scintillation chamber (green) which also holds a PMT (black). Figure is from [48].	31
2.8	The SNO+ ^8Li source design. Figure is from [49].	32
3.1	Original package for the SLB024 $^{241}\text{Am}^9\text{Be}$ source. The size specifications are: A=8mm, B=10mm, and C=0.8mm. Figure is from [56]. . .	37

3.2	The SNO encapsulations on the $^{241}\text{Am}^9\text{Be}$ source. The inner layer of the encapsulation is shown in the red box.	38
3.3	Engineering drawing of the new encapsulation for the $^{241}\text{Am}^9\text{Be}$ source. Figure is from [56].	40
3.4	The specially designed nuts that fills the space between the upper and lower lips. Figure is from [56].	41
3.5	The “captured nut” structure. Figure to the left is from [56].	42
3.6	A schematic of the $^{241}\text{Am}^9\text{Be}$ calibration source positions.	47
3.7	The $^{241}\text{Am}^9\text{Be}$ source assembly was attached to the stem and carriage. The umbilical and central rope were still mounted on the URM, but can be seen to the left side of the figure.	48
3.8	A schematic of the SNO+ deck floor. In total six vertical guide tubes (small blue concentric circles) are available for external source deployment. The UI is shown as a purple circle. These guide tubes are made of stainless steel and provide access through the PSUP to the AV. Guide tube 5 was used for the external $^{241}\text{Am}^9\text{Be}$ calibration. Figure is from [42].	50
3.9	Event displays during an external $^{241}\text{Am}^9\text{Be}$ calibration run at $z=0$ m. Top left: PMT hits of a prompt event (4.4 MeV γ); Top right: color-coded sum of PMT hits for a duration of 10 min. Events are seen to be clustered at where the source was placed; Bottom: nhits spectra over a 10 s and 60 s period, respectively. The peak at around 30 nhits indicates that the 4.4 MeV prompt γ s were collected.	51

4.1	Time difference histogram constructed from a toy MC model, where a set of realistic parameters are configured: $E = 50\%$, $P = 90\%$, $\lambda^{-1} = 208.2 \mu\text{s}$, and $R_2 = 360 \text{ Hz}$. The normalization is done in arbitrary unit. Different components of the histogram (shown in different colors) exhibit different patterns as explained in Section 4.1.1.	60
4.2	Decomposition of the time difference distribution of the <i>True-True</i> event pairs. Two exponential components with different constant can be identified: One slower component that reflects the underlining background rate, and the second which is additionally sensitive to the neutron capture constant λ	61
4.3	Fit results of a one-hour $^{241}\text{Am}^9\text{Be}$ run with the source placed at the center of the detector. The time difference histogram is obtained by placing prompt and delayed nhits cuts of 17 and 7, respectively. Fitted parameters of particular physics interest include the product of P and E , and the neutron capture constant λ , or $\frac{1}{\tau}$. Note that the fitted capture time constant value is different from what is given in Eqn. 4.9 because the latter is averaged for the three hours of data taken in the center of the detector.	63
4.4	Top: fitted time difference histograms with varying prompt candidate nhits cut from 15 to 33 (the delayed candidate nhits cut is fixed to 4). Bottom: fitted time difference histograms with varying delayed candidate nhits cut from 4 to 22 (the prompt candidate nhits cut is fixed to 15).	64

4.5	Change of important fit parameters as a function of the prompt (delayed) candidate nhits threshold. From top to bottom, plotted are the fitted event rate (R_1 or R_2), $P \cdot E$, capture time constant τ , and the signal rate $R_1 \cdot PE$	66
4.6	The event rate distribution as a function of the nhits threshold. For standard physics runs the event rate decreases more rapidly as there are few events above 20 nhits.	67
4.7	Nhits distributions for the neutrons and the 4.4 MeV γ s. These distributions are derived from calculating the difference between consecutive data points of the signal rate distribution in Fig. 4.5.	69
4.8	The fitted neutron capture time constant τ as a function of the radial source position. The weighted average is shown in the green line. . . .	70
4.9	The neutron detection efficiency E as a function of the radial source position. Data points in red are collected from positive z positions and their drop towards higher radius is due to the absence of PMT coverage close to the AV neck.	72
4.10	Detector event rate of run 109134 fitted with a Maxwell-like distribution.	74
4.11	Distribution of the fit parameters for all internal AmBe runs.	74
4.12	Example distribution of fitted capture time for a given set of event rate variation parameters.	76
4.13	Fitted capture time constant as a function of delayed event nhits threshold, before (red) and after (blue) the correction for the fluctuating rate systematic. The prompt candidate nhits threshold is 15 nhits.	77

4.14	Illustration of how the Maxwell-like rate distribution becomes more symmetric with increasing delayed nhits threshold. Note that at 7 nhits and above the distributions were best fitted with a Gaussian, while below 7 nhits the distributions were fitted with the Maxwell-like function, consistent with the jump observed in λ in Fig. 4.13.	78
4.15	Data cleaning sacrifice for prompt and delayed candidate events. Figure is from [74].	79
4.16	Comparison of prompt (top) and delayed (bottom) candidate data cleaning sacrifices to the calculated 4.4-MeV γ and neutron capture data cleaning sacrifices. Figure is from [75].	80
4.17	Overlay of calculated sacrifices for neutron captures and 4.4-MeV γ 's using internal AmBe data. Figure is from [75].	81
4.18	Energy spectrum of neutrons emitted from the $^{241}\text{Am}^9\text{Be}$ source in RAT.	82
4.19	The time difference histogramss fitted with an exponential for thermal neutrons (left) and $^{241}\text{Am}^9\text{Be}$ energy neutrons (right).	83
4.20	The (n, γ) cross-section \times velocity [barn \times m/s] as a function of temperature. Uncertainties are included but too small to be seen. Figure is from [77].	87
4.21	Thermal n - p radiative capture cross-section measurements as a function of publication year. [82]	90
5.1	The cross-sectional profile of the updated $^{241}\text{Am}^9\text{Be}$ source geometry constructed for Monte Carlo production.	94

5.2	The trigger efficiency curve of a central $^{241}\text{Am}^9\text{Be}$ run from the nhits monitor (Data) compared to the realistic trigger model in Monte Carlo. A simulated nhits distribution of the neutron signal with perfect trigger efficiency is overlaid on top. Please note that the x-axis plots the prompt nhits only.	97
5.3	Data-MC comparison of nhits for the neutron and 4.4 MeV γ signals for a central $^{241}\text{Am}^9\text{Be}$ run.	100
5.4	Data-MC comparison of reconstructed energy for neutron and 4.4 MeV γ signals for a central $^{241}\text{Am}^9\text{Be}$ run.	101
5.5	Data-MC comparison of reconstructed distance for neutron and 4.4 MeV γ signals.	101
5.6	Data-MC comparison of β_{14} for neutron and 4.4 MeV γ signals. . . .	103
5.7	Data-MC comparison of ITR for neutron and 4.4 MeV γ signals. . . .	104
5.8	Nhits distributions for neutron signals at different positions of the detector.	106
5.9	Nhits distributions for the 4.4 MeV γ s at different positions of the detector.	107
5.10	Reconstructed energy spectra for neutron signals at different positions of the detector.	108
5.11	Reconstructed energy spectra for the 4.4 MeV γ s at different positions of the detector.	109
5.12	β_{14} distributions for neutron signals at different positions of the detector.	110
5.13	β_{14} distributions for the 4.4 MeV γ s at different positions of the detector.	111
5.14	ITR distributions for neutron signals at different positions of the detector.	112

5.15	β_{14} distributions for the 4.4 MeV γ s at different positions of the detector.	113
5.16	The neutron detection efficiency obtained from data vs. the neutron detection efficiency simulated with the realistic trigger model. A linear relationship can be drawn between these two quantities.	115
5.17	A 2D plot of corrected neutron detection efficiency in the XZ plane. .	116
5.18	A 2D plot of corrected neutron detection efficiency in the YZ plane. .	117
5.19	The corrected neutron detection efficiency as a function of radius. Each point represents a cell in the detector. NDE in the figure title and y-axis is short for neutron detection efficiency.	118
5.20	There exists a weak asymmetry along the x and y direction. The neutron detection efficiency tends to be higher in the positive x and negative y hemisphere. NDE_1-NDE_2 is the fractional difference between the cell (x,y) and its reflection over the two axes.	119
5.21	A 2D plot of the corrected neutron detection efficiency in radius and angle for XZ plane.	120
5.22	A 2D plot of the corrected neutron detection efficiency in radius and angle for YZ plane.	121
6.1	The level scheme of ^{12}C . In the context of the analyses presented in this thesis, the prompt γ can be treated as monoenergetic. Figure is from [80].	126
6.2	The distribution of number of Cherenkov photons produced by 4.4 MeV γ s.	127
6.3	The distribution of number of Cherenkov photons produced for monoenergetic electrons of 3.5 MeV. The non-Gaussian shape is evident.	128

6.4	2D histogram of number of Cherenkov photons and Monte Carlo event kinetic energy (E_{elec} in the x-axis). Individual plots such as Fig. 6.3 is in fact an x-axis slice of Fig. 6.4 at different energies.	129
6.5	The electron equivalent energy spectrum of the 4.4 MeV γ s.	130
6.6	Top: number of coincidences as a function of time difference cut. The plot can be fitted with a sum of an exponential and a constant, corresponding to the $^{241}\text{Am}^9\text{Be}$ signals and backgrounds, respectively. Bottom: purity as a function of time difference cut.	131
6.7	The background energy spectrum. The two spectra with different time cuts are shown to be identical with each other.	133
6.8	The reconstructed energy spectra for events with nhits values of 10, 12, and 14. These events tend to be reconstructed in the energy range from 1.5 MeV to 2.5 MeV.	134
6.9	The reconstructed spectrum of the 4.4 MeV γ s (blue curve). It is derived by subtracting the background spectrum from the prompt . The purity of the selection is evaluated to be 72.9%.	135
6.10	Fitted energy spectrum for 4.4 MeV γ s for a central $^{214}\text{Am}^9\text{Be}$ run. Two different fit regions ([1.8, 8.0] MeV and [2.5, 8.0] MeV) are shown.	136
6.11	The energy resolution and scale across the detector, as measured using an ^{16}N source. ρ is the radius the on x-y plane. Figure is from [99].	137
6.12	The energy resolution as a function of radial position. Left: [1.8, 8.0] MeV; Right: [2.5, 8.0] MeV.	138
6.13	The energy scale as a function of radial position. Left: [1.8, 8.0] MeV; right: [2.5, 8.0] MeV.	139

7.1	The fraction of good data for physics analyses (labelled with "Gold") as a function of time. Figure is from [105].	143
7.2	Detector event rate as seen in data plotted in continuous hours. The event rate is plotted after applying a set of loose cut including fit validity, β_{14} , ITR, and $\mathbf{u}\cdot\mathbf{R}$	144
7.3	Top: event rate distribution fitted with three independent Gaussians; Bottom: distribution of time difference of coincidence pairs, fitted with three independent exponentials.	148
7.4	Distances between coincidence pairs. The distribution can be fitted with an analytical function describing distance between random points within a ball. Higher order corrections can significantly improve the goodness of fit.	149
7.5	Position distributions along the x-, y-, z-axis. The z-axis shows significant distortion.	151
7.6	Distribution of time difference and distance of antineutrino pairs. . .	152
7.7	The product of the cumulative probability of the time difference and distance distributions for the antineutrino pairs.	153
7.8	The likelihood fit on \mathbf{p} and the profile log-likelihood plot.	155
7.9	The likelihood ratio plot. Overlaid is the normalized cumulative and the 1σ upper limit of 2.13 events for the number of signals observed.	156
7.10	Distributions of the best fit value and 1σ upper limit with a 10% perturbation on \mathbf{p}_s . The average and corrected standard deviation of the best fit value and 1σ upper limit are 0.605 ± 0.045 and 2.131 ± 0.026	158

A.1	Drawing of the nuts (part no. 90257A005) used in the new encapsulation for the $^{241}\text{Am}^9\text{Be}$ source. Figure is from [109].	176
A.2	Drawing of the O-ring (part no. 9452K119) used in the new encapsulation for the $^{241}\text{Am}^9\text{Be}$ source. Figure is from [109].	177
A.3	Drawing of the O-ring (part no. 90152A116) used in the new encapsulation for the $^{241}\text{Am}^9\text{Be}$ source. Figure is from [109].	178

Chapter 1

Neutrino Physics

1.1 Neutrinos

The neutrino is a fundamental, electrically neutral, spin-1/2 particle. Due to its lightness and extremely small interaction cross-sections, the neutrino is one of the least understood particles in the Standard Model of particle physics.

First postulated in the 1930s by Wolfgang Pauli [1] [2] in an attempt to solve the apparent violation of energy conservation in nuclear β decay experiments, the neutrino evaded direct detection for almost 30 years until 1956, when Reines and Cowan [3] made use of the powerful background rejection technique of the inverse beta decay (IBD, Eqn. 1.1).



Shortly after, the second flavor of neutrinos was detected in 1962 [4], and finally, a third in 2000 [5]. Differentiated by flavors, the electron neutrino, the muon neutrino, and the tau neutrino are named in association with their corresponding charged leptons.

One of the most fascinating properties of neutrinos is that they oscillate between

the three different flavors. This originates from the fact that the eigenstates of the weak interaction (ν_e , ν_μ and ν_τ) do not coincide with their mass eigenstates (ν_1 , ν_2 and ν_3). The first experimental discovery of neutrino oscillation was made by the SuperKamiokande experiment [6] observing a zenith angle dependent deficit of atmospheric muon neutrinos and the Sudbury Neutrino Observatory experiment [7] (the progenitor of the SNO+ experiment) revealing the absence of ^8B solar neutrinos via the charged current channel and the appearance of the full flux when all neutrino flavors were detected using a neutral-current channel. Thanks to additional data from reactor and beam neutrino experiments, precise knowledge of the neutrino mixing matrix (also known as the Pontecorvo-Maki-Nakagawa-Sakata matrix) that governs the oscillation was acquired in recent few decades. Neutrino oscillation is one of the few pieces of direct evidence for the existence of physics beyond the Standard Model.

As will be shown mathematically later in this chapter, one of the prerequisites for neutrino oscillation is that neutrinos of different flavors have different mass eigenstates, which means that at least two neutrino flavors have nonzero masses. A combination of different probes and techniques have been used to measure the neutrino masses, most notably tritium β decay experiments and cosmological and astrophysical observations. The tritium experiments render a direct constraint on the mass of $\bar{\nu}_e$ by measuring the spectrum of electrons from beta decays near the end point. The current best limit comes from the Troitsk experiment [8] with $m_{\bar{\nu}_e} < 2.05$ eV (95% CL.). On the other hand, if one assumes the validity of the ΛCDM model, the cosmological and astrophysical observations, mostly from the cosmic microwave background and baryon acoustic oscillation data, can place a more stringent upper bound on the sum of neutrino masses [9]: $\sum_j m_j < 0.170$ eV (95% CL.).

Despite the blossoming of neutrino physics in recent decades, important questions about neutrinos remain open: the absolute neutrino mass scale is unknown; the ordering of the neutrino masses is uncertain; the CP-violating phase is unmeasured; and the basic nature of the neutrino, whether it is a Dirac or Majorana particle (whether neutrino is its own antiparticle), is undetermined. In pursuit of answers to these questions, large scale low-background experiments stand out as one of the most efficient and cost-effective strategies. One of such experiments, the SNO+ experiment, utilizes almost one kilotonne of liquid scintillator as the detector volume and intends to address one or more of the questions above. The main objective of SNO+ is a search for the neutrinoless double beta decay, whose existence would prove that neutrinos are Majorana particles. A detailed description of the experiment can be found in Chapter 2.

SNO+ has just finished its water phase and is currently in the process of filling with liquid scintillator. This thesis focuses on my efforts to search for reactor antineutrinos with a small portion of the water phase dataset. In the following three sections I will describe the fundamental physics associated with reactor antineutrino detection in large scale low-background experiments. The physics considerations for these experiments generally come in threefold: the origin, the propagation, and the detection.

1.2 The Source: Reactor Antineutrino Spectrum

Most of our knowledge about this elusive particle comes from six sources of neutrinos: solar, atmospheric, supernova, accelerator, reactor and geo-neutrinos. A pure, powerful and controllable source of electron antineutrinos, nuclear reactors have been

the oldest workhorse for neutrino scientists. The first generation of the reactor experiments successfully prevented physicists from using an atomic bomb for the first detection of (anti-)neutrinos [10]. The second-generation experiments, highlighted by the KamLAND [11] experiment, confirmed that neutrinos oscillate using the reactor antineutrino disappearance channel shortly after SuperKamiokande and SNO demonstrated neutrino flavor change. Daya Bay, Double Chooz, and RENO started the precision era of neutrino physics as the third generation experiments, producing a definitive measurement of the last unknown mixing angle, θ_{13} . The next generation reactor antineutrino experiments will be spearheaded by the JUNO experiment [12], with a major goal to determine the neutrino mass ordering.

In order to precisely measure the neutrino oscillation parameters, accurate knowledge of reactor antineutrino spectra is a necessity. As a matter of fact, many reactor antineutrino experiments utilize one or more small “near detectors” that are relatively close to the reactor(s) to reduce the systematic uncertainties from the antineutrino spectrum.

The majority of antineutrinos emitted from the reactors are the product of beta decays of the fission fragment from Uranium and Plutonium. A very small portion of low energy neutrinos, which are below the inverse beta decay threshold, could also come from neutrons capturing on ^{238}U . Neglecting the neutron captures on ^{238}U , the total antineutrino spectrum can be expressed as follows [13]:

$$S(E_\nu) = \sum_i f_i S_i(E_\nu), \quad (1.2)$$

where f_i and $S_i(E_\nu)$ are the fission rate and the cumulative antineutrino spectrum of isotope i , respectively. $S_i(E_\nu) = \frac{dN_i}{dE_\nu}$ can be derived, either by summing up all

antineutrino spectra of individual fission fragment β -decay spectra, or through direct conversion based on the measurement of the electron spectra of fissioning[14, 15]. Due to large uncertainties in nuclear data, the first method yields significantly larger error (at the 10% level) whereas the second method has an averaged uncertainty of 2%. Most often the accessible data from reactors are in the form of the thermal power of the reactor cores (as a function of time), which can be expressed as the sum of thermal energy from all individual fission fragments:

$$W_{\text{th}} = \sum_i f_i e_i, \quad (1.3)$$

where W_{th} is the thermal power and e_i is the energy release per decay for isotope i .

Combining Eqn. 1.2 and Eqn. 1.3, the antineutrino spectrum can be written as:

$$S(E_\nu) = \frac{W_{\text{th}}}{\sum_i (f_i/F) e_i} \sum_i \frac{f_i}{F} S_i(E_\nu). \quad (1.4)$$

The relative fraction f_i/F is the fission fraction of isotope i and can be predicted with reactor core simulations. Most of the time these simulations are reactor specific, but can be roughly divided into two categories: the first type includes Pressurized Water Reactors (PWRs) and Boiling Water Reactors (BWRs), where the reactors use enriched Uranium as the main fuel and are only refueled about once a year; the second type is the Canada Deuterium Uranium (CANDU) reactors, which uses heavy water as neutron moderator and therefore can run on natural Uranium. They also refuel more frequently and f_i/F is kept close to constant. The CANDU reactors contribute to about 60% of the total reactor antineutrino flux expected for SNO+.

As a conclusion, the reactor antineutrino spectrum can be determined from thermal power measurements, reactor core simulations, and knowledge of neutrino spectra of fuel isotopes. Currently, the uncertainty on the reactor antineutrino flux is about (2-3)% [16]. For single-detector experiments, the dominant uncertainty on the oscillation parameters comes from the neutrino spectrum.

Accurate measurements on the reactor antineutrino flux can be very helpful in understanding the so-called “reactor neutrino anomaly” [17], an observation that the measured reactor antineutrino flux is consistently lower than predicted. The anomaly could originate from two possible sources: either there is a new oscillation between the three known species of neutrinos and a new type of sterile neutrinos, or some underestimated systematic uncertainties in the theoretical flux calculation.

1.3 The Propagation: Neutrino Oscillation

1.3.1 The PMNS Matrix

Recent decades’ precision measurements of the neutrino squared-mass differences and mixing angles has shown that the neutrino oscillation can be interpreted in the framework of a 3×3 unitary mixing matrix, the Pontecorvo-Maki-Nakagawa-Sakata (PMNS) matrix. For more in-depth and detailed reviews, the reader is referred to [16] and [18].

Analogous to quark oscillation in the hadron sector, neutrino oscillation is a quantum-mechanical phenomenon that originates from the mismatch between the flavor eigenstates in weak interactions and the mass eigenstates when propagating in space. The PMNS matrix, with components $U_{\alpha i}$ denoting the amplitude of mass eigenstate i in flavor a , is a unitary transformation:

$$U = \begin{pmatrix} U_{e1} & U_{e2} & U_{e3} \\ U_{\mu1} & U_{\mu2} & U_{\mu3} \\ U_{\tau1} & U_{\tau2} & U_{\tau3} \end{pmatrix}. \quad (1.5)$$

As is the case for any 3×3 **unitary** matrix, U has 9 degrees of freedom, and can be parametrized by 3 mixing angles and 6 phases. However, not all the phases are physical: if neutrinos are Dirac particles, only one of the phases is physical, widely known as the Dirac CP violating phase; or if neutrinos are Majorana particles, then the additional two Majorana phases should be counted. As will be shown below, these two phases do not manifest in the neutrino oscillation.

Neglecting the unphysical phases, the PMNS matrix can be written as the product of three rotation matrices consisting of one CP violating phase and three mixing angles and a diagonal matrix P :

$$U = \begin{pmatrix} 1 & 0 & 0 \\ 0 & \mathcal{C}_{13} & \mathcal{S}_{23} \\ 0 & -\mathcal{S}_{13} & \mathcal{C}_{23} \end{pmatrix} \begin{pmatrix} \mathcal{C}_{13} & 0 & \mathcal{S}_{13}e^{-i\delta_{\text{CP}}} \\ 0 & 1 & 0 \\ -\mathcal{S}_{13}e^{-i\delta_{\text{CP}}} & 0 & \mathcal{C}_{13} \end{pmatrix} \begin{pmatrix} \mathcal{C}_{12} & \mathcal{S}_{12} & 0 \\ -\mathcal{S}_{12} & \mathcal{C}_{12} & 0 \\ 0 & 0 & 1 \end{pmatrix} P. \quad (1.6)$$

where $\mathcal{C}_{ij} \equiv \cos\theta_{ij}$, $\mathcal{S}_{ij} \equiv \sin\theta_{ij}$, and θ_{ij} are the mixing angles. It is easy to prove that \mathcal{S}_{ij} satisfies:

$$\mathcal{S}_{13}^2 = |U_{e3}|^2, \mathcal{S}_{23}^2 = \frac{|U_{\mu1}|^2}{1 - |U_{e3}|^2}, \mathcal{S}_{12}^2 = \frac{|U_{e2}|^2}{1 - |U_{e3}|^2}. \quad (1.7)$$

Conventionally, θ_{12} is known as the solar angle and θ_{23} the atmospheric angle, since they are responsible for the solar electron neutrino oscillation and the dominant atmospheric muon neutrino oscillation, respectively. θ_{13} , relatively smaller than the

other two, was the last mixing angle to be measured through reactor antineutrino experiments. Current best fit values of the mixing parameters can be found in [16].

The diagonal matrix P in Eqn. 1.6 is dependent on the nature of the neutrino:

$$P = \begin{pmatrix} 1 & 0 & 0 \\ 0 & 1 & 0 \\ 0 & 0 & 1 \end{pmatrix}, \text{ if Dirac; } \begin{pmatrix} e^{i\rho} & 0 & 0 \\ 0 & 1 & 0 \\ 0 & 0 & e^{i\sigma} \end{pmatrix}, \text{ if Majorana.} \quad (1.8)$$

where ρ and σ are the two Majorana phases.

1.3.2 Vacuum Oscillation

Neutrino oscillation in a vacuum can be conceived as a three-step process: Production, propagation, and detection.

During the production process, the (anti-)neutrino is produced as one of the three pure flavors via weak interactions, and can be expressed as:

$$|\nu(t=0)\rangle = |\nu_\alpha\rangle = \sum_i U_{\alpha i} |\nu_i\rangle;$$

$$|\bar{\nu}(t=0)\rangle = |\bar{\nu}_\alpha\rangle = \sum_i U_{\alpha i}^* |\bar{\nu}_i\rangle.$$

As the neutrino propagates, the mass eigenstate is naturally the eigenstate of its Hamiltonian in vacuum, making the neutrino no longer at a pure flavor eigenstate. We will make an assumption¹ here that the mass eigenstates can be described by a

¹The proper treatment should be using the wavepacket formalism in the framework of quantum theory [19] [20]; however, this more complicated derivation yields the same result as the classical approach presented here.

plane wave with well-defined momenta \mathbf{p}_i and that $\mathbf{p}_i = \mathbf{p}$. Therefore,

$$\begin{aligned} |\nu(t)\rangle &= \sum_i U_{\alpha i} e^{-i(E_i t - \mathbf{p}_i \cdot \mathbf{x})} |\nu_i\rangle \\ &= \sum_i U_{\alpha i} e^{-i(E_i t - \mathbf{p}_i \cdot \mathbf{x})} \sum_{\beta} U_{\beta i}^* |\nu_{\beta}\rangle, \end{aligned} \quad (1.9)$$

where $E_i = \sqrt{\mathbf{p}^2 + m_i^2}$ is the energy of the i -th mass eigenstate.

For the final detection, the neutrino has to interact as one of the three flavors. The probability for a neutrino of flavor α to have oscillated into flavor β is:

$$\begin{aligned} P(\nu_{\alpha} \rightarrow \nu_{\beta}) &= |\langle \nu_{\beta} | \nu(t) \rangle|^2 \\ &= \left| \sum_i U_{\alpha i} U_{\beta i}^* e^{-i(E_i t - \mathbf{p}_i \cdot \mathbf{x})} \right|^2. \end{aligned} \quad (1.10)$$

Assuming neutrinos are ultra-relativistic (which is true for all neutrino experiments to this generation), we can write the final expression of Eqn. 1.10 as:

$$\begin{aligned} P(\nu_{\alpha} \rightarrow \nu_{\beta}) &= \delta_{\alpha\beta} - 4 \sum_{i>j} \text{Re}(U_{\alpha i}^* U_{\beta i} U_{\alpha j} U_{\beta j}^*) \sin^2\left(\frac{\Delta m_{ij}^2 L}{4E}\right) \\ &\quad + 2 \sum_{i>j} \text{Im}(U_{\alpha i}^* U_{\beta i} U_{\alpha j} U_{\beta j}^*) \sin^2\left(\frac{\Delta m_{ij}^2 L}{2E}\right), \end{aligned} \quad (1.11)$$

where $\Delta m_{ij}^2 \equiv (m_i^2 - m_j^2)$. This is a mathematical illustration that nonzero neutrino masses is a necessity for neutrino oscillation.

Measurements of solar electron neutrino oscillation fix the sign of Δm_{21}^2 to be positive. Without loss of generality, conventionally it was chosen that $|\Delta m_{21}^2| < |\Delta m_{31}^2|$. In fact, current global best fit [16] dictates that $|\Delta m_{21}^2| \ll |\Delta m_{31}^2|$ to be valid. However, the sign of Δm_{31}^2 is yet to be determined, leaving out two possible

scenarios: either $m_1 < m_2 \ll m_3$, or $m_3 \ll m_1 < m_2$. This is widely known as the neutrino mass ordering problem.

It should also be noted that Eqn. 1.11 indicates that the two Majorana phases does not affect the oscillation probability, since the diagonal matrix P follows $P \cdot P^* = P^* \cdot P = \mathbf{1}$. Therefore neutrino oscillation can not be used as a probe for the nature of the neutrino.

Similar to the neutrino case, the antineutrino oscillation probability can be written as:

$$\begin{aligned}
 P(\bar{\nu}_\alpha \rightarrow \bar{\nu}_\beta) &= \delta_{\alpha\beta} - 4 \sum_{i>j} \text{Re}(U_{\alpha i}^* U_{\beta i} U_{\alpha j} U_{\beta j}^*) \sin^2\left(\frac{\Delta m_{ij}^2 L}{4E}\right) \\
 &\quad - 2 \sum_{i>j} \text{Im}(U_{\alpha i}^* U_{\beta i} U_{\alpha j} U_{\beta j}^*) \sin^2\left(\frac{\Delta m_{ij}^2 L}{2E}\right).
 \end{aligned} \tag{1.12}$$

Eqn. 1.12 is identical to Eqn. 1.11 except for the sign on the imaginary term. Therefore if the Dirac phase $\delta_{CP} \neq 0$ or π , CP violation (that is, $P(\nu_\alpha \rightarrow \nu_\beta) \neq P(\bar{\nu}_\alpha \rightarrow \bar{\nu}_\beta)$) is possible in the appearance channels ($\beta \neq \alpha$). However, in disappearance channels the non-oscillation probability is the same for neutrinos and antineutrinos. This can be shown in Eqn. 1.11 as the combination $U_{\alpha i}^* U_{\beta i} U_{\alpha j} U_{\beta j}^*$ is real when $\alpha = \beta$:

$$\begin{aligned}
 P(\nu_\alpha \rightarrow \nu_\alpha) &= 1 - 4 \sum_{i>j} |U_{\alpha i} U_{\alpha j}|^2 \sin^2\left(\frac{\Delta m_{ij}^2 L}{4E}\right) \\
 &= P(\bar{\nu}_\alpha \rightarrow \bar{\nu}_\alpha).
 \end{aligned} \tag{1.13}$$

1.3.3 Neutrino Oscillation Experiments

This subsection will discuss different L/E values for Eqn. 1.11. Experiments that satisfy $\Delta m_{21}^2 L/E \ll 1$ can be approximated by setting $\Delta m_{21}^2 = 0$, and therefore

$\Delta m_{31}^2 = \Delta m_{32}^2$. We can then write Eqn. 1.11 as [21]:

$$P(\nu_\alpha \rightarrow \nu_\beta) = \delta_{\alpha\beta} - (2\delta_{\alpha\beta} - 1)\sin^2 2\theta_{\alpha\beta}^{\text{eff}} \sin^2\left(\frac{\Delta m_{31}^2 L}{4E}\right), \quad (1.14)$$

where $\theta_{\alpha\beta}$ follows:

$$\sin^2 2\theta_{\alpha\beta}^{\text{eff}} \equiv \begin{cases} 4|U_{\alpha 3}U_{\beta 3}|^2, & \text{if } \beta \neq \alpha; \\ 4|U_{\alpha 3}|^2(1 - |U_{\alpha 3}|^2), & \text{if } \beta = \alpha. \end{cases} \quad (1.15)$$

Eqn. 1.14 and Eqn. 1.15 are the underlining detector philosophy for long-baseline beam neutrino experiments and short-baseline reactor experiments.

For experiments with $\Delta m_{21}^2 L/E \gtrsim 1$ and $\Delta m_{31}^2 L/E \ll 1$, the Δm_{31}^2 -driven oscillations are averaged. Specifically, the oscillations of electron (anti-)neutrinos are dominated by Δm_{21}^2 rather than Δm_{31}^2 . We have:

$$P(\nu_e \rightarrow \nu_e) = P(\bar{\nu}_e \rightarrow \bar{\nu}_e) \simeq \sin^4 \theta_{13} + \cos^4 \theta_{13} \left(1 - \sin^2 2\theta_{12} \sin^2\left(\frac{\Delta m_{21}^2 L}{4E}\right)\right) \quad (1.16)$$

Eqn. 1.16 applies to the long-baseline reactor antineutrino experiments (eg. SNO+). For some experiments the approximation that $\sin^2 \theta_{13} = 0$ can be true:

$$P(\nu_e \rightarrow \nu_e) = P(\bar{\nu}_e \rightarrow \bar{\nu}_e) \simeq 1 - \sin^2 2\theta_{12} \sin^2\left(\frac{\Delta m_{21}^2 L}{4E}\right). \quad (1.17)$$

1.4 The Detection: Inverse Beta Decay

There are a handful of interactions other than Eqn. 1.1 that can be used for antineutrino detection. For example, MUNU [22] and GEMMA [23] uses antineutrino-electron elastic scattering (Eqn. 1.18) and coherent antineutrino-nucleus scattering (Eqn. 1.19) to look for neutrino magnetic moment.

$$\bar{\nu}_e + e^- \longrightarrow \bar{\nu}_e + e^- . \quad (1.18)$$

$$\bar{\nu}_e + N \longrightarrow \bar{\nu}_e + N . \quad (1.19)$$

Nevertheless, the most popular reaction to detect antineutrinos is the inverse beta decay (Eqn. 1.1). Inverse beta decay is a standard quasielastic scattering process that is very well understood theoretically. The energy threshold for this process can be calculated in the laboratory frame:

$$E_\nu^{\text{thr}} = \frac{(M_n + m_e)^2 - M_p^2}{2M_p} = 1.806\text{MeV} . \quad (1.20)$$

With the approximation that the nucleon mass is infinite, the differential cross-section can be written as:

$$\left(\frac{d\sigma}{d\cos\theta}\right)^{(0)} = \frac{G_F^2 \cos^2\theta_C}{2\pi} (1 + \Delta_{\text{inner}}^R) [(f^2 + 3g^2) + (f^2 - g^2)v_e^{(0)}\cos\theta] E_e^{(0)} p_e^{(0)} . \quad (1.21)$$

where G_F is the Fermi coupling constant and θ_C is the Cabibbo angle. The vector and axial vector coupling constants are $f = 1$ and $g = 1.27$, respectively. $\Delta_{\text{inner}}^R \simeq 0.024$ is the energy independent inner radiative corrections. $E_e^{(0)}$ and $p_e^{(0)}$ are the energy

and momentum of the final state positron while ignoring the recoil neutron kinetic energy.

The total cross-section can be related to the neutron lifetime:

$$\begin{aligned}\sigma_{\text{tot}}^{(0)} &= \frac{2\pi^2/m_e^5}{f^R\tau_n} E_e^{(0)} p_e^{(0)} \\ &\approx 9.52 \times \left(\frac{E_e^0 \cdot p_e^{(0)}}{\text{MeV}^2}\right) \times 10^{-44} \text{cm}^2,\end{aligned}\tag{1.22}$$

where $\tau_n = 880.2 \pm 1.0$ s is the neutron lifetime and $f^R = 1.7152$ is the neutron decay phase space factor excluding the inner radiative corrections [16]. It is worth noting that the approximation that we made on the nucleon mass does not always apply. Higher order corrections can be accurately made [13].

When compared to other reactions used for detecting antineutrinos, the inverse beta decay has some significant advantages:

- its cross-section is relatively large;
- its cross-section, spectrum and angular distribution can be accurately calculated;
- its measurable e^+ energy is strongly correlated with the $\bar{\nu}_e$ energy;
- material rich in free protons are cheap and has excellent scalability;
- simultaneous emission of the e^+ and neutron provides a coincident signal and can be used to reduce background.

Neutrons produced from IBD will thermalize and get captured by the target nuclei. Table 1.1 shows various nuclei used in experiments and compares them in signal energy as well as cross-section.

Target nucleus	capture reaction	energy deposited	cross-section (barn)
${}^1\text{H}$	$n + p \longrightarrow d + \gamma$	2.2 MeV	~ 0.33
${}^{108}\text{Cd}$	$n + {}^{108}\text{Cd} \longrightarrow {}^{109}\text{Cd} + \gamma$	0.059 MeV	$\sim 1,000$
${}^{155}\text{Gd}$	$n + {}^{155}\text{Gd} \longrightarrow {}^{156}\text{Gd} + \gamma$	8.5 MeV	$\sim 61,000$
${}^{157}\text{Gd}$	$n + {}^{157}\text{Gd} \longrightarrow {}^{158}\text{Gd} + \gamma$	7.9 MeV	$\sim 256,000$

Table 1.1: Most commonly used nuclei for inverse beta decay detection.

1.5 Reactor Antineutrino with SNO+

The measurement of the reactor antineutrino spectrum and the determination of Δm_{21}^2 is one of the ultimate physics objectives for the SNO+ experiment. As is shown in Fig. 1.1, three Canadian reactors (Bruce, Pickering, and Darlington) contribute to $\sim 60\%$ of the reactor antineutrino flux for SNO+. The remaining flux mostly comes from the next closest reactors in the United States. With current reactor power output, it is estimated that 115 ± 6 reactor antineutrino events per year are expected in the SNO+ detector during water phase [24] and 110 ± 5 [25] for later phases. The difference mainly comes from the number of target protons for different detector medium.

The overall shape of the oscillated reactor antineutrino spectrum as measured by SNO+ allows a precise determination of Δm_{21}^2 . As discussed in Section 1.3.2, neutrino oscillations give rise to a survival probability that is energy dependent. The spectrum of detected electron antineutrinos will be distorted with maxima and minima caused by the oscillation. Specially, the deficit seen in the survival probability at approximately 4.5 MeV from Fig. 1.1 are uniquely exaggerated due to the coincident oscillation minima of the Bruce reactor and the Pickering and Darlington reactors.

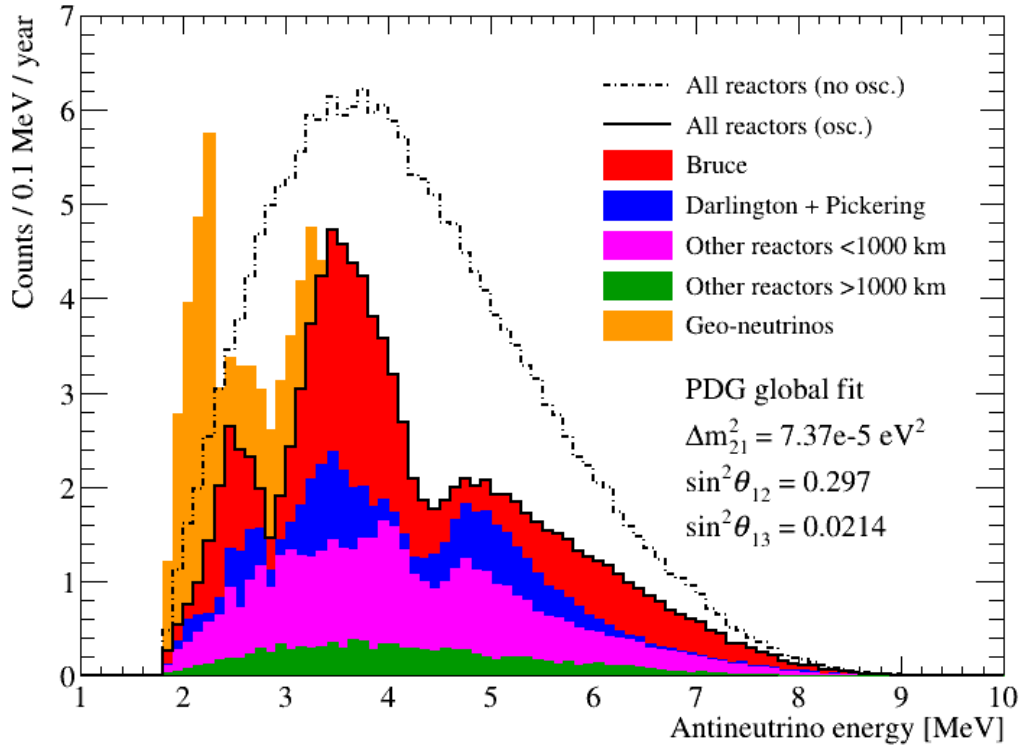


Figure 1.1: The expected reactor antineutrino energy spectrum in SNO+. The reactor information is from IAEA [26] 2017 data and the oscillation parameters are best global fit from PDG 2016 [27]. We expect 110 anti-neutrino event per year assuming 0.58×10^{32} target protons. The expected geo antineutrino contribution are stacked on top of the reactor spectrum.

With less than one year of liquid scintillator data, SNO+ expects to make an independent measurement with sufficient precision to resolve the current tension between solar and reactor neutrino measurements on Δm_{21}^2 . [28]. Furthermore, it is estimated that after 7 years of data taking with liquid scintillator (with and without Te), SNO+ will be able to measure Δm_{21}^2 to a precision of $0.2 \times 10^{-5} \text{ eV}^2$, which is comparable to the current best measurement from the KamLAND experiment [29] [30].

1.5.1 Reactor Antineutrinos in SNO+ Water Phase

In addition to the determination of Δm_{21}^2 during later phases of SNO+, attempts to detect reactor antineutrinos were made in the water phase.

Detecting reactor antineutrinos with pure water is challenging for several reasons. The neutron capture cross-section on hydrogen is significantly smaller than other isotopes (as is shown in Table 1.1); the neutron capture emits a signal of very low energy, which was below the trigger threshold for any pure water Cherenkov detector to date except SNO+; and the coincidence time (neutron capture constant) is long (small). As a result, reactor antineutrinos have never been detected in pure water.

Thanks to the very low energy threshold of the SNO+ detector, the neutron capture signal can be detected. In this thesis, work on the $^{241}\text{Am}^9\text{Be}$ calibration and results of a reactor antineutrino search using a 115-days pure water dataset are presented.

1.6 Organization of the Thesis

Chapter 2 provides a detailed introduction to the SNO+ experiment; Chapter 3 describes the hardware effort on the $^{241}\text{Am}^9\text{Be}$ source calibration; Chapter 4 presents a minimalistic statistical analysis of the $^{241}\text{Am}^9\text{Be}$ calibration data to extract several important observables including the neutron capture time constant, the neutron capture cross-section, and the neutron detection efficiency; Chapter 5 discusses the Monte Carlo simulation of the $^{241}\text{Am}^9\text{Be}$ source, and makes a full data-MC comparison. The position dependence of the neutron detection efficiency is also examined with the simulation; Chapter 6 discusses the energy calibration program using the

$^{241}\text{Am}^9\text{Be}$ calibration data; Chapter 7 details the analysis method for detecting antineutrinos; Chapter 8 is the conclusion.

Chapter 2

The SNO+ Experiment

2.1 Detector Overview

The SNO+ detector (Fig. 2.1) is located in a 30 m high, 22 m diameter barrel-shaped cavity, 2 km underground in SNOLAB, Sudbury, Ontario, Canada. It inherits most of the detector structure of the original SNO experiment, including an 8.9 m radius geodesic stainless steel structure (PSUP) on which sit around 9300 photomultipliers (PMTs) and a 6 m radius acrylic vessel (AV) that separates the internal liquid and external ultra pure water. A 6 m tall, 1.5 m diameter cylindrical neck sits on top of the AV. A universal interface (UI) is installed on top of the neck to allow for necessary AV access (e.g. calibration during the data-taking period). A deck clean room (DCR) is set up surrounding the UI for extra cleanliness. The deck, housing the electronics, the calibration system and the DCR, can be accessed through the experiment control room.

As one of the deepest and largest neutrino detectors, SNO finished its last phase in 2006, at which time a new experiment, the SNO+ experiment [31], was proposed to

continue the quest in neutrino physics. By replacing heavy water with liquid scintillator, SNO+ will enjoy a much lower threshold and greatly improved energy resolution. Many hardware additions and upgrades such as the hold-down rope system [32], the cover gas system, and an in-situ optical calibration system (ELLIE) [33] were made to convert SNO to SNO+. Several underground chemical plants including a liquid scintillator purification plant, a Telluric Acid purification plant and a Tellurium Butanediol complex production plant are also major supplemental projects to the new experiment.

2.1.1 Staged Approach

SNO+ takes a staged approach where three phases are planned to accomplish its physics goals:

The first phase, known as the water phase, ranged from May 4th, 2017 to July 16th, 2019. During this phase, the AV was filled with 890 tonnes light water. The main physics goal of this phase is a search for the invisible nucleon decay in ^{16}O [34], measurement of ^8B solar neutrino flux [35], and possible detection of reactor antineutrinos. Many efforts were also put into characterizing the detector performance, the PMT response, and external background measurements in preparation for the following phases.

The second phase, the pure scintillator phase, where the detector will be filled with 760 tonnes linear alkylbenzene (LAB; $\text{C}_n\text{H}_{2n+1}\text{-C}_6\text{H}_5$, $n=10\sim 13$), focuses on the measurement of low energy solar neutrinos, and reactor/geo antineutrinos. During this phase, the optical model of the liquid scintillator and detector response will be examined, and the intrinsic background of the LAB evaluated.

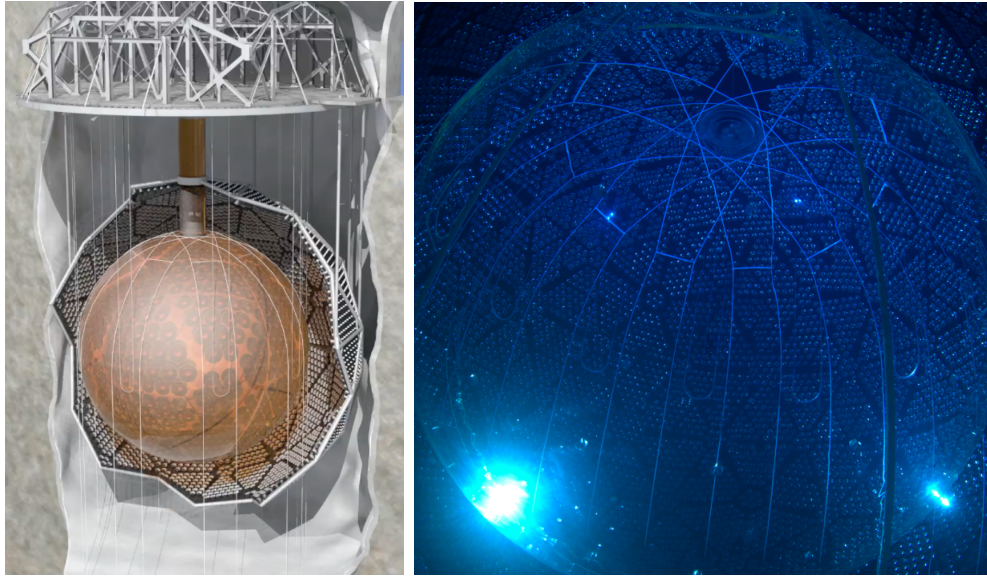


Figure 2.1: Left: the SNO+ detector. The cavity is filled with ~ 7000 -tonnes ultra pure water to attenuate radiogenic backgrounds from the rock. Right: picture taken from a camera mounted on the PSUP [36]. The PMT hexagon panels, hold-down ropes, and the bottom of the neck are clearly seen.

The third phase, the Te-loading phase, will suspend ~ 1.3 tonnes of ^{130}Te in the LAB for a search for the neutrinoless double beta decay. One of the most important advantages of this technique is that even a modest isotope loading percentage can yield a relatively high target mass. The high cost-effectiveness of this method has growing importance given the current weak evidence of normal hierarchy [37, 38, 39].

As of September 2019, SNO+ has successfully completed the water phase and is currently in the process of LAB fill. The results presented in this thesis are based on the water phase data.

2.2 Detection Principle in the Water Phase

2.2.1 Cherenkov Radiation

The primary detection mechanism during the SNO+ water phase is Cherenkov radiation, a type of electromagnetic radiation emitted when a charged particle travels through a medium at a speed faster than the phase velocity of light in that medium. The pattern of emitted photons is well characterized by the Cherenkov cone, whose angle (relative to the direction of the moving particle) can be written as:

$$\cos\theta_c = \frac{1}{n\beta}, \quad (2.1)$$

where n is the refractive index of the medium and $\beta = \frac{v}{c}$ is the relativistic velocity of the particle. For relativistic particles moving through water, $\beta \sim 1$ and $n = 1.33$, therefore $\theta_c = 41.4^\circ$.

The energy loss of the charged particle predominantly comes from ionization, which is described by the Bethe equation [16]:

$$-\left(\frac{dE}{dx}\right)_{\text{Bethe}} = \frac{4\pi k^2 e^4 n z^2}{m_e c^2 \beta^2} B(v); \quad (2.2)$$

and,

$$B(v) = \left(\frac{1}{2} \ln\left(\frac{2m_e v^2 \gamma^2 T_{\text{max}}}{I_2}\right) - \beta^2\right) - \frac{\sigma(\beta\gamma)}{2} - \frac{C(I, \beta\gamma)}{Z}, \quad (2.3)$$

where k is the Coulomb constant, n is the electron number density of the medium, z is the number of charges, and $B(v)$ is the sum of correction factors including considerations on ionization potential, density, and shell corrections.

The subdominant Cherenkov energy loss can be described by:

$$-\left(\frac{dE}{dx}\right)_{\text{Cher}} = \left(\frac{ze}{c}\right)^2 \int_{n\beta > 1} \omega - \left(\frac{\omega}{n\beta}\right) d\omega, \quad (2.4)$$

where ω is the photon frequency. The photon emission spectrum can be determined from Eqn. 2.4:

$$\frac{dN}{d\lambda dx} = 2\pi\alpha \left[1 - \left(\frac{1}{n\beta}\right)^2\right] \lambda^{-2}, \quad (2.5)$$

where α is the fine structure constant, and λ is the photon wavelength. The derived emission spectrum is continuous and its relative intensity per unit wavelength is anti-correlated (λ^{-2}) with the wavelength. This (plus the fact that human eyes are more sensitive to blue than violet [40]) results in the characteristic Cherenkov blue ($\sim 450\text{nm}$) glow in water.

Based on Eqn. 2.2 and 2.4, a relativistic electron of 1-10 MeV range will travel in water for about 0.5 cm per MeV, emitting ~ 200 Cherenkov photons per MeV.

2.2.2 The Photomultiplier Tube

Cherenkov photons emitted from charged particles traveling in the water volume are detected by the photomultiplier tubes (PMTs), which collect relevant time and charge information. The SNO+ experiments reuses ~ 9300 Hamamatsu R1408 PMTs [41] from SNO. Each PMT is of 20 cm diameter, and has a mushroom-shaped glass front. A thin photocathode layer is plated on the inside of the glass surface, from which incident photons can release photoelectrons through the photoelectric effect. The photoelectrons are focused by electric field down to a dynode stack, a series of electrodes that can produce multiple secondary electrons under high voltage. For

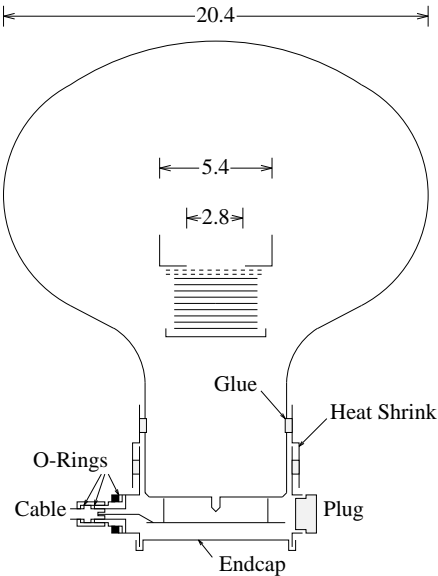


Figure 2.2: A schematic of the Hamamatsu R1408 PMT. The two dashed lines shows the focussing grid and the nine solid lines are layers of the dynodes. The bottom of the PMT is filled with silicone gel for airtightness. Dimensions are in cm. Figure is from [42].

the SNO PMTs, the potential difference between the photocathode and the anode is around 2000 V. Each of the 9 layers of dynode gives a factor of about 5 increase in the number of electrons, resulting in an overall amplification factor of about 10^7 .

The wavelength range that the photocathode is sensitive to is from 250 nm to 550 nm. The short-wavelength cutoff is determined by the transparency of the PMT glass. The quantum efficiency, defined as the fraction of incident photons which produce a photoelectron, is around 15% [41]. The total transit time inside the PMT from the photocathode to the anode is 30ns, with a spread around 1.5ns. The spread is mostly caused by different routes a photoelectron can take to reach the first dynode. A small contribution of about 0.2ns also comes from the difference between photoelectron energies. Additionally, a surrounding light concentrator, of 27cm diameter, is placed on every PMT that increases the overall photocathode coverage from 31%

to 54%.

2.2.3 The Trigger System

A fixed-size current pulse of $300 \mu\text{A}$ for each firing channels (PMTs) is sent through a 30 m long RG59/U type 75Ω cable to the trigger subsystems and finally, a Master Trigger Card (MTC), where the pulses are summed to be compared to a programmable threshold. The time window of the SNO+ primary trigger (NHIT100) for the trigger sum is set to 89 ns. This window is predominantly determined by the possible range of arrival times of direct photons on the ~ 9300 PMTs, which is calculated to be 77 ns for a 17 m sphere.

A global trigger is issued by the MTC if the trigger condition is met (There are in total 26 different independent trigger types including the NHIT100 trigger). This trigger is then passed to all crates on the next rising edge of a 50 MHz clock on the MTC. The time and charge information of any channels that have fired within the last 400 ns is then read out and stored in an underground buffer. The constraint on lowering the trigger threshold mainly comes from the read-out rate. With the expected increase of the light yield in SNO+ compared to SNO, the read-out boards and the data acquisition system were upgraded to have higher bandwidth. Thanks to this upgrade, during the SNO+ water phase the NHIT100 threshold was able to be lowered to 7 nhits (as opposed to 17 nhits for SNO, nhits is defined as the number of fired PMTs of the event), corresponding to a trigger rate in the range of 600 to 1000 Hz[43].

When a global trigger is received by the channels, the time and charge information are read out by analog to digital converters (ADCs). To translate the raw ADC

counts to physical time and charge units for each channel, two types of electronics calibration (ECA) are performed on a weekly basis: the charge pedestal calibration which finds the number of ADC counts that corresponds to zero charge; and the time slope calibration which uses an adjustable delay of the global trigger from the time of the pedestal pulse to convert ADC counts into nanoseconds.

2.3 Calibrations in the Water Phase

Calibration plays an important role in SNO+ in that it allows a thorough understanding of the detector response. Calibration is vital to event reconstruction such as position and energy, and therefore is the prerequisite for any sophisticated data analysis. The calibration in SNO+ is divided into three elements in hierarchical order from low-level to high-level:

1. Electronics calibration (ECA). This is the time and charge calibration on the low-level electronics channels, as described in Section 2.2.3.
2. PMT calibration (PCA), which corrects for the unknown offset of the ECA calibrated time between different PMTs. The offset comes from different cable lengths and pulse sizes. The effect of pulse sizes is such that bigger pulses tend to trigger the PMT earlier. An empirical function of time and charge is first fitted to each PMT by placing an isotropic light source (laserball) at a known location (the center of the detector) and calculating the time period for a photon propagating from the source to the PMT. The cable delay effect is then calibrated by collecting the PMT time residual distribution over many events with an external asynchronous trigger which can issue trigger regardless the status of the 50 MHz trigger clock.

3. Calibration of the detector's physics response, including the optical and energy response. In the water phase, the optical calibration (OCA) determines the attenuation and scattering properties of both the internal and external water as well as the PMT angular response. For energy calibration, γ -ray sources such as ^{16}N and $^{241}\text{Am}^9\text{Be}$ can be used to set the absolute energy scale and at the same time provide a measurement of the energy resolution as well as the spatial uniformity.

The deployable calibration sources can be put in different locations both inside and outside the AV using the calibration source manipulator system, shown in the schematic in Fig. 2.3. For the water phase, SNO+ reuses the SNO manipulator system with a few upgrades. The calibration source is mounted on a carriage, which provides attachment points for the central rope, umbilical, and two pulleys that the side ropes go around. A weight is also attached to the carriage to meet the minimum tension requirement for the ropes to function properly. Inside the AV, two sets of side ropes define two orthogonal planes on which the source can be moved to different points by adjusting the lengths and tensions of three attaching ropes (one central and two side ropes at any given time). The umbilical is a 30 m long, 6.3 mm radius silicone cable that provides necessary source utilities, including electrical wires, optical fibers, and inner tubes for gaseous source. Both the umbilical and the central rope are controlled by the Umbilical Retrieval Mechanism (URM), which consist of a compressed air system and a block and tackle system calibrated with shaft encoders and load cells (Fig. 2.4). The four side rope boxes use a similar mechanism as the URM, but are much smaller in size since there is no need to accommodate for the umbilicals. As shown in Fig. 2.5, an updated design was made for SNO+ where the side rope boxes

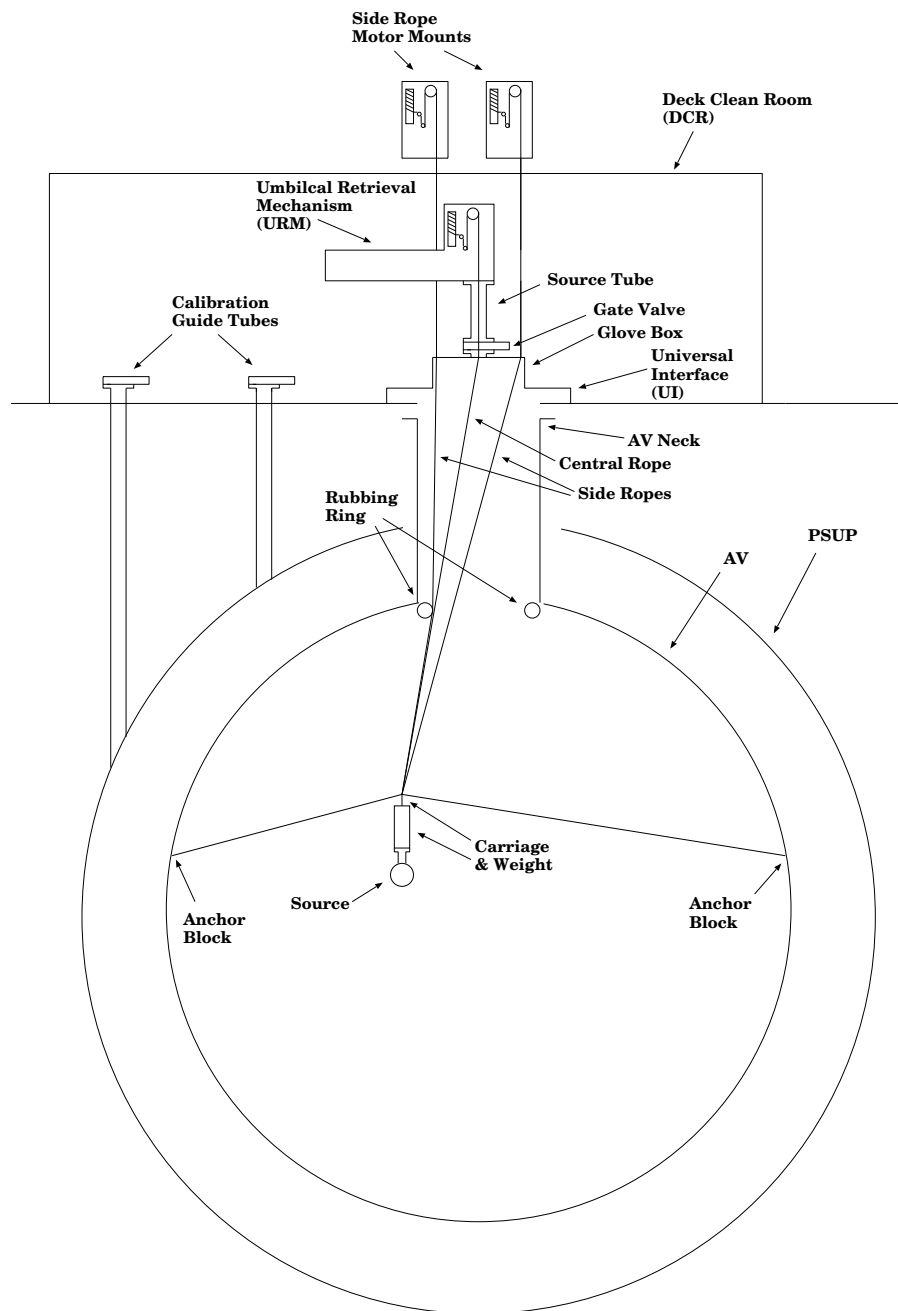


Figure 2.3: A schematic of the SNO+ calibration source manipulator system. A new design was made for the side rope boxes: instead of attaching to the ceiling, the boxes are now mounted directly on the UI. The UI also has a modified design where it is now mounted on the AV instead of the deck. Figure is from [42].

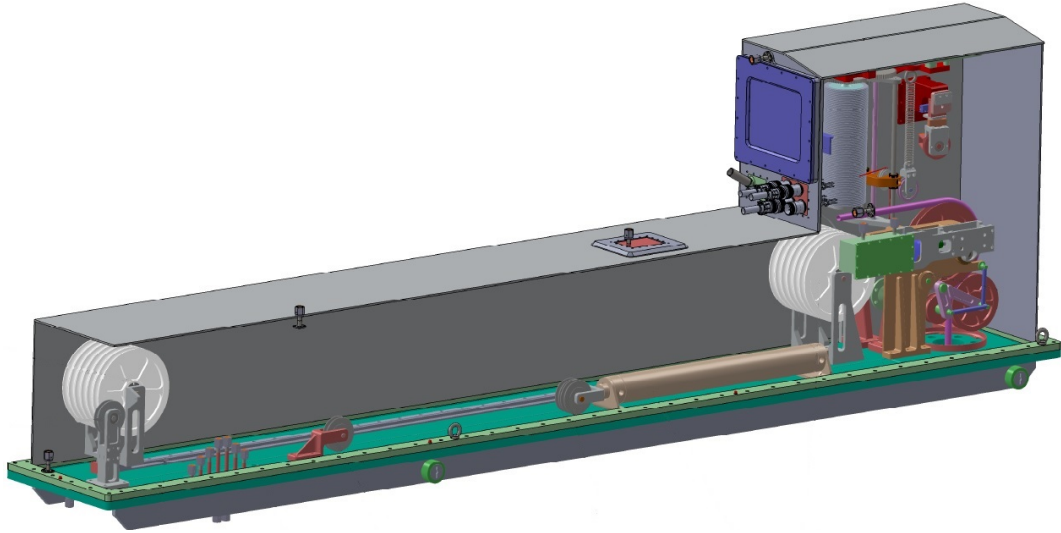


Figure 2.4: A side view of the scintillator phase URM, which preserves the essential design of the water phase URM. When not in use, the umbilical is stored between the two big pulleys in white. The central rope is mounted on the column in the right box, next to a block and tackle system. The compressed air system in brown provides power for playing out/in the umbilical. The system is calibrated with shaft encoders and load cells, shown in the right side of the figure. Figure is from [44].

are directly mounted on the UI instead of hanging from the ceiling. Three gate valves of different sizes (6-inch, 8-inch and 10-inch) on the UI and six calibration guide tubes on the deck are available for internal and external source deployment, respectively.

During the SNO+ water phase, the detector was extensively calibrated with multiple deployable sources to characterize the detector response, including laserball, ^{16}N , ^8Li , and $^{241}\text{Am}^9\text{Be}$. The laserball [46] and ^{16}N [47] resembled to large extent what were built in SNO, whereas the two other sources are significantly improved or modified for SNO+. The following subsections will describe each calibration except $^{241}\text{Am}^9\text{Be}$, which is discussed in more detail in Chapter 3.

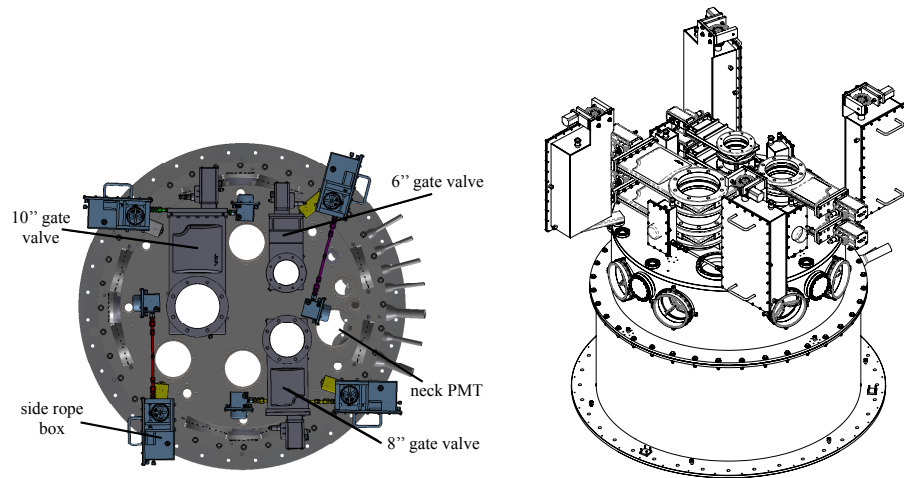


Figure 2.5: Left: Top view of the UI. Three gate valves, four neck PMTs, and four side rope boxes occupy most of the space on the UI. Right: Isometric view of the UI. Four glove box ports are available on the side of the UI for source handling. Figure is from [45].

2.3.1 The Laserball Calibration

The laserball is a 5 cm radius spherical quartz flask filled with silicone gel mixed with glass diffusers that diffuses the laser light roughly uniformly with a $\sim 10\%$ drop towards the top of the ball. It is connected through optical fibers with a pulsed dye laser driven by a nitrogen laser (Fig. 2.6) that produces light pulses with a wavelength of 337.1 nm and a duration of 0.6 ns with a pulse rate of ~ 100 Hz. Four dye cells are available to shift the light to wavelengths in the range of 337 nm to 650 nm. The intensity of the light can be adjusted by tuning two neutral density filters on the light path to the optical fibers that lead to the laserball. Just outside the laser box and before the entrance to the AV, the laser pulse is split to a photo-diode, which is then used to provide the external asynchronous trigger to the detector. Inside the AV, the optical fibers are embedded inside the umbilical for detector cleanliness and fiber

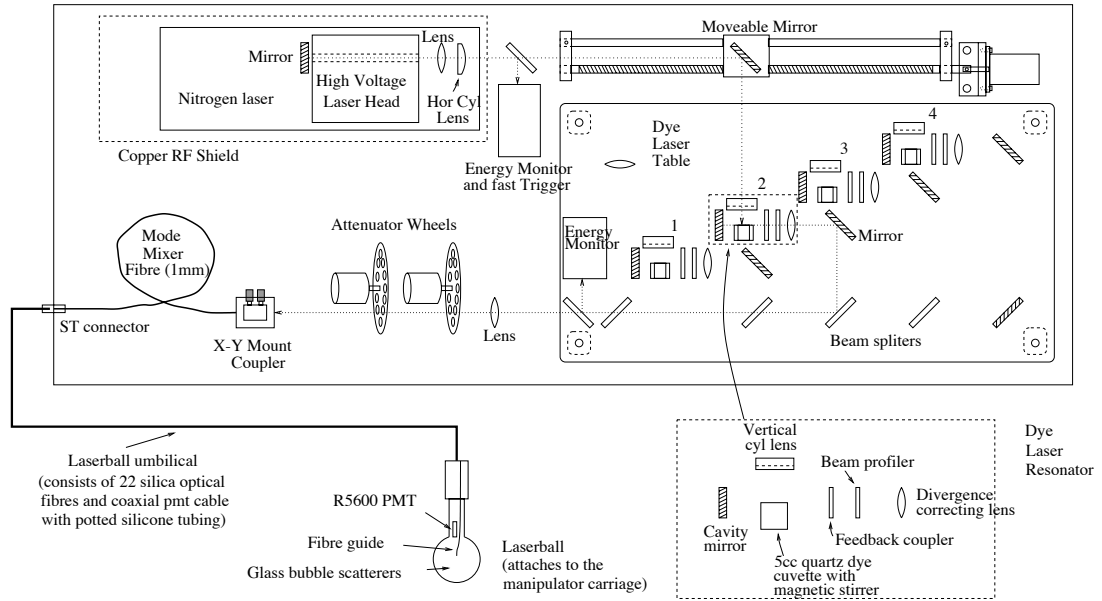


Figure 2.6: A schematic of the laserbox and laserball. Figure is from [42].

protection.

The laserball calibration data directly feeds into PCA and OCA.

2.3.2 The ^{16}N Calibration

The ^{16}N calibration is the principle energy calibration for the SNO+ water phase due to its unique advantage that the source events can be precisely tagged. ^{16}N beta decays to ^{16}O with a half-life of 7.1 seconds, with $\sim 73\%$ of decays producing an excited state of ^{16}O . About 92% of the γ -rays that are subsequently emitted due to de-excitation have an energy of 6.1 MeV. The β is used to tag the γ -ray propagating into the AV.

The ^{16}N gas is generated by piping CO_2 gas past a DT(deuterium-tritium) neutron generator located ~ 30 m away from the detector. The radioactive gas is then transferred in an inner tube of the umbilical into a 10 cm long and 5.7 cm radius



Figure 2.7: The ^{16}N source as implemented in the SNO+ simulation package. The blue box to the right represents the decay chamber. It is observed by a scintillation chamber (green) which also holds a PMT (black). Figure is from [48].

decay chamber that can be deployed in the detector (see Fig. 2.7). The cylindrical chamber is made from 5 mm thick stainless steel to fully shield the emitted electrons from entering the detector. The beta tag is generated by a 3 mm thick scintillator sleeve and a 5 cm PMT inside the decay chamber.

2.3.3 The ^8Li Calibration

The ^8Li source (Fig. 2.8) was also deployed in the water phase as a Cherenkov calibration source and the data was verified with the ^{16}N data. The primary goal of the ^8Li calibration is to calibrate the global light collection efficiency for later phases. ^8Li beta decays to ^8Be with a half-life of 838 ms. The electron energy spectrum is a continuum with an endpoint of ~ 13 MeV. The ^8Be is unstable and decays into two α s, which can be used to generate a global trigger to the detector.

Similar to the ^{16}N gas, ^8Li can be generated using the DT generator, this time in conjunction with a ^{11}Be target. The ^8Li atoms are then transported by helium

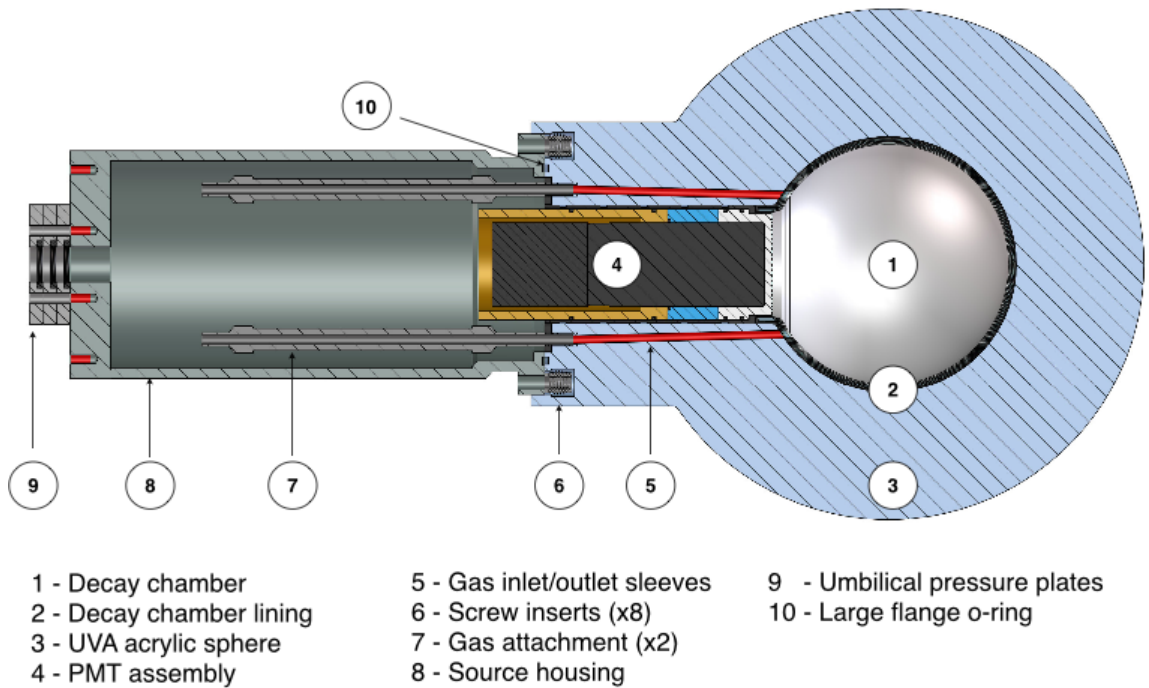


Figure 2.8: The SNO+ ^8Li source design. Figure is from [49].

gas through the umbilical to a spherical decay chamber, which is surrounded by a 6 cm thick acrylic sphere. The energetic electrons are stopped in this acrylic wall and produce Cherenkov light. A 2 cm PMT in the neck of the source is used to detect scintillation light from the alphas moving in helium gas.

2.3.4 ELLIE

One of the many important upgrades for SNO+ from SNO is the Embedded LED/Laser Light Injection Entity (ELLIE) system [33]. It uses light from fast pulsing LEDs/lasers that are mounted at fixed locations on the PSUP. The ELLIE system has three modules: TELLIE, which constitutes part of the PCA calibration and measures the PMT timing offset; SMELLIE, which measures the scattering properties of the detector

volume; and AMELLIE, which measures the absorption as well as the optical degradation. The ELLIE system is primarily intended for the liquid scintillator and Te-loading phase, nonetheless, some of the hardware was commissioned and tested during the water phase.

2.4 Software and Data Stream

The SNO+ experiment uses the Reactor Analysis Tools (RAT) for both Monte Carlo simulation and data analysis. This framework is written in C++ and based on GEANT4 [50], ROOT [51] and GLG4sim [52]. The former two softwares are widely used in the particle physics community while the last one is designed for general liquid scintillator neutrino experiments. The GLG4sim is predominantly used for the optical photon handling and the GEANT4 library is responsible for all other physics processes as well as the command interpreter and compilation system. ROOT is used to manage data structure and I/O. The RAT library, which is specific for SNO+, includes a detailed geometry description of the detector, a simulated data acquisition system, the optical properties of different detector volumes and multiple event reconstruction and classification algorithms.

The raw data in SNO+ is collected in the ZEBRA¹ data analysis banks (ZDAB) file format. Low-level calibration and data processing in RAT transforms the raw data into the ROOT data structure, with each event containing a list of hit PMTs with calibrated time and charges. Other utilities such as event reconstruction and classification can be applied either at the same time as the data processing or at a later time. Additionally, a portable ROOT ntuple file consisting only event-level (as

¹ZEBRA is a memory management and high efficiency I/O system that was developed by CERN [53].

opposed to PMT-level) information is also produced for quick access.

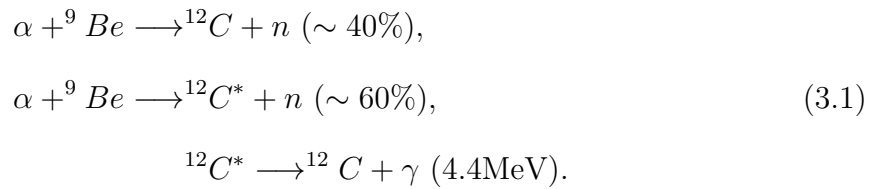
As is most software in particle physics experiments, RAT is a collaboration-wide effort that is under constant development. Unless otherwise stated, the results included in this thesis should be referenced to a tagged version of RAT, 6.16.4.

Chapter 3

The $^{241}\text{Am}^9\text{Be}$ Calibration

3.1 The $^{241}\text{Am}^9\text{Be}$ Source

The $^{241}\text{Am}^9\text{Be}$ calibration source is a kind of α -induced neutron sources that is widely used in particle physics experiments. Eqn. 3.1 explains the neutron production process of this source. The α -particle emitted by ^{241}Am (half-life of 432.2 years) can be absorbed by the ^9Be target, and produces a ^{12}C nucleus through neutron emission. As an order of magnitude estimate of the reaction cross-section, about 80 neutrons are produced for every one million α particles [54]. Subject to the source internal setup, $\sim 60\%$ [55] of the time the ^{12}C nucleus is produced in the first excited state, which will immediately de-excite and emit a 4.44 MeV γ . Other higher excited state decay channels include 7.65 MeV and 9.64 MeV γ s, but the branching ratios (highest at 0.04% for the 7.65 MeV γ) are negligible in the context of SNO+.



In the SNO+ detector, the 4.4 MeV γ propagating outside of the source will produce energetic electrons via Compton scattering. These electrons emit Cherenkov photons along their path and are then detected by the PMTs. The neutron, on the other hand, takes time to thermalize and random-walk by colliding with other nuclei, and eventually captures on a hydrogen atom (a sub-percent of the neutrons will capture on oxygen instead), releasing a 2.2 MeV γ . There is a strong time and position coincidence between the 4.4 MeV γ and the neutron capture signal.

Performing the $^{241}\text{Am}^9\text{Be}$ calibration in the SNO+ water phase was highly desirable. Firstly, the calibration is instrumental to understand the detector response to neutrons. During the water phase, SNO+ operated at an energy threshold as low as ~ 1.5 MeV, which means that not all neutrons triggered the detector. The calibration permitted an accurate measurement of the neutron detection efficiency. Secondly, the time difference distribution between the prompt and delayed signals is highly sensitive to the neutron capture time constant, and can be analyzed to infer the neutron capture (on hydrogen) cross-section. Thirdly, the 4.4 MeV γ gives an additional energy calibration point beside the ^{16}N calibration, and can be used to cross-check the energy scale, energy resolution, and energy linearity. Last but not least, as a result of the similarity between the $^{241}\text{Am}^9\text{Be}$ source signal and the antineutrino signal, this calibration can be important in understanding the parameter space in search for reactor antineutrinos in water.

The source used in the SNO+ calibration is a veteran SNO powder source (SNO-LAB source ID: SLB024 [57]), which was produced by LEA Cerca, France in 2005. As is shown in Fig. 3.1, the original source was doubly encapsulated with stainless steel as part of the standard manufacture procedure. An additional two layers of

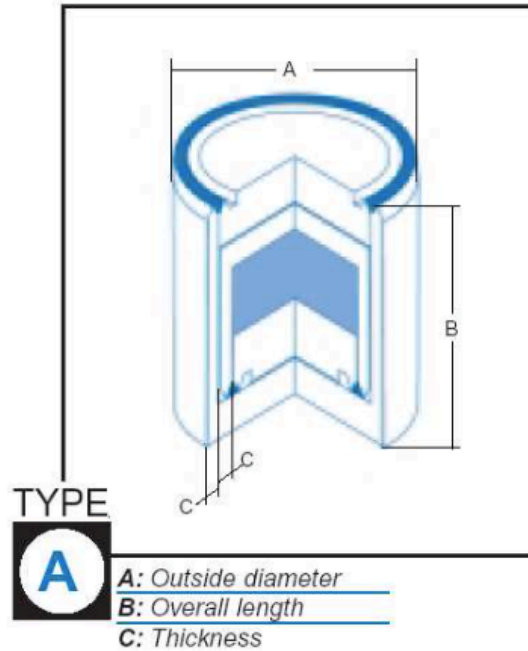


Figure 3.1: Original package for the SLB024 $^{241}\text{Am}^9\text{Be}$ source. The size specification are: $A=8\text{mm}$, $B=10\text{mm}$, and $C=0.8\text{mm}$. Figure is from [56].

black O-ring sealed Delrin (Polyoxymethylene) were added by the SNO experiment for source deployment to ensure the cleanliness and compatibility of the source-stem connection. Per SNOLAB radiological source encapsulation policy [58], the SNO encapsulations are to stay permanently on the source. Detailed drawings of the SNO encapsulations can be found in Fig. 3.2.

The source has a nominal strength of 1683.33 kBq, and a documented neutron rate of 66 Hz [57]. In-situ measurement in SNO determined the neutron rate to be 68.70 ± 0.74 Hz in 2008 [59]. This can be translated to 67.39 ± 0.72 Hz at the time of the SNO+ water internal deployment.

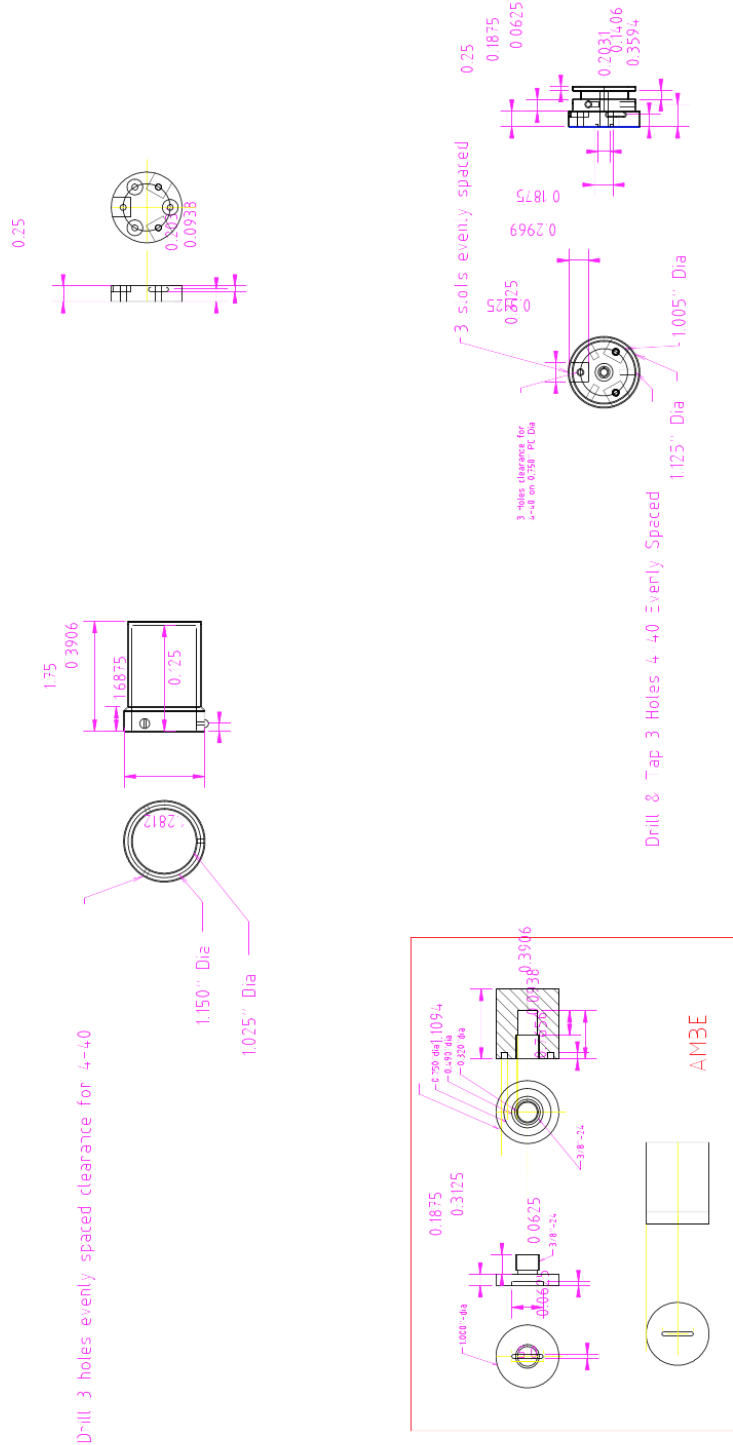


Figure 3.2: The SNO encapsulations on the $^{241}\text{Am}^9\text{Be}$ source. The inner layer of the encapsulation is shown in the red box.

3.2 The New Encapsulation

After the SNO experiment finished, the source was securely stored in the underground lab at SNOLAB, but has been used in other SNOLAB experiments. In the spirit of absolute source cleanliness, a new layer of encapsulation was proposed, designed and fabricated for the deployment in the SNO+ water phase. This new encapsulation is considered to be “temporary” and made demountable, since another encapsulation [60] comprised of lead and stainless steel is already under planning for the liquid scintillator phase.

3.2.1 Design and Fabrication

The design of the encapsulation can be found in Fig. 3.3. The entirety of the encapsulation was made of Delrin to avoid high energy γ s being emitted from neutron capture on stainless steel. The screws and the nuts are made of 316 stainless steel and the wires used to secure the screws are made of 18-8 stainless steel. A low background Butyl O-ring that was leached and counted by SNO was used to seal the can and the cap.

Besides the cleanliness of the source, The main focus of the encapsulation design is to minimize the risks of losing parts of the encapsulation during deployment. Several design features are made to fulfill the purpose. The can is designed to have an inner diameter and height that will securely fix the position of the source inside the encapsulation. Three lockable screws on the edge of the can are used to safeguard the enclosure. These screws are connected by a 0.036” diameter wire using the single-wire method in the aerospace procedure [61]. This prevents the possibility that the screws can untighten themselves from the nuts during the deployment. Special care

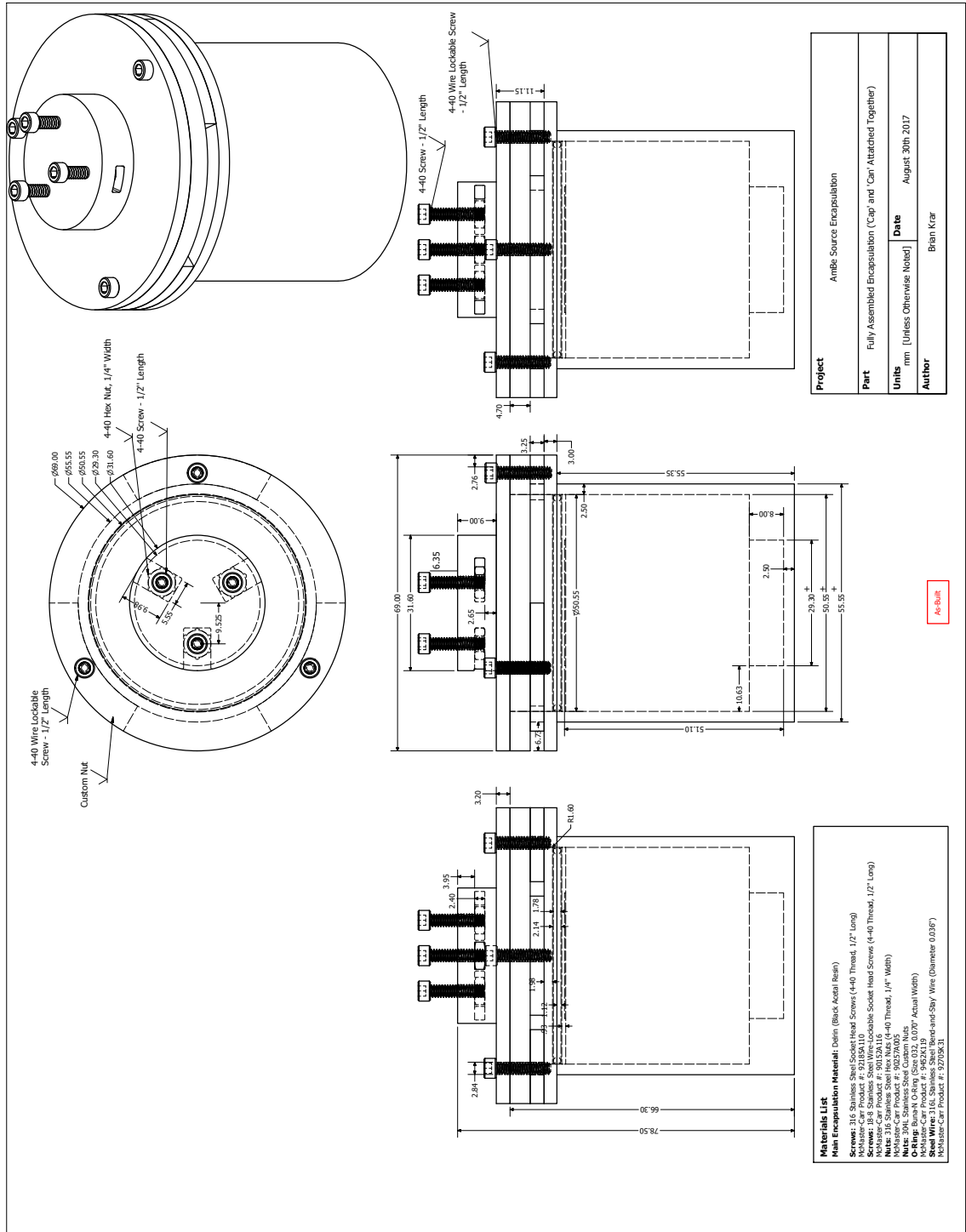


Figure 3.3: Engineering drawing of the new encapsulation for the $^{241}\text{Am}^9\text{Be}$ source. Figure is from [56].

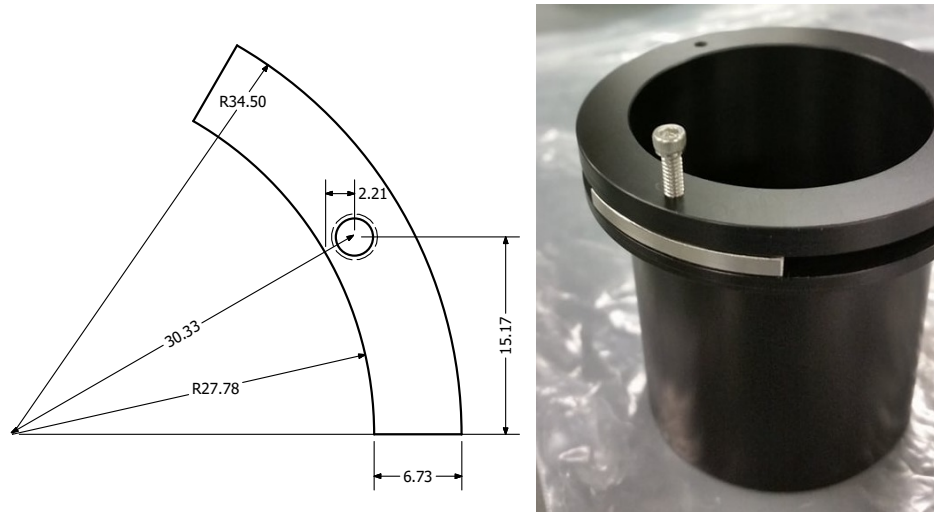


Figure 3.4: The specially designed nuts that fills the space between the upper and lower lips. Figure is from [56].

is exercised to not overtighten the screws to break the Delrin threads. The nuts that are mounted on each screw have a specially designed shape that precludes the self-rotation of the nuts (Fig. 3.4).

As is shown in Fig. 3.5, the standard “captured nut” structure in SNO [42] is adopted for the top of the cap for compatibility with the SNO source-stem connection. Three hex nuts are inserted into three manufactured slots with one side of the hex nuts directly against the slot edge, so that the rotation of the nuts is restricted. After mounting the screws onto the nuts, the screws are wired with the same wiring technique.

In this design, the air inside the encapsulation will be compressed during the assembly process. A simple calculation yields the change in pressure to be 15 psi, which is well within the design threshold (60 psi). As a matter of fact, this pressure difference will offset against the compression pressure from the water during the deployment.



Figure 3.5: The “captured nut” structure. Figure to the left is from [56].

The Delrin can and cap, as well as the special nuts were machined at Queen’s University in August 2017. UPW (ultra pure water) and methanol wiping was applied immediately after the machining. Other encapsulation parts including the screws, nuts, wires, and Buna O-rings for test purposes are ordered from McMaster-Carr Supply Company (See Appendix A).

3.2.2 Pre-deployment Tests and Cleaning

To reduce deployment risks, the source encapsulation underwent extensive leak-checking tests and cleaning prior to the deployment.

Pressure Test

The primary leak-checking test for the source encapsulation is the so-called pressure test, where a similar environment during source deployment is simulated. The encapsulation was assembled with a “dummy source” (a small Delrin cylinder that has a similar size as the source) inside to create comparable internal air pressure. The

encapsulation assembly was then placed under water inside a 1m high aluminum vessel. For cleanliness, the encapsulation assembly was sealed inside a polyethylene bag filled with deionized water. The vessel was enclosed to sustain water pressure, with the exception of a valve that was connected to faucet water.

The encapsulation assembly was kept under 60 psi for 1 hour before the vessel was opened. Nitrogen gas was used to blow dry the external surface of the encapsulation after the source assembly was retrieved and before the encapsulation was disassembled. Careful inspection of the interior revealed no sign of leakage. The pressure test validates the soundness of the conceptual design and fabrication of the source encapsulation.

Bubble Test

Bubble test is a complementary leak-checking test that is designed to safeguard the integrity of the final source assembly. After the cleaning procedures (see Section 3.2.2) on both the source and the encapsulation, and immediately before the source entering the detector, a successful bubble test gives the final green light for this deployment. To perform the test, the source assembly which is assembled at an ambient temperature of about 20°C is kept in a ziplock polyethylene bag filled with ~40°C UPW for 10 mins, during which time the bag is under constant scrutiny. The source assembly is deemed leakproof if no bubbles is observed. As opposed to the one-time pressure test, the bubble test needs to be performed prior to every deployment.

Cleaning Procedure

Different from the “grandfathered” laserball and ^{16}N calibration sources which were inherited from SNO and have been stored in a clean manner, the $^{241}\text{Am}^9\text{Be}$ encapsulation is new and made from off-the-shelf material. Therefore, a thorough cleaning procedure is prepared to meet the SNO+ background criteria and cleanliness standard in the water phase. This procedure was later adapted for subsequent water calibration source deployments, such as ^8Li [49].

At least two persons are required to undertake the cleaning procedure: an operator and an observer. The operator is the individual with primary responsibilities on most of the cleaning operations, while the observer is responsible to fill in the checklist, provide help if appropriate, and observe (e.g. if the operator unknowingly touched any unnecessary objects).

The cleaning procedure started as soon as the encapsulation machining was done. Once the parts were machined, they were ultrasonically cleaned with Alconox [62] to remove any machining grease. Afterward, they were sprayed with 10% isopropyl solution, soaked and rinsed with distilled water and sprayed with methanol to remove the detergent residues. Except during the pressure test, all encapsulation parts were double-bagged before they were shipped to the underground lab at SNOLAB, where several rounds of additional cleaning took place. The encapsulation parts were ultrasonic cleaning with Radiacwash [63], UPW soaked and rinsed, and methanol sprayed. The $^{241}\text{Am}^9\text{Be}$ source, on the other hand, was only sprayed with Alconox, soaked and rinsed in UPW, and finally sprayed with methanol. The source and encapsulation were assembled in a clean manner, after which similar cleaning procedures as the source itself were applied to the assembly. The source assembly was cleaned for a final

time before connecting the source to the umbilical (after the bubble test). Detailed cleaning procedure and a step-by-step checklist can be found in [56].

Ultrasonic cleaning is one of the most effective techniques for decontamination. Different detergents are chosen at different stages of the cleaning process. Alconox is a type of alkaline detergent that is best used to remove grease or machine oils, whereas Radiacwash is very efficient at removing radioactive contaminants. The cleaning procedure imitates the standard SNOLAB ultrasonic cleaning protocol, which includes three repetitions of 1-hour ultrasonic cleaning. Before the first repetition, the cleaner is heated to 60°C and is degassed for 5 mins. This degas step removes the gases in the cleaning solution so that full cavitation energy can be directed towards cleaning the parts. After each repetition, the cleaner is emptied, rinsed and refilled with UPW. The last two repetitions are put in place to remove any residues from the detergent itself.

3.3 The Source Deployment

Two $^{241}\text{Am}^9\text{Be}$ calibration campaigns were carried out during the water phase. The calibration scanned through many positions both inside and outside of the AV. Fig. 3.6 shows the deployed source positions. Table 3.1 additionally lists the duration and measured neutron detection efficiency for all the internal runs, which will be discussed in details in the following chapter.

3.3.1 Internal Deployment

The first $^{241}\text{Am}^9\text{Be}$ calibration campaign [64] took place on January 19th, 2018, with the source deployed at 23 different positions inside the AV. Prior to the $^{241}\text{Am}^9\text{Be}$

Run no.	T (h)	x (cm)	y (cm)	z (cm)	Efficiency (%)
109133	0.93	0.0	-0.04	-0.10	48.3±0.3
109134	0.94	0.0	-0.04	-0.10	48.4±0.3
109135	0.93	0.0	-0.04	-0.10	48.0±0.3
109137	0.51	0.0	440.55	-0.90	47.7±0.4
109140	0.48	0.0	297.85	-0.31	49.2±0.4
109144	0.49	0.0	149.68	-0.02	49.3±0.4
109147	0.50	0.0	-149.03	-0.27	48.5±0.4
109150	0.50	0.0	-299.08	-2.24	49.9±0.4
109153	0.49	0.0	-399.81	-2.30	48.7±0.4
109159	0.48	0.0	-260.90	-260.81	50.5±0.4
109156	0.51	0.0	259.92	-260.51	50.0±0.4
109214	0.49	0.0	148.34	-150.04	50.3±0.4
109217	0.49	0.0	-148.31	-150.11	49.6±0.4
109220	0.48	0.0	-149.56	150.27	49.0±0.4
109223	0.55	0.0	149.63	150.04	49.3±0.4
109162	0.48	0.0	-0.07	-549.89	47.3±0.4
109165	0.47	0.0	-0.11	-499.93	48.4±0.5
109171	0.50	0.0	-0.30	-450.24	49.3±0.4
109168	0.48	0.0	-0.04	-299.91	51.0±0.4
109211	0.51	0.0	-0.06	-150.07	50.2±0.4
109208	0.48	0.0	-0.04	149.91	48.1±0.4
109174	0.48	0.0	-0.01	300.33	47.9±0.4
109178	0.51	0.0	0.01	450.71	43.9±0.5
109226	0.48	0.0	4.60	511.46	40.9±0.5
109181	0.49	0.0	-1.08	550.23	34.7±0.6

Table 3.1: The duration and source position of all internal $^{241}\text{Am}^9\text{Be}$ runs. The runs are subdivided into four groups (indicated by the solid lines). The first three runs are collected with the source at the center of the detector; the second group is a y-axis scan; the third group is a diagonal scan in the y-z plane; and the last group is a z-axis scan.

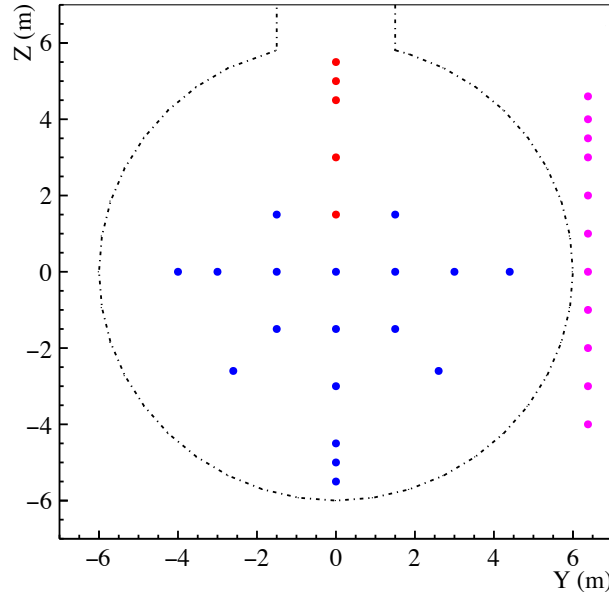


Figure 3.6: A schematic of the $^{241}\text{Am}^9\text{Be}$ calibration source positions.

calibration, the detector was running PCA with the laserball at the center. To evaluate background coming from the umbilical and the source, a 30 min “background” run was taken with the laserball at the center of the detector while the laser was off. This background run was disrupted by a breakdown of one PMT towards the end of the run.

After the background run, the laserball was pulled out from the detector using the calibration source manipulator system. The $^{241}\text{Am}^9\text{Be}$ source assembly was attached to a 31.2 cm long Teflon (polytetrafluoroethene, PTFE) stem, which was then connected to the carriage and the umbilical. Fig. 3.7 shows the source assembly moment before it was deployed.

Using the manipulator system, the $^{241}\text{Am}^9\text{Be}$ source was retracted into the source tube, which was then mounted onto the UI again. Afterwards, the 10-inch gate valve



Figure 3.7: The $^{241}\text{Am}^9\text{Be}$ source assembly was attached to the stem and carriage. The umbilical and central rope were still mounted on the URM, but can be seen to the left side of the figure.

was opened to drive the source into the neck. The side ropes located on the y - z plane were attached to the carriage through the glove ports on the side of the UI. Several test drives were done to make sure that the umbilical and the rope system were functioning as expected.

A special run type, “AMBE”, was created for the calibration, although the trigger settings were the identical to the normal detector data-taking one. A simple script [65] to identify time coincidences that runs directly on the raw data stream (zdab files) was also prepared for real-time diagnosis. The script was calibrated with the background

run taken earlier, which gave an accidental coincidence rate of 0.05 Hz. To study the trigger effect, each $^{241}\text{Am}^9\text{Be}$ calibration run was followed by a ~ 5 min nhit monitor run [43] that can be used to derive the trigger efficiency curve.

The $^{241}\text{Am}^9\text{Be}$ source was first placed at the center of the detector for 3 hours. A significant coincidence rate (~ 8 Hz) above background was observed. After the central runs, the source was moved to other positions in the YZ plane. Within 4.5m from the center, the source positions were separated by 1.5m. From 4.5m to the edge of the AV, smaller steps were taken to carefully map out the neutron detection efficiency changes.

Due to limitations of calibration personel resources, 16 different positions were scanned with the $^{241}\text{Am}^9\text{Be}$ source before it was parked in the glove box (~ 6 m above the top of the AV), and the detector was switched back to take physics data. An additional seven different positions were scanned at the first available opportunity next week. In total, about 0.5 million coincidence pairs (estimated using the coincidence script) were collected.

The source assembly was extracted from the detector on January 23th, 2019. Careful inspection of the disassembled encapsulation showed no sign of leakage.

3.3.2 External Deployment

Preliminary analysis of the internal $^{241}\text{Am}^9\text{Be}$ calibration data revealed that there was no significant drop of the neutron detection efficiency at higher radii except when the source was close to the neck. In light of this observation, a proposal for an external $^{241}\text{Am}^9\text{Be}$ calibration [66] was made in an attempt to increase the fiducial volume for the reactor antineutrino search. It also had the potential to contribute to the

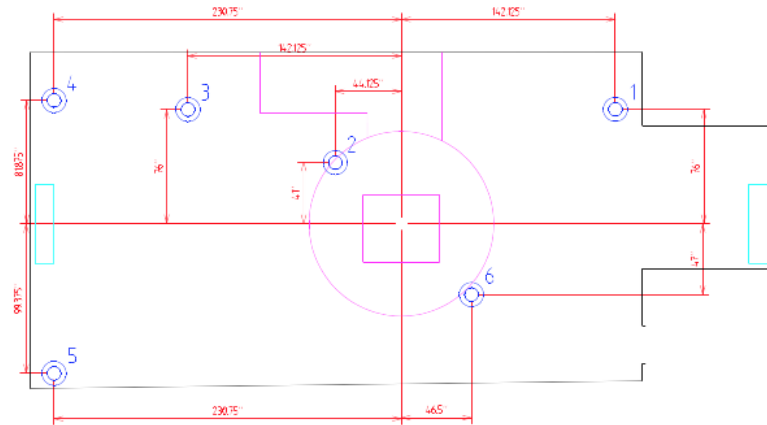
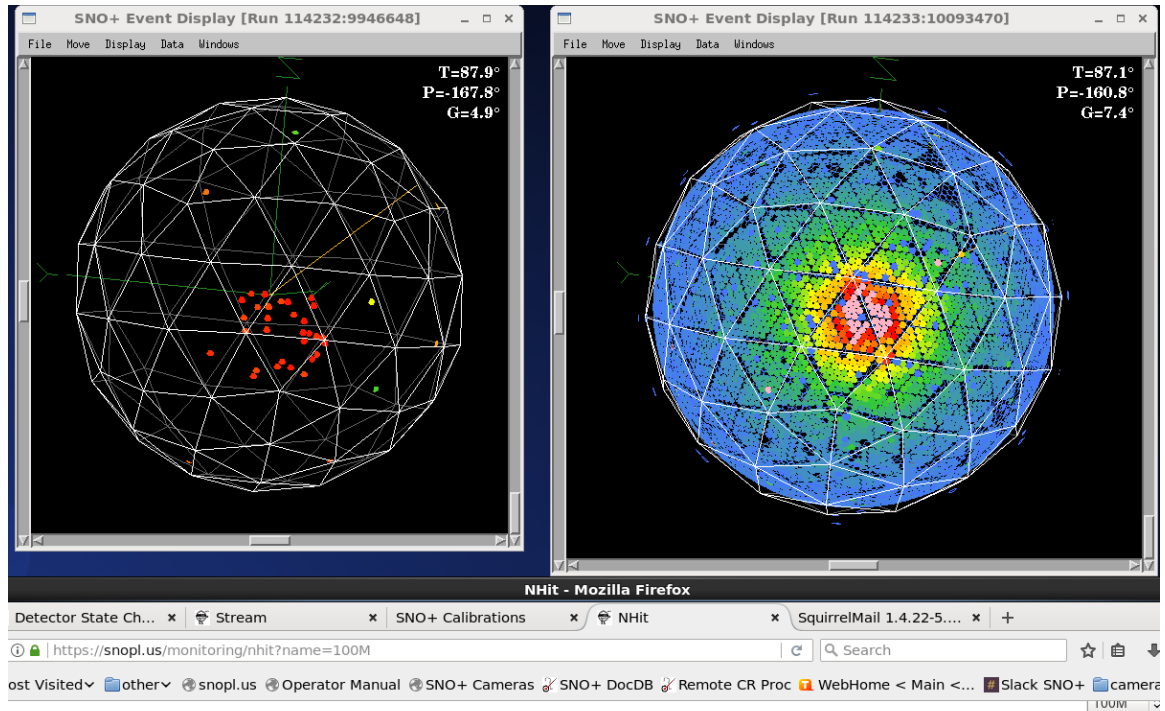


Figure 3.8: A schematic of the SNO+ deck floor. In total six vertical guide tubes (small blue concentric circles) are available for external source deployment. The UI is shown as a purple circle. These guide tubes are made of stainless steel and provide access through the PSUP to the AV. Guide tube 5 was used for the external $^{241}\text{Am}^9\text{Be}$ calibration. Figure is from [42].

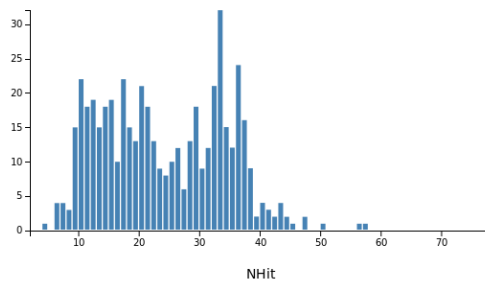
external energy calibration, which is important to understand the optical properties of external water and the AV.

On June 25th, 2018, the $^{241}\text{Am}^9\text{Be}$ source was deployed again, this time through a vertical guide tube (Fig. 3.8) that provides access to the cavity outside the AV. The closest distance from the source to the AV, 38 cm, occurs when the source is in the same horizontal plane as the detector center ($z=0$ m). The calibration data was taken at 11 different positions spaced 1 m apart vertically, with the furthestmost position 1.87 m away from the AV. At this point, a factor of 5 reduction of the coincidence rate was observed compared to that at $z=0$ m. Fig. 3.9 shows some event displays from the detector monitoring tools during the deployment.

As is the case for internal calibration, the nhit monitor was run after every source run. Additionally, two different threshold settings were tested during the external calibration to better understand the systematics associated with the trigger threshold



NHit (10 seconds)



NHit (60 seconds)

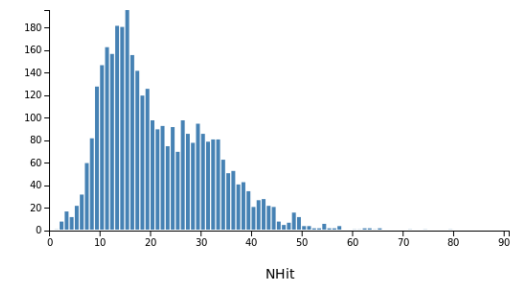


Figure 3.9: Event displays during an external $^{241}\text{Am}^9\text{Be}$ calibration run at $z=0$ m. Top left: PMT hits of a prompt event (4.4 MeV γ); Top right: color-coded sum of PMT hits for a duration of 10 min. Events are seen to be clustered at where the source was placed; Bottom: nhits spectra over a 10 s and 60 s period, respectively. The peak at around 30 nhits indicates that the 4.4 MeV prompt γ s were collected.

and trigger efficiency curve. Although plenty of coincidence signals were observed for the external calibration, interpretation of the data is still under development due to the changes in threshold setting. Therefore, the analysis results of the external $^{241}\text{Am}^9\text{Be}$ calibration data are not presented in this thesis.

Chapter 4

Minimalistic $^{241}\text{Am}^9\text{Be}$ Data Analysis

A novel, minimalistic analysis method utilizing the statistical separation of $^{241}\text{Am}^9\text{Be}$ signal events from accidental backgrounds is designed to extract important information such as the neutron properties and detector performance indicators. These include the neutron capture (on proton) time constant at room temperature, the neutron capture cross-section, and the neutron detection efficiency. As opposed to the traditional analysis method [67] [68] [69] where stringent cuts are applied to the $^{241}\text{Am}^9\text{Be}$ data to obtain a very pure coincidence event sample, the method presented here treats the purity of the coincidence selection as a parameter to be directly fitted. As a result, a large fraction of signal events in the calibration data is preserved in the analysis, thus reducing the statistical uncertainties of the measurements.

4.1 Analysis Method

One of the distinguishing features of the $^{241}\text{Am}^9\text{Be}$ signal (the γ -neutron coincidence) from backgrounds (random accidental background events) is that the time difference of the former follows a sharp exponential decay with a constant associated with the neutron-proton capture time ($\sim 200 \mu\text{s}$). On the other hand, under the assumption

that the background event rate is a constant, the accidental backgrounds have the time difference distribution of a Poisson process. Despite that the time difference between accidental backgrounds still follows an exponential form, the distribution has a much larger time constant that is determined by the detector event rate (~ 500 Hz, or ~ 2000 μs). The distinction in the two time difference distributions proves to be a powerful tool for isolating signal events from accidental backgrounds; a statistical separation method is thus made possible.

A histogram of 10 μs bin size can be filled with the time differences between an suitable event (referred to as the prompt candidate, detailed selection criteria discussed below) and the event right after it (referred to as the delayed candidate), where both candidates are selected with a minimum value of nhits. Note that this filling method does not exclude the possibility where an event can be the delayed event in one coincidence pair and the prompt event in another. Such a histogram should be well fitted by some combination of a few exponentials (it turns out that a sum of two exponentials is enough to describe it) which presumably consists of parameters of interest such as the neutron detection efficiency E , the purity of the prompt selection P , the detector event rate R_2 , and the neutron capture constant λ ($\lambda = \frac{1}{\tau}$).

The neutron detection efficiency, defined as the ratio between the number of neutrons in the delayed candidates and the number of correlated 4.4 MeV γ s in the prompt candidates, is the probability that the detector triggers on a neutron signal. Due to the low energy nature of the signal, the detection efficiency is very sensitive to the detector trigger threshold as well as the delayed candidate nhits cut applied in the analysis. It can be shown later that the lowest practical nhits cut for delayed

candidates, which produces the highest neutron detection efficiency, turns out to be 4 in the analysis. The main limitation comes from the stability of the fit performance as the accidental background rate becomes volatile at low thresholds. The purity of the 4.4 MeV γ selection, P , is defined as the proportion of the 4.4 MeV γ s in the prompt candidates. Because the backgrounds have a different nhits spectrum than the 4.4 MeV γ s, P is also dependent on the prompt candidate nhits cut, although the correlation is much weaker compared to the case of neutrons. λ , on the other hand, is a physical constant and stays undisturbed except for temperature variations. Data collected from different source positions can be combined to increase the statistical precision of the neutron capture constant.

4.1.1 Derivation and Interpretation of the Fit Function

The fit function for the time difference histogram is given below:

$$F(t) = N \cdot R_1 (P \cdot E \cdot (\lambda + R_2) e^{-(\lambda + R_2)t} + (1 - P \cdot E) \cdot R_2 e^{-R_2 t}), \quad (4.1)$$

where N is a normalization coefficient and R_1 is the prompt candidate rate.

During the $^{241}\text{Am}^9\text{Be}$ source deployment, events in the detector can be traced to two origins: a small fraction is the signal events from the radioactive source with a rate in the order of magnitude of ~ 10 Hz, while most other events are from random particle decays or cosmic radiations, which can be referred to as the backgrounds. Of these background events most are unrelated in time. Some background events that are especially perilous to this analysis are the so-called (α, n) reaction in the water, which creates time coincident pairs that can not be distinguished from the source

events. However, thanks to the cleanliness of the detector, the rate of these time-correlated backgrounds is estimated to be at least 10^6 times less than the $^{241}\text{Am}^9\text{Be}$ source event rate [70] [71], and therefore the effect is negligible in this analysis.

Since the prompt and delayed candidates are selected with only nhits criteria, it is possible that one or two events in the candidate pairs is misidentified. Events in the coincidence candidate pairs can be tagged as *True* (or *False*) if it is correctly (falsely) identified as the source event. Specifically, the prompt candidate is tagged as *True* if it is the 4.4 MeV γ emitted from the source, and the delayed candidate is tagged as *True* if it is the neutron signal (2.2 MeV γ). With this classification, every coincidence candidate pair falls into one of the following four categories:

- *True-True* event pair: the prompt event is the 4.4 MeV γ , and the delayed event is a source neutron.
- *True-False* event pair: the prompt event is the 4.4 MeV γ , but the delayed event is a background event.
- *False-True* event pair: the prompt event is a background event, but the delayed event is a source neutron.
- *False-False* event pair: both the prompt and delayed events are background events.

A naive intuition is that the time difference distribution of the *True-True* event pairs would be similar to that of an exponential decay of λ ; however, a subtlety presents. It arises from the intrinsic implication that for *True-True* event pairs there has to be no background event occurring in between the *True* γ and the neutron. As

a result, the expression for the *True-True* event pairs can be written as:

$$\begin{aligned}
 \text{Prob}_{\gamma-n \text{ before } b}(t) &= P \cdot E \cdot \lambda e^{-\lambda t} \cdot \left(1 - \int_0^t R_2 e^{-R_2 t'} dt'\right) \\
 &= P \cdot E \cdot \lambda e^{-\lambda t} \cdot e^{-R_2 t} \\
 &= P \cdot E \cdot \lambda e^{-(\lambda+R_2)t},
 \end{aligned} \tag{4.2}$$

where $P \cdot E$ is the normalization factor for the *True-True* event pairs and the last term in this equation denotes the conditional probability.

As for the *True-False* event pairs, two subsidiary scenarios need to be considered. The first scenario is where the associated neutron does not trigger the detector or satisfy the minimum nhits requirement. In this case the time difference distribution of the pairs will be a simple exponential that solely relates to the detector event rate:

$$\text{Prob}_{\gamma-b \text{ no } n}(t) = P \cdot (1 - E) \cdot R_2 e^{-R_2 t}. \tag{4.3}$$

The second scenario, which in some sense ties closely to the *True-True* event pairs, occurs when the associated neutron passes the delayed event selection criteria, but does not make into the event pair because a background event (or more than one background events - although those would be rather rare and only cause second-order effect) happens to appear before the neutron. Similarly this constitutes as a conditional probability, and the exponential expression for this scenario is (only considering first-order effect):

$$\begin{aligned}
 \text{Prob}_{\gamma-b \text{ before } n}(t) &= P \cdot E \cdot R_2 e^{-R_2 t} \cdot \left(1 - \int_0^t \lambda e^{-\lambda t'} dt'\right) \\
 &= P \cdot E \cdot R_2 e^{-(R_2+\lambda)t}.
 \end{aligned} \tag{4.4}$$

This can be viewed as a competing process with the case of *True-True* event pairs. Both have the same exponential constant and can be combined:

$$\text{Prob}_{\gamma-n \text{ before } b}(t) + \text{Prob}_{\gamma-b \text{ before } n}(t) = P \cdot E \cdot (\lambda + R_2)e^{-(\lambda+R_2)t}. \quad (4.5)$$

Lastly, the *False-False* event pairs and the *False-True* event pairs, as stated before, follow a Poisson process and their time difference distributions reflect that of an exponential, with a constant sensitive to only the detector event rate. The combination of the last two categories can be written as:

$$\begin{aligned} \text{Prob}_{b-b}(t) + \text{Prob}_{b-n}(t) &= (1 - P) \cdot (1 - E) \cdot R_2 e^{-R_2 t} + (1 - P) \cdot E \cdot R_2 e^{-R_2 t} \\ &= (1 - P) \cdot R_2 e^{-R_2 t}. \end{aligned} \quad (4.6)$$

When combined with the first sub-scenario in the *True-False* event pairs which also have an exponential term with a constant of R_2 , the expression becomes:

$$\begin{aligned} \text{Prob}_{\gamma-b \text{ no } n}(t) + \text{Prob}_{b-x}(t) &= P \cdot (1 - E) \cdot R_2 e^{-R_2 t} + (1 - P) \cdot R_2 e^{-R_2 t} \\ &= (1 - P \cdot E) \cdot R_2 e^{-R_2 t}, \end{aligned} \quad (4.7)$$

where x can be either a background event or a neutron. Summing up all expressions for the four categories, we derive Eqn. 4.1 as the final fit function for the time difference histogram.

4.1.2 Validation of the Fit Function with a Toy MC Model

Eqn. 4.1 is validated with a toy Monte Carlo Model where pseudo-events are generated to simulate the case of an active detector. Two types of events are produced: background events that are uniformly distributed in time, according to the detector event rate; and source events for which the time difference distribution follows an exponential decay (however, only a fraction of neutrons are generated since some of those do not trigger the detector). These two types of events are generated independently following their own time profile, and then sorted in time sequence to form a time series. Each event is tagged with a timestamp and one of the three event identifiers (background, 4.4 MeV γ , and neutron). In addition, as a simpler emulation of the minimum prompt nhits requirement, each event is also tagged with a boolean value to indicate whether or not it passes the prompt candidate selection criteria.

Fig. 4.1 shows an example plot of the different components in the time difference histogram in the logarithm scale. Three significant components can be seen whereas the *False-True* event pairs only contribute to a sub-percent effect. Both *True-True* event pairs (green line) and *False-False* event pairs (red line) follow a single exponential. As expected, their exponential constants, which are shown as the slopes at which the lines decrease, are different by more than an order of magnitude, thanks to the low background levels in SNO+. While traditional analyses rely on various cuts to screen off most backgrounds in order for the exponential to regress to a linear approximation, Fig. 4.1 provides a compelling proof that a good fit can be sensitive enough to distinguish the two slopes thus making possible the statistical separation using a global fitting algorithm.

As illustrated in Section 4.1.1, the *True-False* event pairs are a combination of two

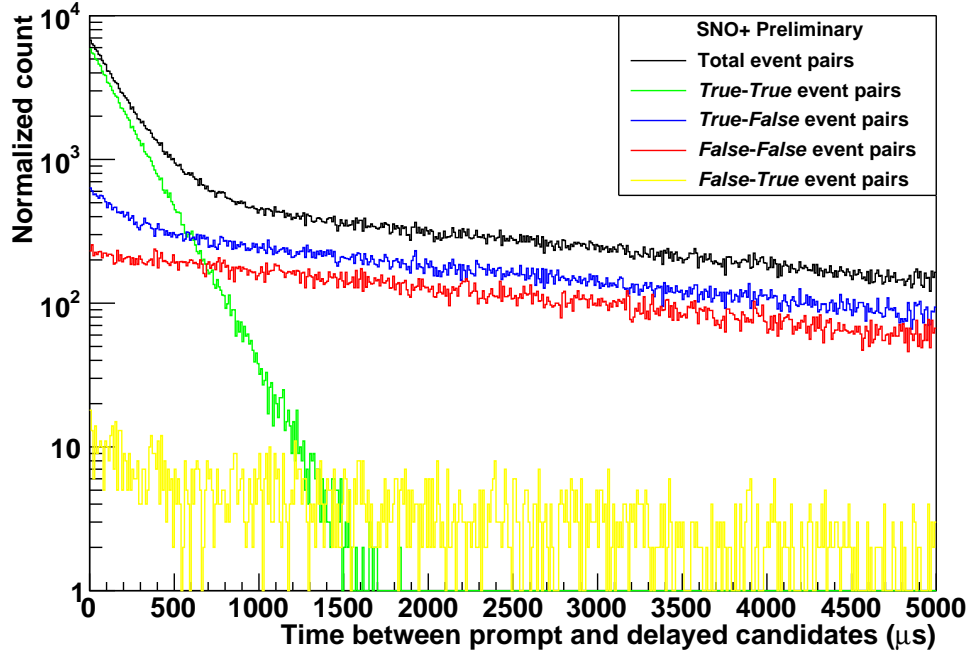


Figure 4.1: Time difference histogram constructed from a toy MC model, where a set of realistic parameters are configured: $E = 50\%$, $P = 90\%$, $\lambda^{-1} = 208.2 \mu\text{s}$, and $R_2 = 360 \text{ Hz}$. The normalization is done in arbitrary unit. Different components of the histogram (shown in different colors) exhibit different patterns as explained in Section 4.1.1.

exponentials with different constants. Fig. 4.2 examines its decomposition. The blue curve, showing the distribution of the *True-False* event pairs, is first compared to a normalized distribution of the *False-False* event pairs, in red. The normalization is done in the way that the latter distribution matches the proportion of the blue curve between $2000 \mu\text{s}$ and $5000 \mu\text{s}$. Within statistical uncertainties, it can be concluded that the two distributions are identical from $\sim 800 \mu\text{s}$, where one expects almost no source event left. A distribution (darker blue) is derived by subtracting the red curve from the blue one, indicating a second component of the *True-False* event pair

distribution. This distribution can be compared against a scaled distribution of the *True-True* event pairs, again identical within statistical variation. This suggests that the second component has the same exponential constant as the *True-True* event pairs, as dictated by the fit function. The exact ratio between the two components is subject to the product of P and E .

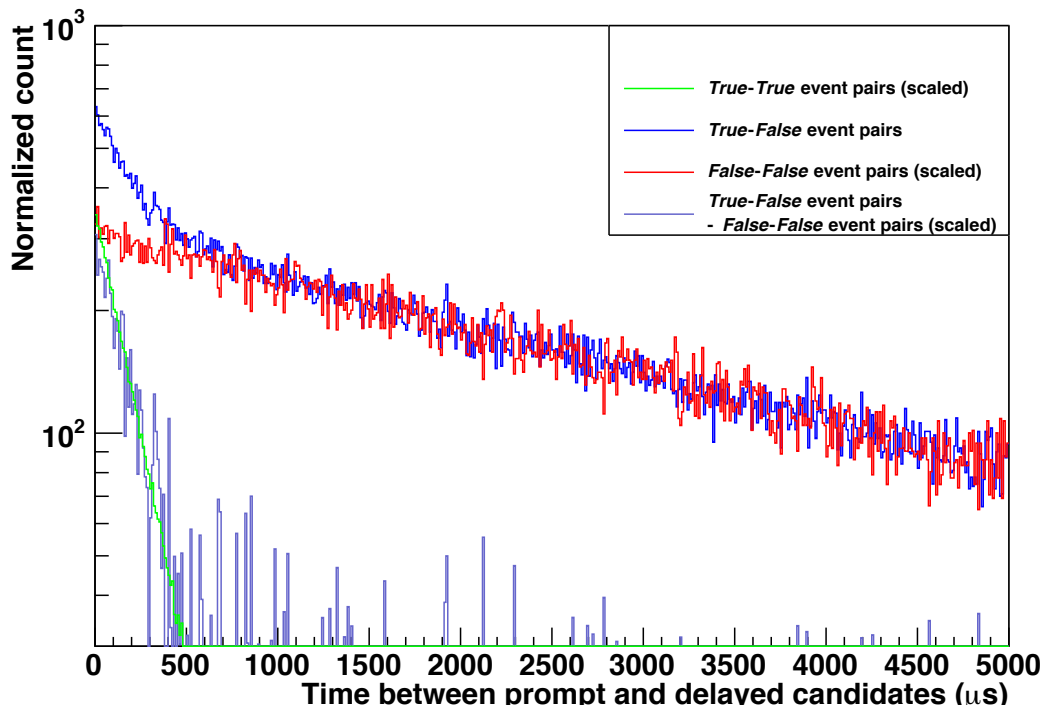


Figure 4.2: Decomposition of the time difference distribution of the *True-True* event pairs. Two exponential components with different constant can be identified: One slower component that reflects the underlying background rate, and the second which is additionally sensitive to the neutron capture constant λ .

Besides the illustration of the fit function, the toy Monte Carlo model is also used to quantitatively evaluate part of the systematic effects in the $^{241}\text{Am}^9\text{Be}$ analysis, especially those that are inherited from the fit function. These come from the secondary

effects that are neglected in deriving the fit function, as well as the assumption that the detector event rate is constant. Further discussion can be found in Section 4.4.1.

4.2 Application to a One-hour Central $^{241}\text{Am}^9\text{Be}$ Calibration Data

4.2.1 The Fit Result

The results of an application of the fit function on a one-hour central $^{241}\text{Am}^9\text{Be}$ run is discussed here. The calibration data is processed with only the SNO+ standard trigger word and data cleaning mask (a small adjustment was made to the burst livetime cut [72] which has only a minimal livetime effect). No reconstruction is needed as the only selection criterion for the candidate pairs is the nhits of events. The results were shown at Neutrino 2018.

Fig. 4.3 shows the fitted time difference histogram for the central run 109134. With nhits thresholds of 17 for the prompt candidate and 7 for the delayed candidate, the neutron capture time constant τ is measured to be:

$$\tau = \lambda^{-1} = 208.2 \pm 2.1 \mu\text{s}, \quad (4.8)$$

where the 2.1 μs denotes the statistical uncertainty from the fit.

Another important direct observable, the product of P and E , is determined by the fit to be 40.6%. This product does not automatically translate itself to the neutron detection efficiency E , which is of more physics interest. Nonetheless, since P has an upper limit of 1 (the purity can not exceed 100% in any circumstance), the fit results allow a lower bound to be set on E . With this particular set of nhits thresholds and

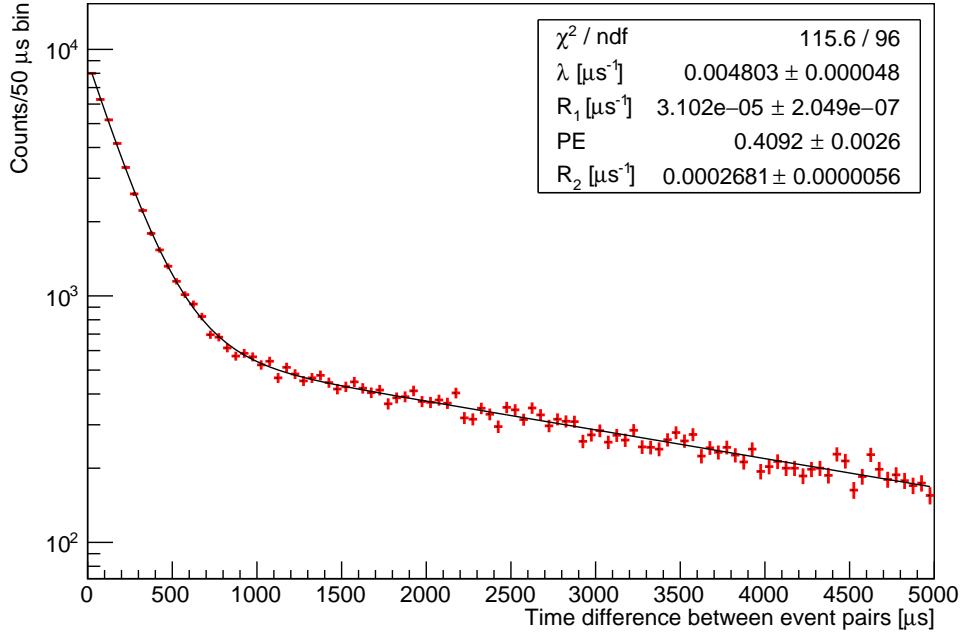


Figure 4.3: Fit results of a one-hour $^{241}\text{Am}^9\text{Be}$ run with the source placed at the center of the detector. The time difference histogram is obtained by placing prompt and delayed nhits cuts of 17 and 7, respectively. Fitted parameters of particular physics interest include the product of P and E , and the neutron capture constant λ , or $\frac{1}{\tau}$. Note that the fitted capture time constant value is different from what is given in Eqn. 4.9 because the latter is averaged for the three hours of data taken in the center of the detector.

dataset, we have:

$$E \geq 40.6\%. \tag{4.9}$$

It will be shown in the following section that as the prompt candidate nhits cut increases, the purity of this selection grows swiftly to be very close to 1.

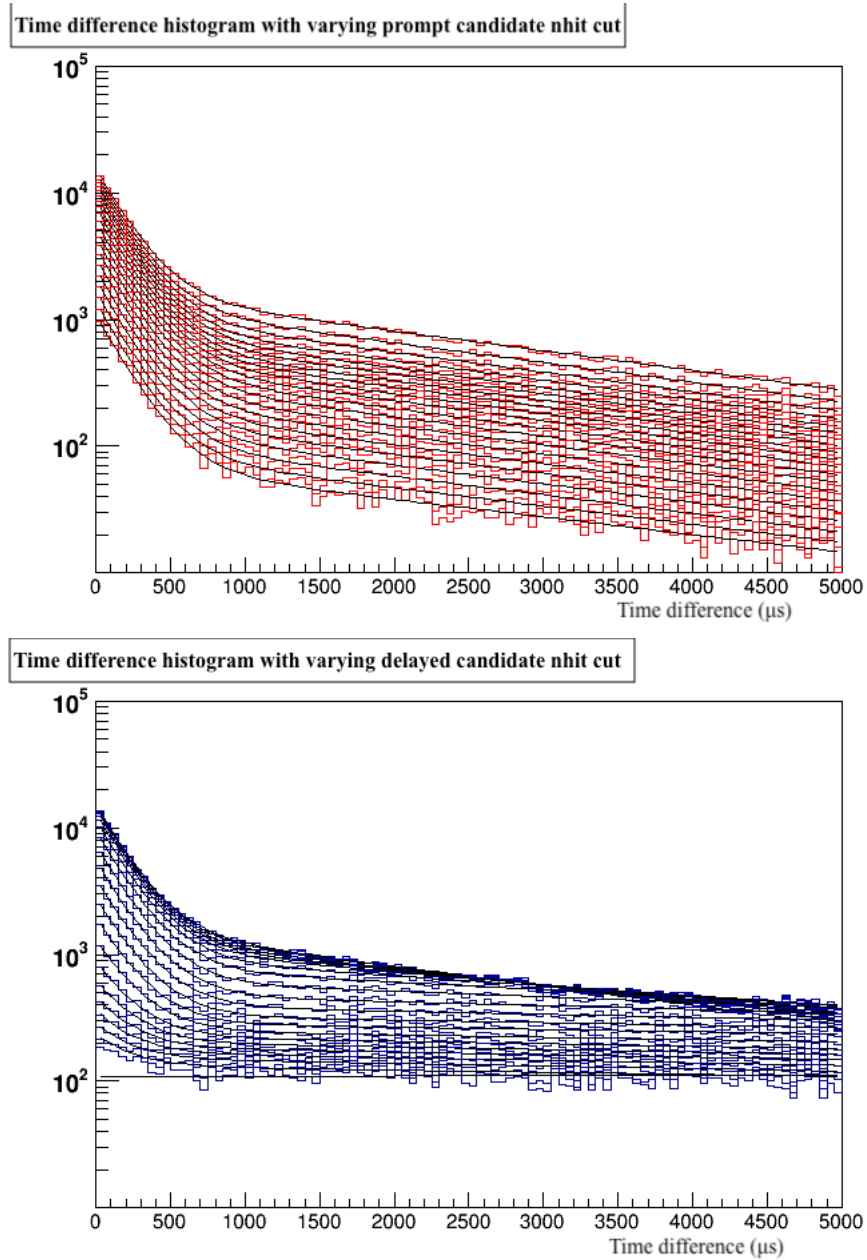


Figure 4.4: Top: fitted time difference histograms with varying prompt candidate nhits cut from 15 to 33 (the delayed candidate nhits cut is fixed to 4). Bottom: fitted time difference histograms with varying delayed candidate nhits cut from 4 to 22 (the prompt candidate nhits cut is fixed to 15).

4.2.2 Varying the Nhits Cuts for Prompt and Delayed Candidates

Further studies of the prompt and delayed candidate nhits cuts prove to be beneficial in understanding special features in the fit parameters. For the one-hour central run, the prompt candidate nhits cut is varied from 15 to 33 and the delayed candidate nhits cut from 4 to 22. Fig. 4.4 overlays all the fitted histograms for different nhits cuts.

Lower fit curves in Fig. 4.4 correspond to higher prompt or delayed candidate nhits cuts, since raising the threshold reduces the total number of events. The prompt candidate nhits cut has little to no effect on the slower exponential component, while the increase of the delayed candidate nhits cut flattens its slope, to a point where with the highest nhits cut the background rate is effectively zero. In fact, traditional $^{241}\text{Am}^9\text{Be}$ analyses expect a similar time difference histogram with a flat secondary “exponential” component. Fig. 4.4 demonstrates that the novel method described in this chapter can be in fact viewed as a generalized case of the traditional analyses.

Fig. 4.5 additionally shows the evolution of the fitted parameters as the prompt and delayed candidate nhits threshold increases. The increase of prompt (delayed) candidate nhits cut decreases the prompt (delayed) event rate. While it is a fairly smooth curve for the prompt event rate, the background rate plateaus after around 14 nhits. This can be explained by the fact that most low energy backgrounds and the neutron signals are excluded from the data at such a high nhits threshold.

The changes in $P \cdot E$ as a function of the nhits cuts shed more light on the understanding of the product. For the left side plot, the product grows as the prompt candidate nhits cut increases, until around 22 nhits. This is due to the fact that as the prompt nhits cut is lifted, E stays the same and P increases. As shown in Fig. 4.6, few

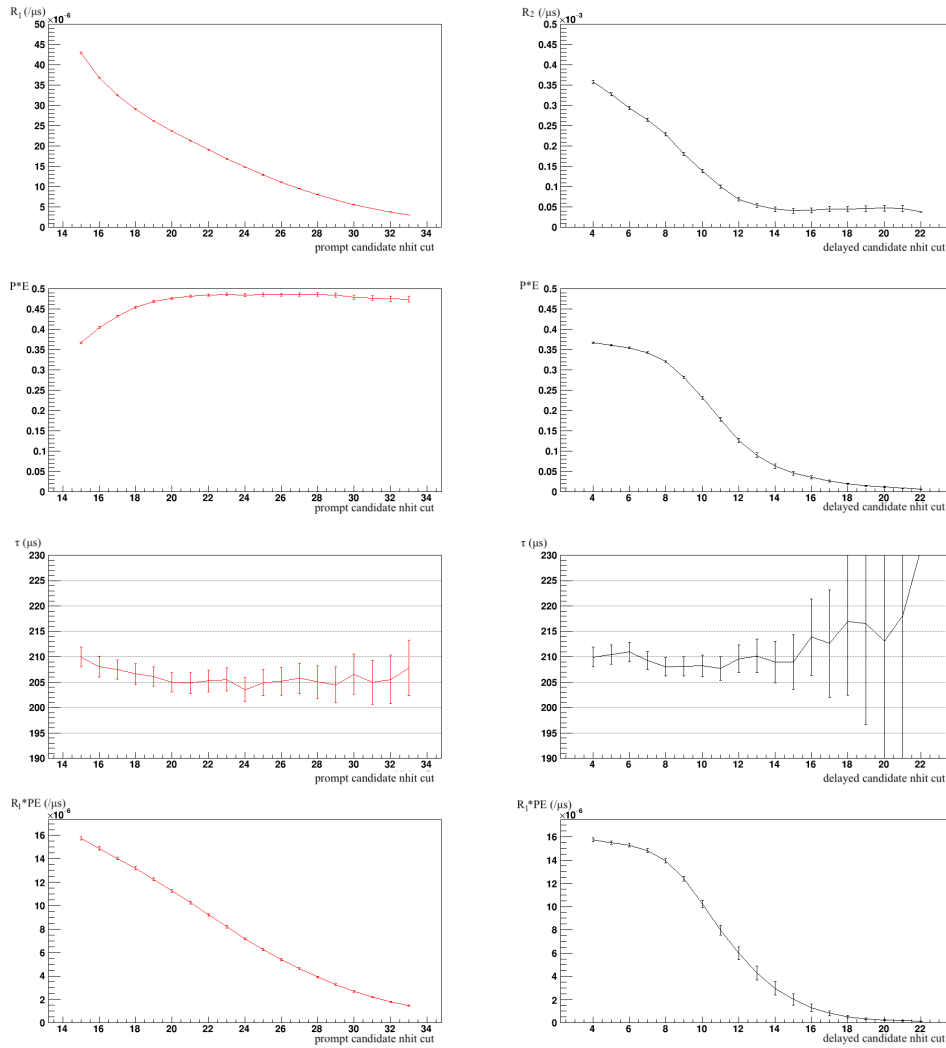


Figure 4.5: Change of important fit parameters as a function of the prompt (delayed) candidate nhits threshold. From top to bottom, plotted are the fitted event rate (R_1 or R_2), $P \cdot E$, capture time constant τ , and the signal rate $R_1 \cdot PE$.

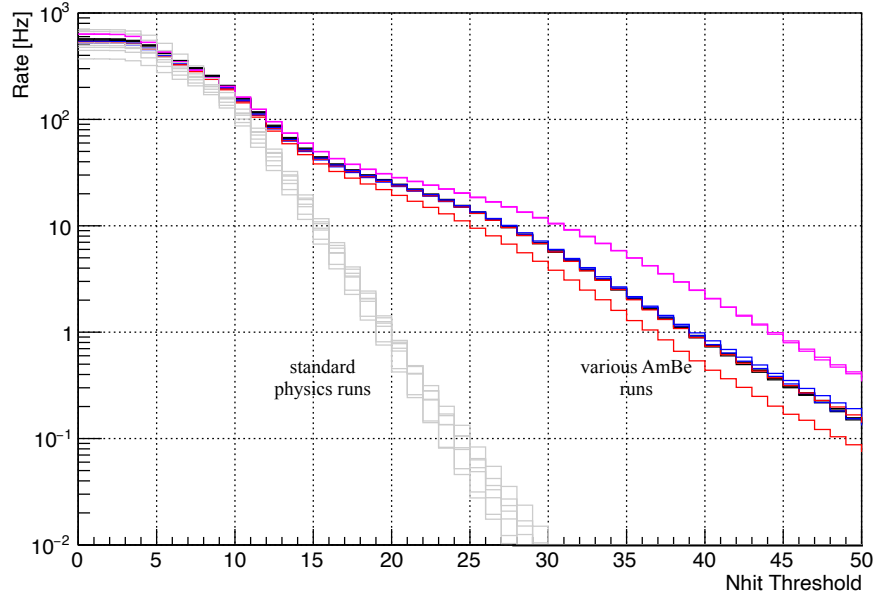


Figure 4.6: The event rate distribution as a function of the nhits threshold. For standard physics runs the event rate decreases more rapidly as there are few events above 20 nhits.

background events have an nhits above 22, where P is calculated to be 1 within 0.1% uncertainties. On the other hand, the plot on the right shows a steady decrease of $P \cdot E$ as the delayed candidate nhits threshold moves up, an expected trend since the neutron detection efficiency E falls as the threshold rises. Using a prompt (delayed) candidate nhits threshold of 22 (4), we measured the neutron detection efficiency at the center of the detector to be:

$$E = 48.4\% \pm 0.3\%, \quad (4.10)$$

where the uncertainty is statistical only.

The third row of Fig. 4.5 shows the evolution of the neutron capture time constant τ . Note the due to the extreme small size of the data with high delayed candidate

nhits cut, the statistical uncertainties on the fit parameter becomes too big to fit in the plot. τ is a physical constant and is not dependent on the nhits thresholds. However, a decreasing trend can be observed at both plots in the low nhits threshold region. The bias with the prompt candidate nhits cut goes away as the purity of the prompt selection increases to close to 1. The deflection caused by the delayed candidate nhits cut, on the order of $\sim 2 \mu\text{s}$, can be attributed to a source of systematic uncertainty related to the fit function which will be discussed in Section 4.4.1.

The signal rate, defined as $R_1 \cdot P \cdot E$, denotes the event rate of true 4.4 MeV γ s that are followed by detectable associated neutrons. It is, in fact, the rate of the detectable γ -n coincidences. As shown in Fig. 4.5, the signal rate drops consistently as the prompt (delayed) candidate nhits cut increases. The difference between consecutive data points is actually the signal rate of a specific nhits. Therefore, the nhits distributions for both the 4.4 MeV γ s and the neutrons can be calculated, shown in Fig. 4.7. Note that the cutoffs at both sides of the 4.4 MeV γ s (15 and 33) and the 2.2 MeV γ s (4 to 22) are not physical bounds. Instead, they represent the nhits range preset in the analysis.

4.3 Application to the Global Dataset

The same analysis method is applied to all the internal $^{241}\text{Am}^9\text{Be}$ calibration data (see Table 3.1), with source positions ranging from the detector center up to 5.5 m away. Because the background rate can be different in each run, the fit is performed separately after which the results are combined to reduce the statistical uncertainties. Two observables are of particular physics interests: neutron capture time constant τ (or the neutron capture constant λ), with which the cross-section of neutron capturing

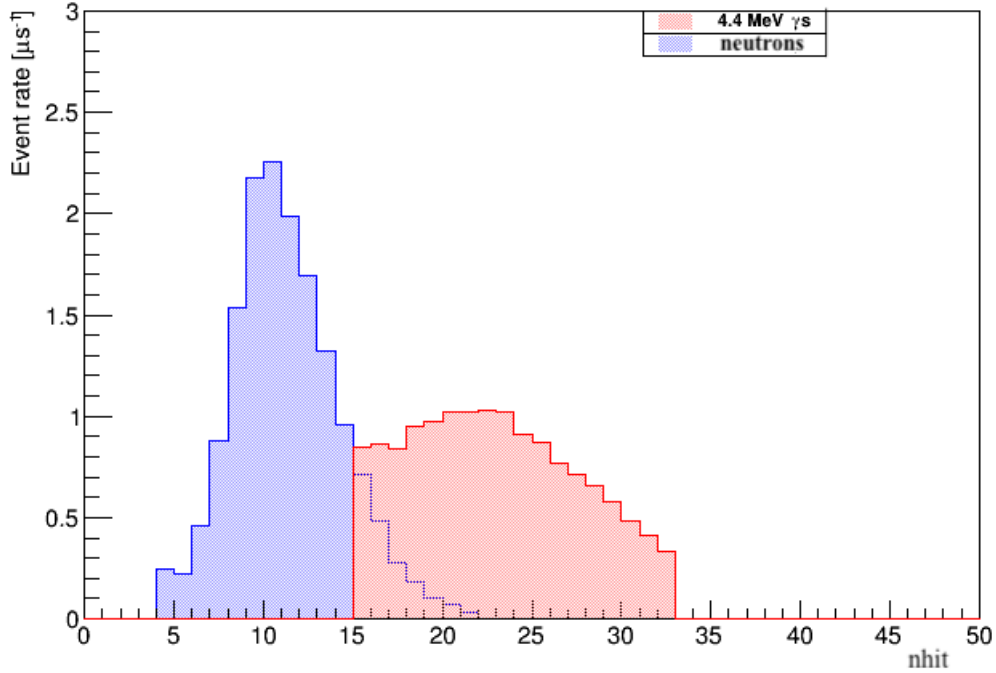


Figure 4.7: Nhits distributions for the neutrons and the 4.4 MeV γ s. These distributions are derived from calculating the difference between consecutive data points of the signal rate distribution in Fig. 4.5.

on proton can be inferred; and the neutron detection efficiency E , which is very sensitive to the detector trigger threshold and is vital in detecting antineutrinos in SNO+ or SNO+-like water Cherenkov detectors. τ is a direct parameter to be fitted whereas E can be calculated from the product $P \cdot E$ using data samples that are selected with relatively high prompt candidate nhits cut.

4.3.1 The Neutron Capture Time Constant τ

A set of prompt and delayed candidate nhit threshold of (18, 5) is determined to render the best precision for the measurement of the neutron capture time constant

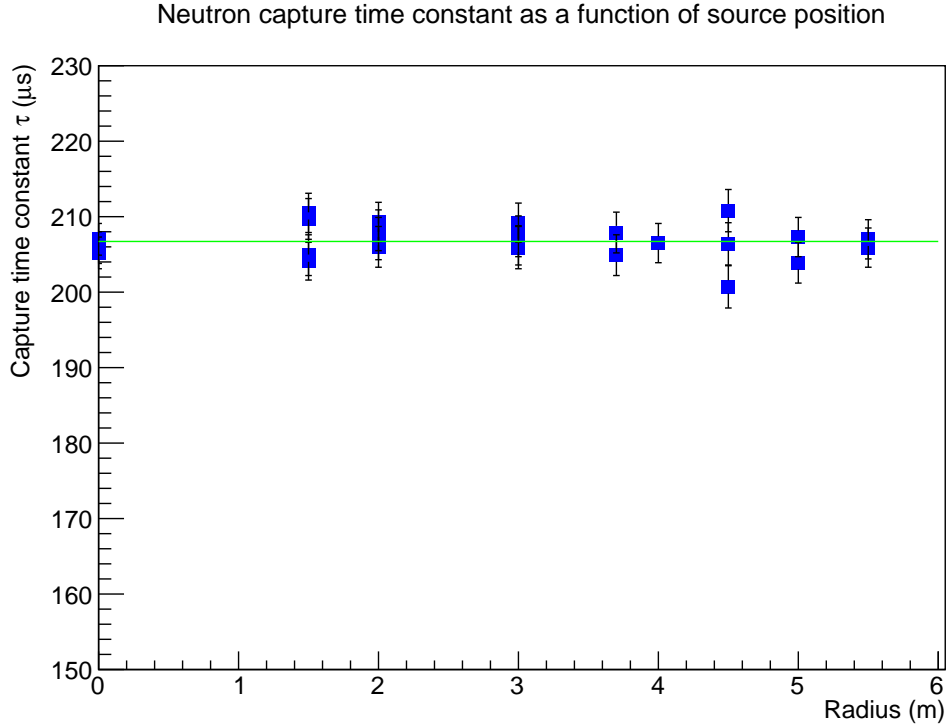


Figure 4.8: The fitted neutron capture time constant τ as a function of the radial source position. The weighted average is shown in the green line.

τ (see Section 4.4.1). Fig. 4.8 shows the distribution of the neutron capture time constant τ as a function of the radial source positions. The results from individual runs have a similar statistical uncertainty of $\sim 2.5 \mu\text{s}$ and are consistent with each other. The weighted average is:

$$\tau = \frac{1}{\lambda} = 207.03 \pm 0.42 \mu\text{s}, \quad (4.11)$$

where the uncertainty is statistical only.

4.3.2 The Neutron Detection Efficiency

An accurate measurement of E is obtained by increasing the prompt candidate nhits threshold. As shown in Fig. 4.6, an nhits threshold of 25 guarantees that $(1 - P) < 0.001$. Additionally, the results are compared with those obtained with a threshold of 22 or 30 nhits and confirmed to be consistent. The delayed candidate nhits cut is set to be 4 to obtain the highest neutron detection efficiency. Moreover, in order to increase the stability of the fit, the neutron capture time constant τ is fixed to the value given in Eqn. 4.11. The associated uncertainty is propagated by fixing τ to different values in accordance with its statistical uncertainty, and evaluated to be negligible.

Fig. 4.9 shows the neutron detection efficiency as a function of the radial source position. The combined efficiency at the center of the detector is calculated to be $(48.3 \pm 0.2)\%$. In general, E has a fairly flat distribution inside the detector, maintaining a value of around 48.3%. A significant drop in the efficiency is observed for positive z positions, where it lacks the PMT coverage because of the AV neck. More studies on the position dependence of the neutron detection efficiency using Monte Carlo simulations can be found in Section 5.3.

4.4 Systematic Considerations

Multiple sources of systematic effects that could have an impact on either the neutron capture time constant τ or the neutron detection efficiency E have been identified and closely examined. These include the secondary effects that are oversimplified and some ideal assumption made when deriving the fit function, the data cleaning sacrifice, the initial neutron energy spectrum, the encapsulation effects, and the temperature

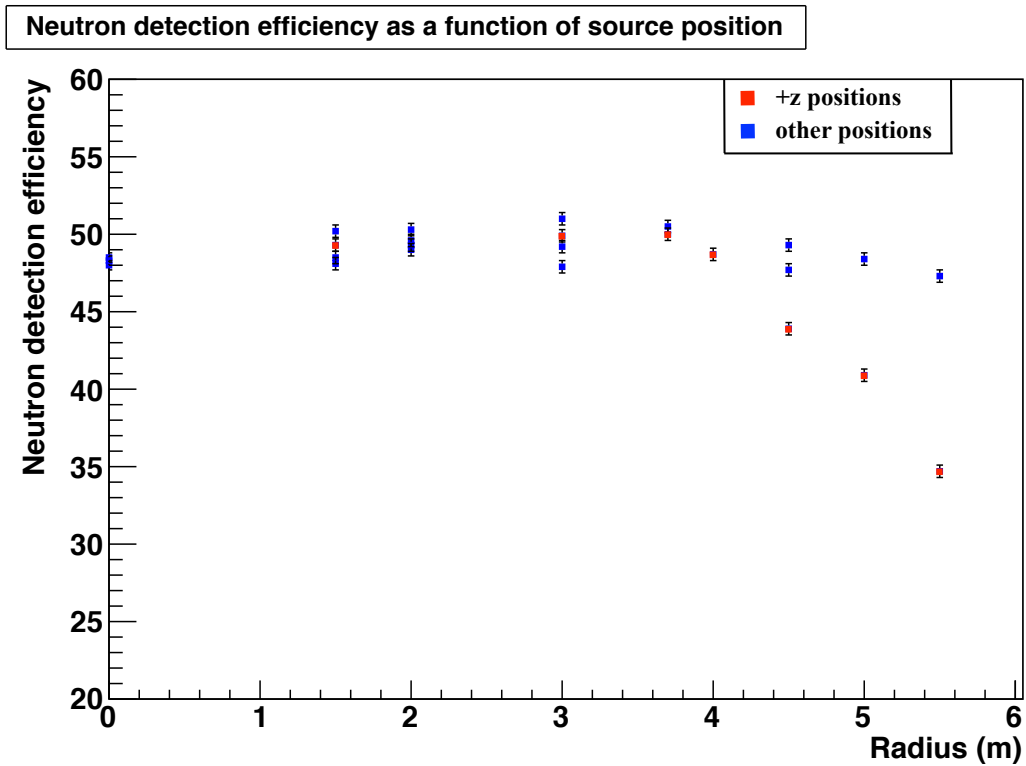


Figure 4.9: The neutron detection efficiency E as a function of the radial source position. Data points in red are collected from positive z positions and their drop towards higher radius is due to the absence of PMT coverage close to the AV neck.

variations.

In the following subsections, details on the evaluation of each systematic effect are presented.

4.4.1 Systematics From the Fit Function

One of the most significant systematic corrections for τ and E comes from the incompleteness of the fit function. To start with, Eqn. 4.1 neglects several secondary effects such as the scenario where multiple background events get in between the 4.4 MeV γ s and the neutron. The absence of other exponentials with even slower time

constant would result in an intrinsic positive bias on the capture time constant τ . Furthermore, Eqn. 4.1 fails to take into account the fluctuation in the detector event rate but instead simply assumes it to be constant. The correction for this effect is dependent on the size of the fluctuation, which in turn depends on the delayed candidate nhits cut. These effects are evaluated with the toy Monte Carlo model described in Sec. 4.1.2.

The systematic due to the secondary effects is evaluated by comparing the true neutron capture time constant τ_{true} preconfigured in the toy Monte Carlo and the fitted time constant τ_{fit} . The difference between τ_{true} and τ_{fit} , using a realistic set of parameters, is calculated to be $\sim 0.2 \mu s$.

The second systematic arising from the fit comes from the fact that the detector rate does not oscillate around a single mean value. As shown in Fig. 4.10, a measurement of the detector rate in 1-second periods within a run fails to follow a Gaussian distribution, but instead can be well described by an empirical one-dimensional Maxwell-like distribution:

$$F(x) = A(x - \mu)e^{-\frac{(x-\mu)^2}{\sigma}}, \quad (4.12)$$

where μ and σ are the equivalent mean and spread of the Gaussian distribution. Fig. 4.11 shows the distribution of fit parameters μ and σ for all internal runs. These two parameters were found to have no correlation with the source position.

A correction to the fitted neutron capture time constant is derived by sampling a detector event rate from the Maxwell-like distribution with μ and σ set to the medians of the 25 internal runs (Table 4.1). The correction is calculated as the difference between the true MC value and the fitted value. Note that by doing so

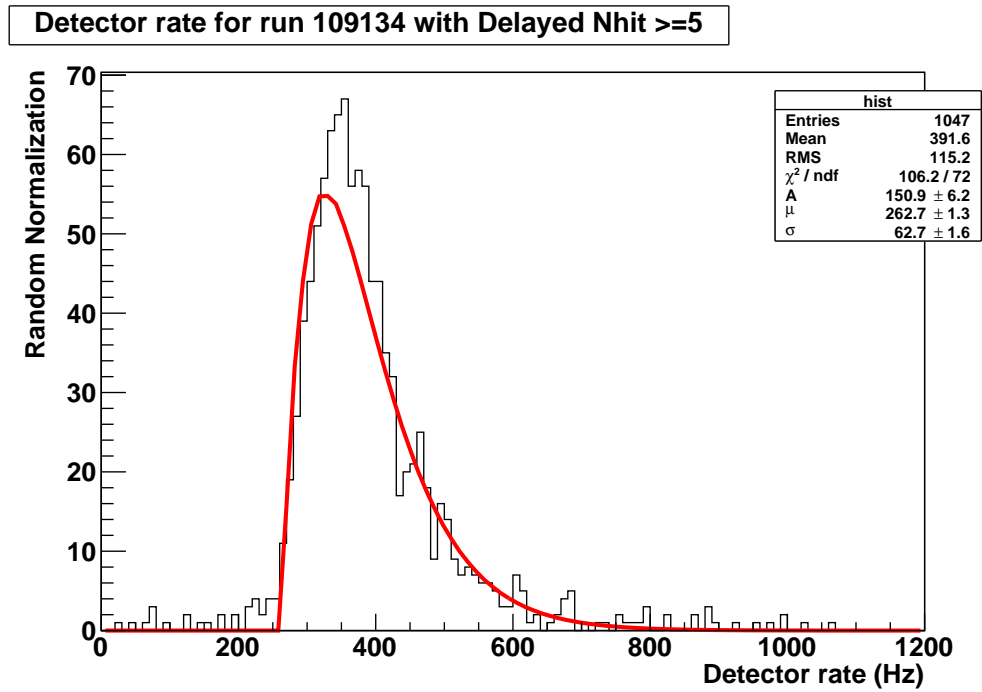


Figure 4.10: Detector event rate of run 109134 fitted with a Maxwell-like distribution.

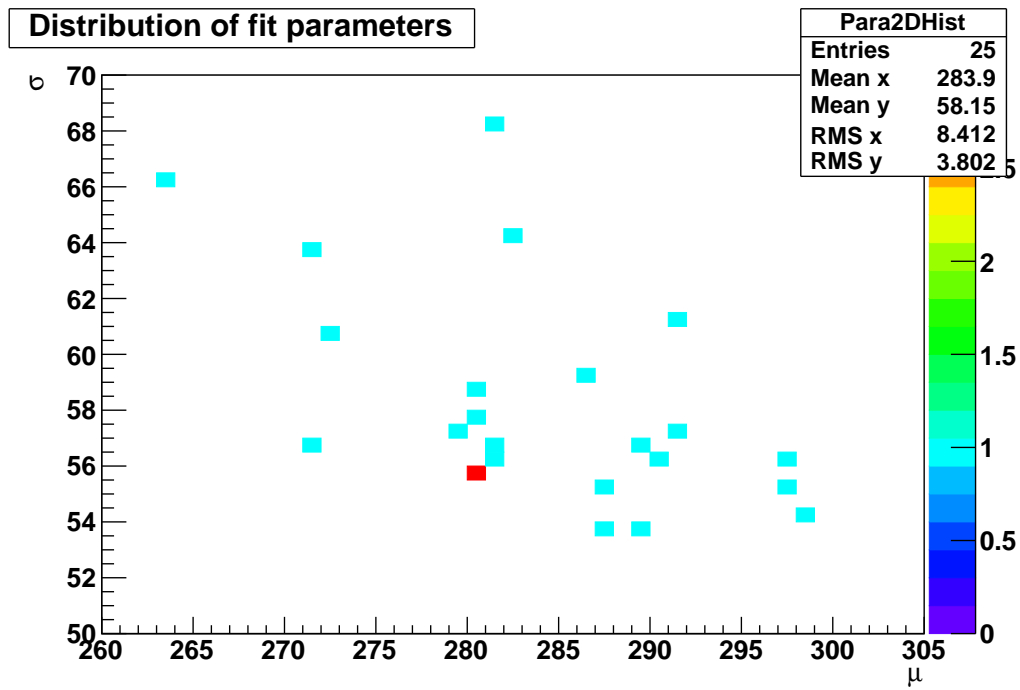


Figure 4.11: Distribution of the fit parameters for all internal AmBe runs.

the first systematic is automatically included in the calculation. To reduce the effect of statistical fluctuations for the fitted value, the toy MC datasets are generated 100 times, and the χ^2 minimum is calculated to be the final fitted value¹. Fig. 4.12 shows a distribution of fitted capture times for a specific pair of rate parameters.

Table 4.1 also shows the calculation of the uncertainty to this systematic correction. Different combinations of the upper and lower RMS values of μ and λ are used to generate the toy Monte Carlo datasets and calculate again the corrections. The difference between the two most extreme values is set to be the uncertainty for this systematic correction.

μ	σ	fitted time [μ s]	true time [μ s]	comment
283.9	58.51	210.00	208.20	median μ , median σ
292.3	61.95	210.25	208.20	upper RMS μ , upper RMS σ
292.3	54.35	209.77	208.20	upper RMS μ , lower RMS σ
275.5	61.95	210.10	208.20	lower RMS μ , upper RMS σ
275.5	54.35	209.88	208.20	lower RMS μ , lower RMS σ

Table 4.1: The fitted capture time constant and true value for the median and upper & lower RMS values of event rate parameters μ and σ .

To validate the correction, this systematic effect was evaluated as a function of the delayed event nhits threshold. Fig. 4.13 shows the fitted capture times as output by the analysis in Section 4.3 and also after they were corrected. The important observations are (1) that the two curves converge as the threshold is increased, indicating that the Maxwell-like distribution becomes more symmetric, which is directly confirmed with the data (see Fig. 4.14), and (2) the curve after correction is flat, indicating the correction is calculated correctly at all thresholds.

This systematic is calculated specifically for the analysis of Section 4.3.1 and 4.3.2,

¹The χ^2 minimum was found to be the same as the arithmetic average.

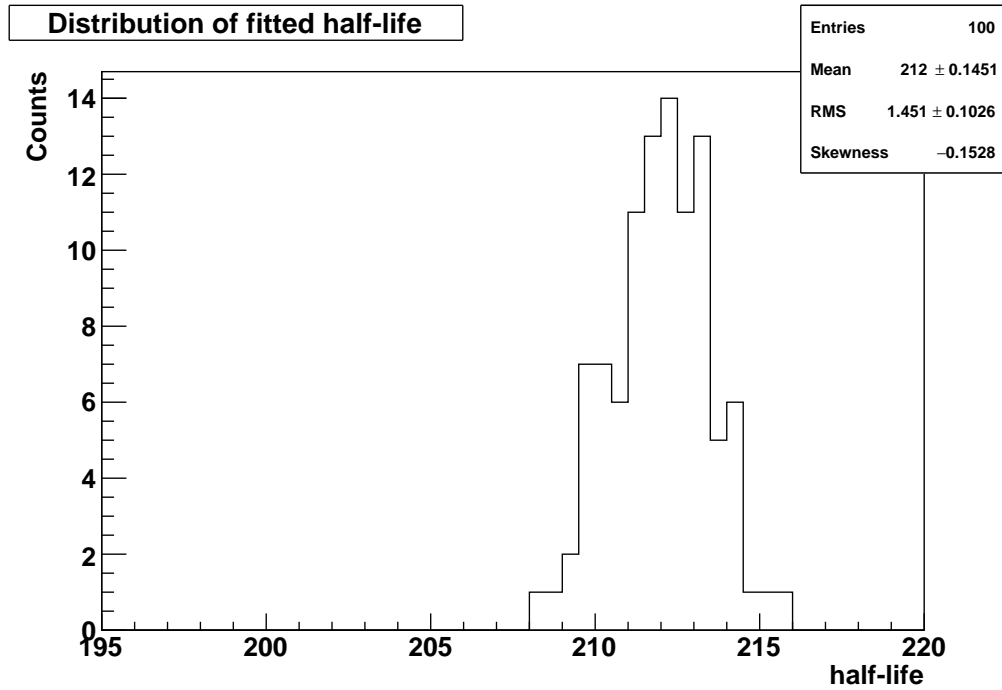


Figure 4.12: Example distribution of fitted capture time for a given set of event rate variation parameters.

which uses a delayed event threshold of 5 nhits when determining τ and 4 nhits when calculating the efficiency. Indeed, Fig. 4.13 motivated the threshold of 5 for τ : a threshold of 4 would increase the statistics slightly, however, the correction calculated at 4 appears inconsistent with the correction at all other values.

The systematic correction is calculated for all AV-internal runs to be $-1.80 \mu\text{s}$ and a systematic uncertainty of ${}_{-0.25}^{+0.23} \mu\text{s}$ is taken from Table 4.1. Expressed relatively, this is $(-0.86_{-0.12}^{+0.11})\%$. Similarly, the effect on the detection efficiency is obtained for only the three central runs to be $(0.21 \pm 0.29)\%$.

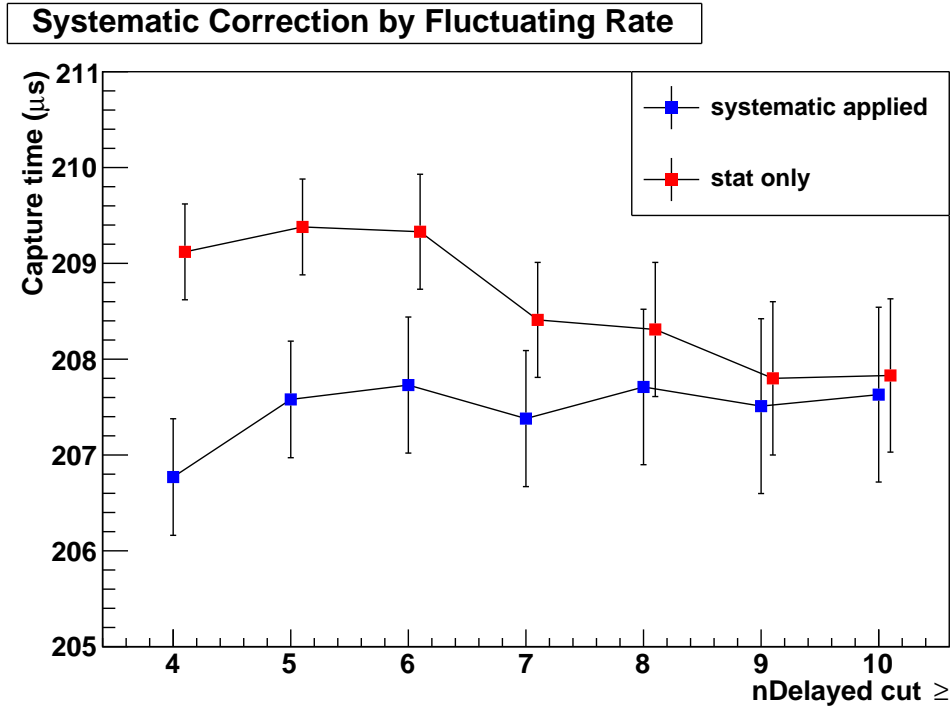


Figure 4.13: Fitted capture time constant as a function of delayed event nhits threshold, before (red) and after (blue) the correction for the fluctuating rate systematic. The prompt candidate nhits threshold is 15 nhits.

4.4.2 Data Cleaning Sacrifice

Data cleaning [73] constitutes a wide range of cuts that are designed to remove events with specific characteristics such as instrumental backgrounds. Instrumental backgrounds are backgrounds that are caused by the detector, such as flashing PMTs or crosstalk events. While removing these backgrounds it is possible that the data cleaning cuts also throw away real physics events or source events in the case of $^{241}\text{Am}^9\text{Be}$ calibration runs. This proportion of the real events that are mistakenly removed from the data is defined as the data cleaning sacrifice.

For the $^{241}\text{Am}^9\text{Be}$ analysis, the data cleaning sacrifice can cause a systematic shift in the neutron detection efficiency, while the neutron capture constant λ is immune

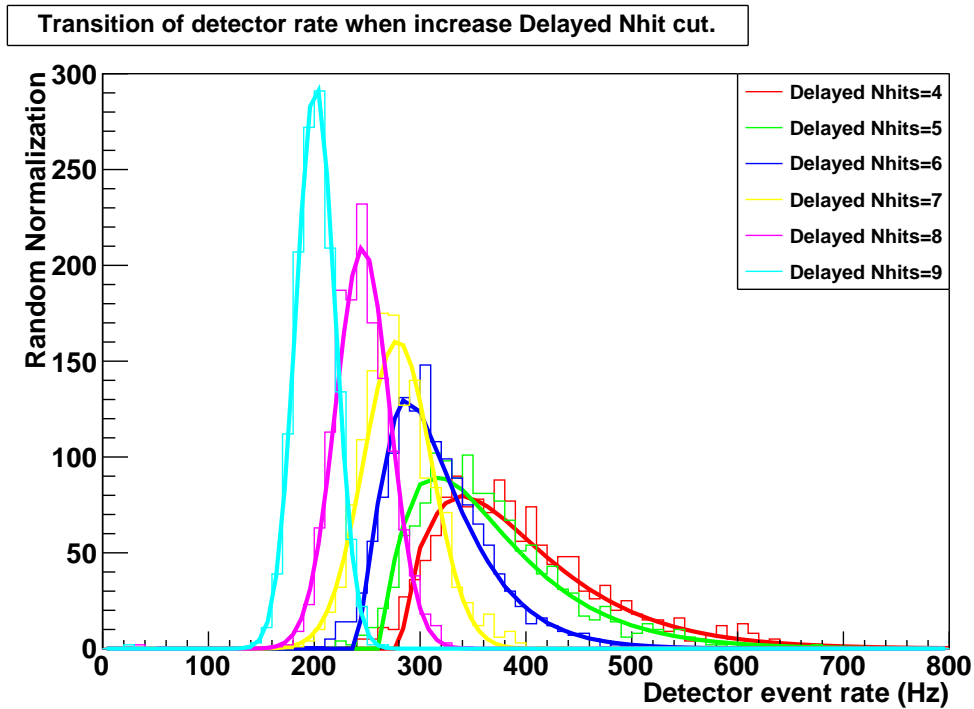


Figure 4.14: Illustration of how the Maxwell-like rate distribution becomes more symmetric with increasing delayed nhits threshold. Note that at 7 nhits and above the distributions were best fitted with a Gaussian, while below 7 nhits the distributions were fitted with the Maxwell-like function, consistent with the jump observed in λ in Fig. 4.13.

to the effect. This section presents an estimate of the fractional sacrifice of $^{241}\text{Am}^9\text{Be}$ events.

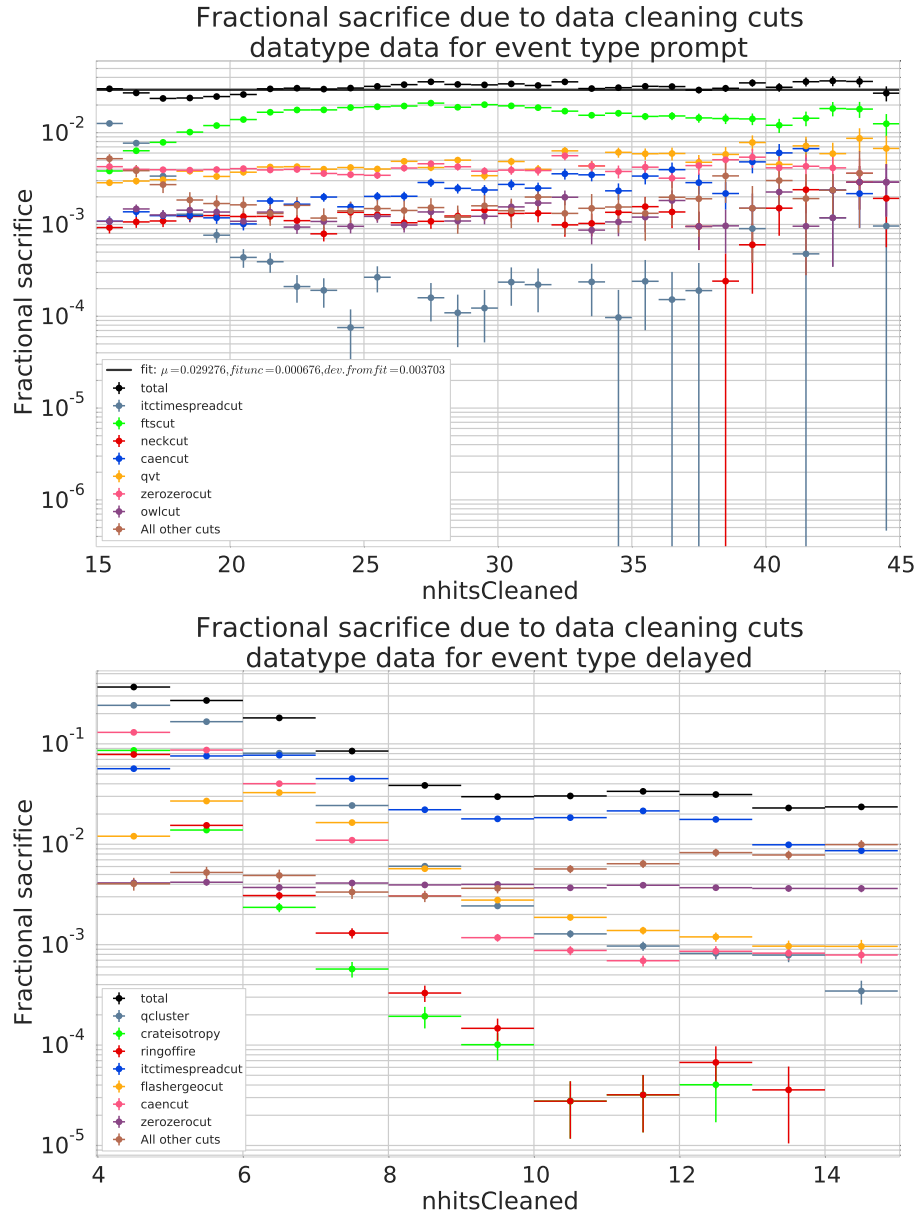


Figure 4.15: Data cleaning sacrifice for prompt and delayed candidate events. Figure is from [74].

The sacrifices are evaluated separately for prompt and delayed candidates and the results are shown in Fig. 4.15. All data cleaning cuts except the livetime cuts are evaluated individually, and then simultaneously to evaluate the total sacrifice.

The `ftscut` (designed to target flashers) dominates the prompt event data cleaning sacrifice, while the `nhits \leq 5` region is dominated by the `qcluster` cut, designed to flag hits that produce noise in neighboring channels. The `itctimespreadcut`, which targets `flatTAC` events, dominates the remaining sacrifice.

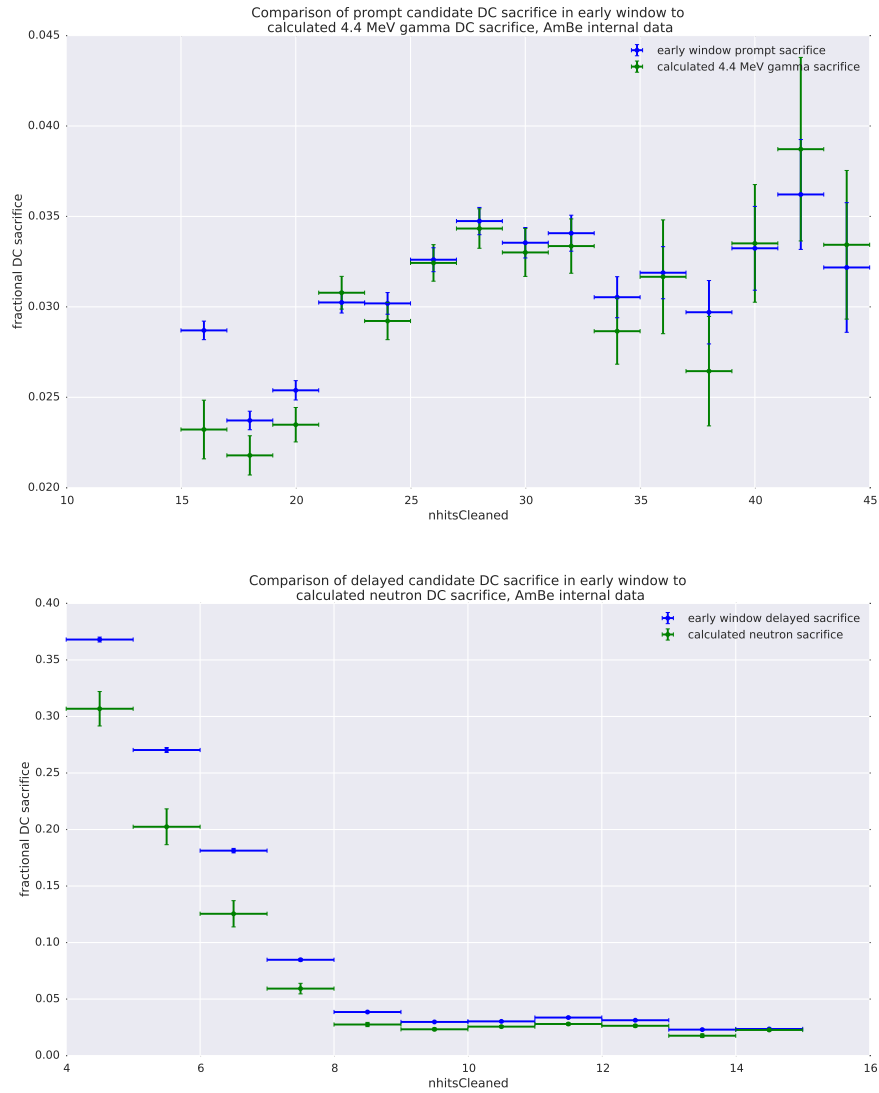


Figure 4.16: Comparison of prompt (top) and delayed (bottom) candidate data cleaning sacrifices to the calculated 4.4-MeV γ and neutron capture data cleaning sacrifices. Figure is from [75].

The calculation of the $^{241}\text{Am}^9\text{Be}$ signal sacrifice (the sacrifice for the *True-True* event pairs) is done in [74] by estimating at the same time both the fraction of *True-True* event pairs and the fraction of instrumental backgrounds in the candidate dataset. Fig. 4.16 shows the comparison of calculated sacrifice between the prompt (delayed) and the 4.4 MeV γ s (neutrons). A sizable shift is visible in the delayed candidate to neutron capture sacrifice comparison, indicating a large presence of instrumentals at lower nhits. On the other hand, the sacrifices of the prompt candidate and the 4.4-MeV γ are mostly consistent within uncertainties, since there is little to no contamination of instrumental backgrounds in the high nhits region.

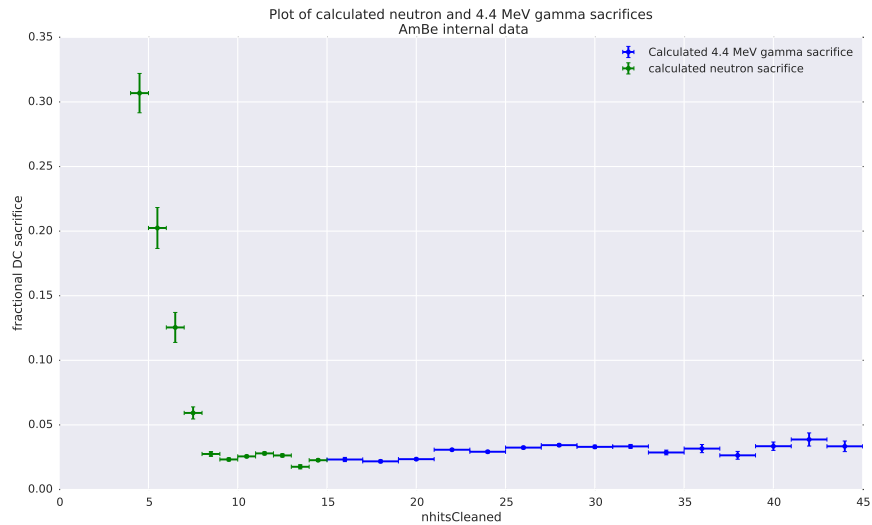


Figure 4.17: Overlay of calculated sacrifices for neutron captures and 4.4-MeV γ 's using internal AmBe data. Figure is from [75].

The calculated sacrifices for the neutron capture and 4.4-MeV γ as a function of nhits are shown in Fig. 4.17. The calculated data cleaning sacrifice is largely flat in the $\text{nhits} > 8$ region. Convoluting this curve with the nhits distributions of the neutron signals (Fig. 4.7) yields a total sacrifice of $(3.89 \pm 0.80)\%$ for the central $^{241}\text{Am}^9\text{Be}$

runs, which can be expressed as an absolute correction and uncertainty of $(1.89 \pm 0.39)\%$ on the neutron detection efficiency at the center of the detector.

4.4.3 Initial Neutron Energy Spectrum

Neutrons from the $^{241}\text{Am}^9\text{Be}$ source are emitted at different energies. The energy spectrum is heavily dependent on the anisotropic neutron distribution and the final state of the residual nuclei. The spectrum currently in RAT was implemented from past SNO simulations [76] and is shown in Fig. 4.18.

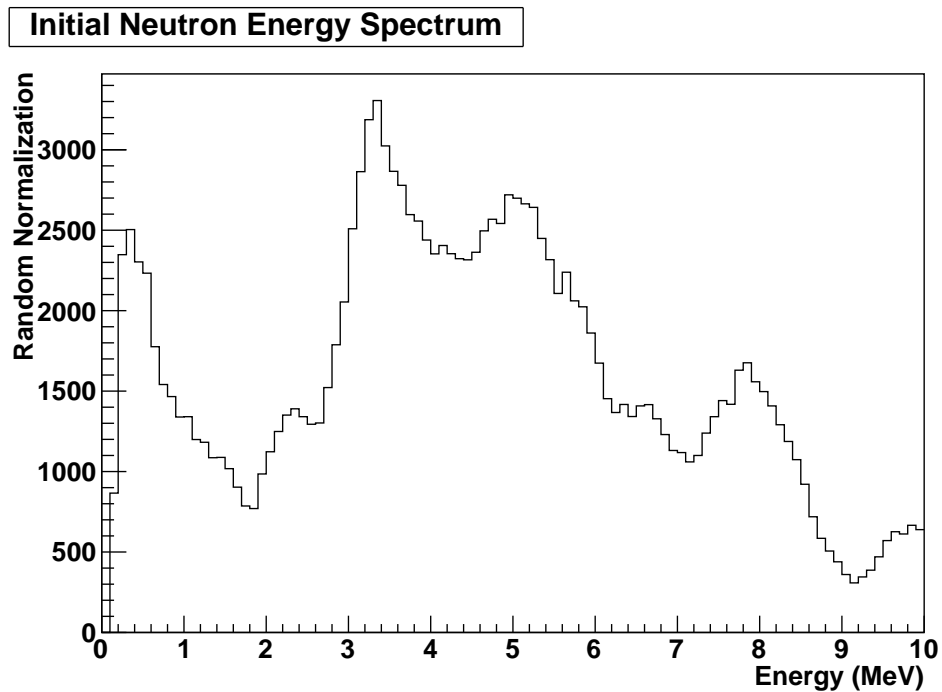


Figure 4.18: Energy spectrum of neutrons emitted from the $^{241}\text{Am}^9\text{Be}$ source in RAT.

The various initial neutron energies could in principle lead to different capture times. This effect is evaluated by comparing simulations of thermal neutrons and $^{241}\text{Am}^9\text{Be}$ neutrons at the center of the detector. The two time difference distributions are shown in Fig. 4.19, where they are fitted with an exponential from $10 \mu\text{s}$ to

1000 μs . The fitted capture time constants τ are indistinguishable, resulting in a $-0.05 \mu\text{s}$ correction with a statistical uncertainty of $\pm 0.19 \mu\text{s}$.

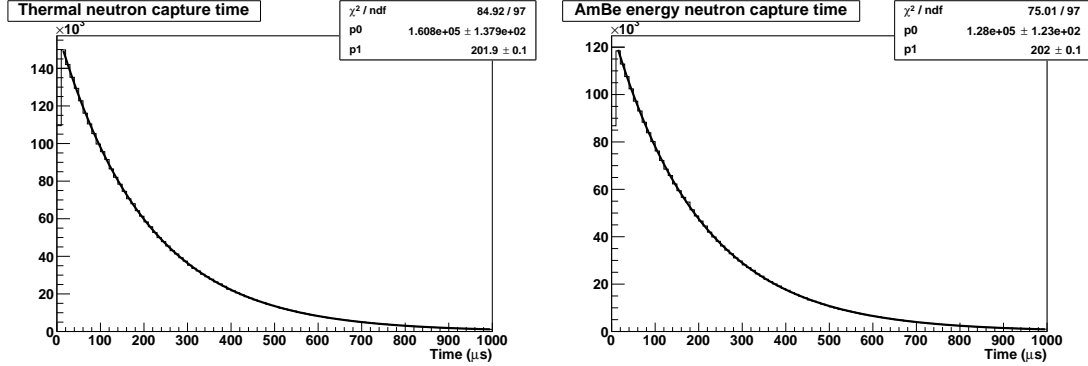


Figure 4.19: The time difference histogramss fitted with an exponential for thermal neutrons (left) and $^{241}\text{Am}^9\text{Be}$ energy neutrons (right).

This was further checked by categorizing $^{241}\text{Am}^9\text{Be}$ simulations into ten bins in the emitted neutron energy, from 0-1 MeV to 9-10 MeV. The time difference histograms were plotted for each energy bin and capture time constants were fitted. The results are shown in Table 4.2, and are consistent with no energy dependence.

The neutron detection efficiency does not depend on the neutron energy, so there is no associated systematic.

E (MeV)	0-1	1-2	2-3	3-4	4-5	5-6	6-7	7-8	8-9	9-10
λ (μs)	201.2	200.6	199.2	202.2	201.6	202.0	201.4	200.0	199.3	202.1
error (μs)	± 1.0	± 1.0	± 1.0	± 1.1	± 1.2	± 1.2				

Table 4.2: Neutron capture time constant for different neutron energy bins.

4.4.4 Source Encapsulation

The source encapsulation described in Section 3.2 poses a few bias effects towards the measurement of E and λ .

To start with, neutrons passing through the encapsulation would have a bigger capture time constant because the proton density of the encapsulation is less than that of water. This effect is evaluated by simulating $^{241}\text{Am}^9\text{Be}$ event with and without encapsulation. As will be discussed in Section 5.1.1, it is achieved by changing the material of the encapsulation from Delrin to water. The fitted neutron capture time constants are given in Table 4.3. Additionally, the uncertainty related to this correction is evaluated by measuring the uncertainty of the volume and density of the encapsulation, which is measured to be $1.405 \pm 0.032 \text{ g/cm}^3$ using water displacement. Simulations are done with the lower and upper bound values for the Delrin density and the results are also included in Table 4.3.

Simulations	τ (μs)	Fit error (μs)	Efficiency	Fit error
Default	204.74	± 0.19	54.62%	$\pm 0.14\%$
No encapsulation	201.89	± 0.22	55.05%	$\pm 0.14\%$
Delrin density=1.37	204.21	± 0.20		
Delrin density=1.44	205.01	± 0.20		

Table 4.3: Fitted neutron capture time constants and selection efficiencies from four different simulations. Efficiencies are excluded from the bottom two rows because their differences are estimated analytically to be smaller than the precision that is practically achievable with the simulation.

From Table 4.3 a correction on the capture time constant is derived by taking the difference between the fit results, yielding $-2.85 \mu\text{s}$. An uncertainty on this correction is estimated to be $^{+0.53}_{-0.27} \mu\text{s}$, or $^{+0.57}_{-0.34} \mu\text{s}$ with the $0.20 \mu\text{s}$ fit errors included. Expressed relatively, this is $^{+0.28\%}_{-0.16\%}$.

Furthermore, as discussed in Section 3.2 and 5.1.1, the encapsulation has a small amount of stainless steel, which is composed of iron, chromium, and nickel, all of which have large neutron cross-sections. The stainless steel is not modeled in the simulation, so a separate study was performed to determine any potential effect.

First, a simulation was performed in which the material of the smallest subvolume (the outer wall, see Section 5.1.1) of the source was changed from Delrin to stainless steel. Events from this simulation were then inserted into the nominal simulation in proportion to the volume of stainless steel present in the source encapsulation (1.04 cm³ out of 60.56 cm³). This provides an estimate of the systematic effect, which is $0.07 \pm 0.30 \mu\text{s}$, or $(0.03 \pm 0.15)\%$.

Finally, summing the corrections and quadratically summing the uncertainties, the correction of capture time with uncertainty is $(-2.78^{+0.70}_{-0.54}) \mu\text{s}$, or $(-1.38^{+0.35}_{-0.27})\%$.

Regarding the neutron detection efficiency, the presence of the source encapsulation results in a $(0.43 \pm 0.20)\%$ correction and uncertainty (from Table 4.3). As such, the contribution from the uncertainty in density is estimated to be on the order of $0.03/1.41 \cdot 0.43\% = 0.01\%$, and therefore negligible. Due to this value being much smaller than the precision of simulations practically achievable, no additional uncertainty is assigned. As the impact of stainless steel is expected to be similar, the final correction and systematic are simply those determined from the presence of the encapsulation.

4.4.5 Temperature Variations

The mean neutron-capture time constant τ is related to neutron velocity v_n and the mean free path of the neutron λ_{mfp} :

$$\frac{1}{\tau} = \frac{v_n}{\lambda_{\text{mfp}}} = v_n n_{\text{H}} \sigma_{\text{H}}(v_n), \quad (4.13)$$

where n_{H} is the number density of hydrogen atoms and σ_{H} is the neutron-hydrogen cross-section. There are two effects on neutron capture time from temperature: (1)

the typical neutron velocity increases with temperature, (2) the density of water increases with decreasing temperature, and therefore, so does the density of hydrogen nuclei n_{H} .

The product of $v_n n_{\text{H}} \sigma_{\text{H}}(v_n)$ is extremely flat as a function of energy below inverse beta decay energies [$O(15)$ keV], therefore little variation is expected in the capture time from effect (1) above². To quantify this, Monte Carlo calculations were performed with the energy-dependent cross-section and a Maxwell–Boltzmann velocity distribution [77]. Fig. 4.20 shows that the product changes by $-0.0022\%/^{\circ}\text{C}$. This estimate is expected to also be valid for the higher energies of $^{241}\text{Am}^9\text{Be}$ neutrons based on the observation that our determination of τ shows no dependence on neutron energy (see Section 4.4.3).

The number density n_{H} varies as the density of water changes with temperature, which is $-0.015\%/^{\circ}\text{C}$ at 15°C [78].

Across the periods of $^{241}\text{Am}^9\text{Be}$ calibration, as well as across the top and bottom of the detector, the detector temperature was measured to be around 15°C and a maximum difference of 2.4°C was observed [79] for both variations. Therefore, the total systematic uncertainty from temperature is estimated to be:

$$\sqrt{[(0.0022\%/^{\circ}\text{C})^2 + (0.015\%/^{\circ}\text{C})^2] \cdot [(2.4^{\circ}\text{C})^2 + (2.4^{\circ}\text{C})^2]} = 0.051\%. \quad (4.14)$$

4.4.6 Summary of Corrections and Uncertainties

Table 4.4 shows the systematic corrections and uncertainties for the two observables of interest; i.e., the thermal neutron capture time constant τ and the neutron detection

²This v^{-1} dependence of the cross-section is also what allows Eq. (4.13) to be expressed equivalently in terms of neutron velocity instead of relative neutron-proton velocity.

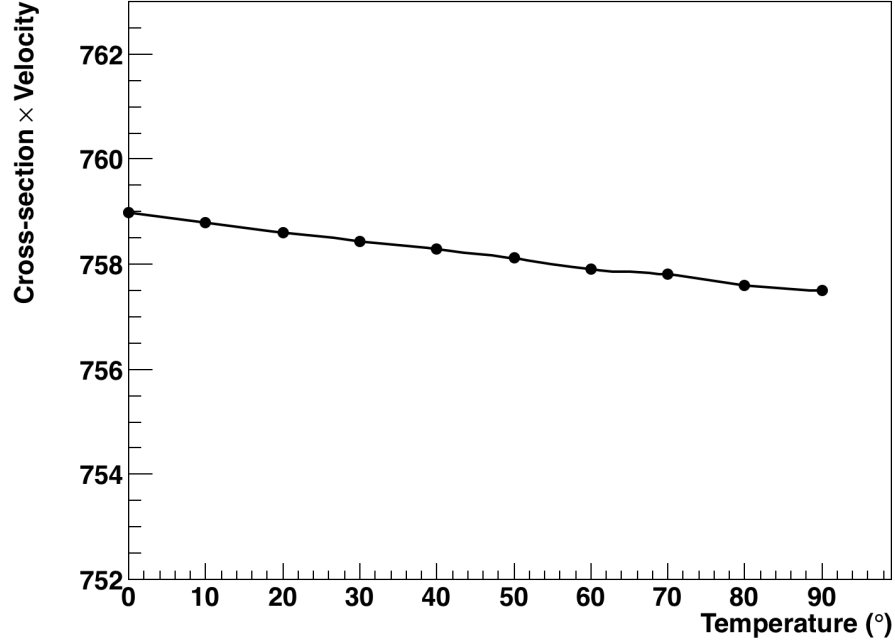


Figure 4.20: The (n, γ) cross-section \times velocity [barn \times m/s] as a function of temperature. Uncertainties are included but too small to be seen. Figure is from [77].

efficiency E .

	fit function	data cleaning	neutron energy	source encapsulation	temp. variation	total
τ	$-0.86^{+0.11}_{-0.12}\%$		$-0.025\pm 0.094\%$	$-1.38^{+0.35}_{-0.27}\%$	$\pm 0.051\%$	$-2.26^{+0.38}_{-0.31}\%$
E	$0.21\pm 0.29\%$	$1.89\pm 0.39\%$		$0.43\pm 0.20\%$		$2.53\pm 0.53\%$

Table 4.4: Systematic corrections and uncertainties for the $^{241}\text{Am}^9\text{Be}$ analysis. Values for τ are relative and those for E are absolute.

4.5 Final Results

4.5.1 Neutron Capture Time Constant and Neutron Detection Efficiency

The final results for the neutron detection efficiency E and capture time constant τ are calculated using Eqn. 4.11, Section 4.3.2 and Table 4.4. Note that the efficiency is measured with three central $^{241}\text{Am}^9\text{Be}$ runs, whereas τ is calculated using all internal calibration runs.

$$\begin{aligned} E &= (50.79 \pm 0.55)\%, \\ \tau &= 202.35^{+0.88}_{-0.76} \mu\text{s}. \end{aligned} \tag{4.15}$$

While E in Eqn. 4.15 includes the contribution from data cleaning sacrifice, this portion of data is not retrievable with normal data processing. Under the standard trigger settings and data cleaning criteria, the neutron detection efficiency at the center of the SNO+ detector is $(49.08 \pm 0.39)\%$. This efficiency for detecting 2.2-MeV γ s is the highest among pure water Cherenkov detectors.

The neutron capture time constant τ , is similar to that of another large water Cherenkov detector [68] ($203.7 \pm 2.8 \mu\text{s}$ (stat. only)), but with much-improved precision.

4.5.2 Thermal neutron-hydrogen capture cross-section

The thermal capture cross-section is computed using Eq. (4.13) and the thermal neutron velocity $v_{n,t}$:

$$\sigma_{\text{H},t} = \frac{1}{\tau v_{n,t} n_{\text{H}}}. \tag{4.16}$$

where n_{H} is the number density of hydrogen atoms.

For comparison purposes, the velocity $v_{n,t}$ is calculated for a kinetic energy of 0.02530 eV [80]. Using the non-relativistic expression for kinetic energy ($mv^2/2$) and the mass of the neutron ($m_n = 939,565,413 \text{ eV}/c^2$), a value of 2200.0 m/s is obtained.

The number density of hydrogen is calculated as

$$n_{\text{H}} = \rho w_{\text{H}} N_A / m_{\text{H}}, \quad (4.17)$$

where ρ is the density of water at the temperature and pressure at which the capture time was measured ($0.9991 \times 10^6 \text{ g m}^{-3}$), w_{H} is the mass fraction of hydrogen in H_2O (11.19%), N_A is Avogadro's number ($6.0221 \times 10^{23} \text{ mol}^{-1}$), and m_{H} is the molar mass of hydrogen ($1.0080 \text{ g mol}^{-1}$). The calculated $n_{\text{H}} = 0.6680 \times 10^{29} \text{ m}^{-3}$.

The thermal capture cross-section is thus calculated to be:

$$\sigma_{\text{H},t} = 336.3_{-1.5}^{+1.2} \text{ mb}. \quad (4.18)$$

Dedicated experiments have measured the thermal neutron-proton capture cross-section using strong-pulsed sources to create a large number of neutrons in smaller water volumes. The decay of the population of neutrons is then evaluated as a function of time. The most precise measurements are $334.2 \pm 0.5 \text{ mb}$ [81] (1965) and $332.6 \pm 0.7 \text{ mb}$ [82] (1977). In contrast, the measurement presented here was made by analyzing the capture time distribution of individual neutrons, in a much larger, uniform, pure water Cherenkov detector. In 2018, ENDF/B-VIII.0 updated their thermal capture cross-section from 332.00 mb to 332.58 mb [83], noting that it now agrees better with one of the most precise experimental values [82].

In total 23 previous measurements have been carried out, of which the global

average is 332.61 mb. Among all 24 measurements, the SNO+ value is the third most precise. Fig. 4.21 plots all of these measurements as a function of publication years.

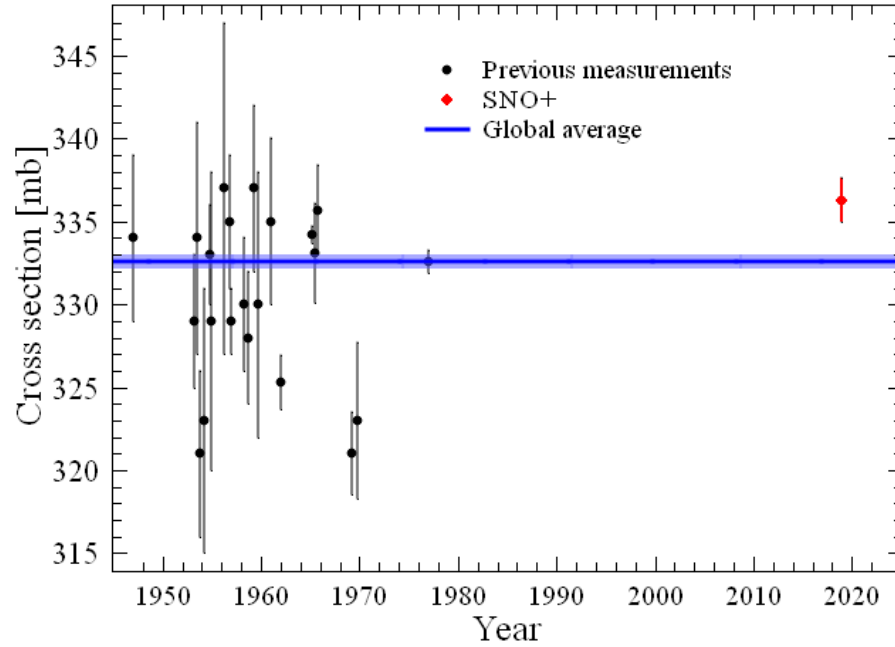


Figure 4.21: Thermal $n-p$ radiative capture cross-section measurements as a function of publication year. [82]

Chapter 5

The Monte Carlo Simulation for the $^{241}\text{Am}^9\text{Be}$ Calibration

Even though a Monte Carlo simulation for the $^{241}\text{Am}^9\text{Be}$ calibration is not required for the analysis method and raw results presented in Chapter 4, such a simulation is necessary for evaluating the systematic effects for the analysis. In particular, the simulation is important in calculating systematic effects for the initial neutron energy spectrum and the source encapsulation. Additionally, the simulation with user-defined positions can produce a detector map of neutron detection efficiency, from which a volume-weighted average can be derived. Furthermore, the Monte Carlo simulation can be used to carry out an energy calibration based on the 4.4 MeV γ s, which is complementary to the main energy calibration program in SNO+ using a ^{16}N source.

This chapter introduces the details of the $^{241}\text{Am}^9\text{Be}$ Monte Carlo simulation, followed by a thorough comparison between data and Monte Carlo for some important event properties. Features identified in the neutron detection efficiency map are also discussed and a volume-weighted neutron detection efficiency for the full detector

volume is presented. The energy calibration using the 4.4 MeV γ s will be discussed in Chapter 6.

5.1 Monte Carlo with the $^{241}\text{Am}^9\text{Be}$ Source

Similar to other experiments in the high energy physics field which have dedicated, experiment-specific software for Monte Carlo simulation, SNO+ utilizes RAT as its main software tool for performing this task. As discussed in Section 2.4, RAT is an adapted simulation package that integrates different software components including geometry modeling, event generation, particle tracking, detector response, and event reconstruction. For this reason, RAT receives contributions from a wide range of working groups in the collaboration, and is regularly updated and maintained. Prior to the SNO+ $^{241}\text{Am}^9\text{Be}$ calibration in the water phase, there were already utilities inherited from SNO that perform basic $^{241}\text{Am}^9\text{Be}$ calibration simulations. This section discusses the improvements made to the existing $^{241}\text{Am}^9\text{Be}$ simulation framework, which include a new source geometry, a new $^{241}\text{Am}^9\text{Be}$ event generator, the determination of source positions, trigger efficiency modeling, and an empirical neutron simulation cutoff.

5.1.1 The $^{241}\text{Am}^9\text{Be}$ Source Geometry

The $^{241}\text{Am}^9\text{Be}$ source as it was shipped from the production company can be seen in Fig. 3.1. The radioactive part of the source is very small, occupying approximately a $10\times 8\times 8$ mm³ space. Enclosing the source is a thin layer (~ 2 mm) of stainless steel, which is further surrounded by multiple layers of Delrin as encapsulation (see Section 3.2). The Delrin encapsulations are sealed with stainless steel screws and

nuts. In addition to the source assembly, the Teflon holder that secures the source assembly to the calibration carriage is also simulated.

Shown in Fig. 5.1 is the updated source geometry with the new encapsulation added, which is split into four subvolumes: the radioactive source itself, an inner encapsulation layer, the air pocket and an outer wall to seal off the air pocket. A few approximations are made to the source materials for simplicity purposes. Firstly, the material of the radioactive source is approximated to Delrin as the details about the setup of the powder source is unknown. The effect of the change is minimal since Delrin is not a strong neutron absorber. The thin layer of stainless steel, as well as the screws, nuts, wires used to seal and secure the source assembly, is also omitted in the geometry construction. The air pocket volume is filled with the air of an adjusted pressure (since the air inside the source is compressed during the assembly process).

The simulated geometry in RAT is created through a LEGO-style combination (no overlapping allowed) of different GEANT4 [50] objects. Because of the geometrical characteristics of the source, the four subvolumes can all be constructed as cylindrical objects. In GEANT4, an object is defined with two volumes: a logical volume and a physical volume. The logical volume specifies the object's mother volume, that is, the volume that this object should exist in. Additionally, it also denotes the object's dimensions and material. The physical volume, on the other hand, deals with the placement of the object by controlling its position and rotation relative to its mother volume.

An $^{241}\text{Am}^9\text{Be}$ source geometry factory file creates the daughter volumes shown in Fig. 5.1 inside the "AV" mother volume, which is the volume containing every object inside the AV. The dimensions and relative position of each object are predefined

in a RAT database (RATDB), with an additional position vector relative to the "AV" volume, which will be further discussed in Section 5.1.3. Potential overlaps are checked prior to building the geometry.

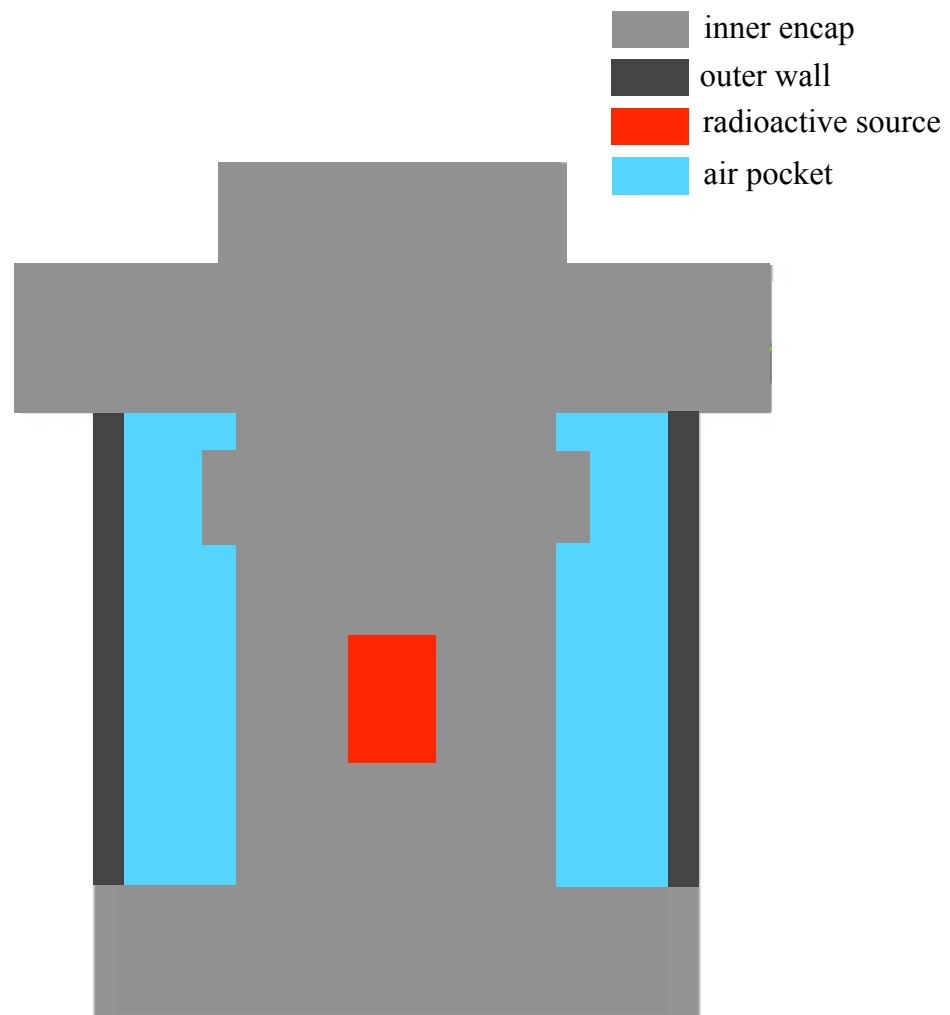


Figure 5.1: The cross-sectional profile of the updated $^{241}\text{Am}^9\text{Be}$ source geometry constructed for Monte Carlo production.

5.1.2 The $^{241}\text{Am}^9\text{Be}$ Source Event Generator

The RAT event generator provides functionalities of simulating events with specified types and customized time and position profiles. A top-level generator can be declared in the simulation to determine the type of event (e.g. solar neutrinos or ^{16}N decays), which is followed by a few second-level generators as arguments. The second-level generators provide further information including the vertex (the momenta and polarization of the particles), position, and time. The position generator allows events to be generated from one or more customized point, surface, or volume and the time generator can generate events either uniformly or Poisson-like.

The coincidence generator, one of the available top-level generators and originally implemented for pile-up event studies for the $0\nu\beta\beta$ search, was adapted to produce the $^{241}\text{Am}^9\text{Be}$ source events. The coincidence generator allows events to be generated in a pair with a user-defined interevent time difference. For the $^{241}\text{Am}^9\text{Be}$ source event, the neutrons are produced a few tens of picoseconds after the prompt γ s, which is negligible in the context of the $^{241}\text{Am}^9\text{Be}$ analysis. Taking advantage of the vertex generator, both the γ s and the neutrons can be simulated with user-defined energy spectra. The γ spectrum is obtained from ^{12}C de-excitation [80] and the neutron spectrum is derived from [76] in SNO. It is worth noting that different $^{241}\text{Am}^9\text{Be}$ sources can have different neutron spectra, as the emitted neutron energy is dependent on the set up of the source.

The $^{241}\text{Am}^9\text{Be}$ events are generated within the logical volume of the radioactive source object. The time of the event pairs is configured to follow a Poisson distribution.

5.1.3 Determination of Source Positions and the AV/PSUP Offset

During the $^{241}\text{Am}^9\text{Be}$ source deployment, the source positions are logged into the calibration database (MANIP) every 10 seconds to track the source movement. The position data is then processed to obtain a central value and is written into the run table in the main database (RATDB) for calibration runs. To generate the $^{241}\text{Am}^9\text{Be}$ Monte Carlo, a list of $^{241}\text{Am}^9\text{Be}$ calibration run numbers needs to be provided to retrieve the source positions from the ratdb tables.

Since the source position is measured in the Manipulator system, it is recorded relative to the AV coordinates. However, the position reconstruction, which uses the timing and positions of the PMT hits, reconstructs events in PSUP coordinates. As the AV has some freedom along the vertical direction to allow adjustment in the rope tensions, it is possible that these two coordinates do not coincide. In fact, it was shown by multiple independent studies [84] [85] [86] [87] that during the SNO+ water phase the AV is shifted upwards with respect to the PSUP center by 10.8 cm. This difference is subtracted from the reconstructed position along the z-axis after position reconstruction and a new radius of the event are recalculated afterward. In the following discussions, all the coordinates are given in the AV system of reference.

5.1.4 Modeling the Trigger Efficiency

The trigger efficiency [73] is the probability of producing a global trigger for an event with a given number of PMT hits in the prompt trigger window. This is especially important for the $^{241}\text{Am}^9\text{Be}$ Monte Carlo since the trigger efficiency is less than 100% for low nhits events. In fact, as shown in Fig 5.2, the neutron detection efficiency is ultimately limited by this trigger efficiency (curve). The trigger efficiency processor

measures the trigger efficiency using the nhits monitor, a periodically run program that artificially increases fired PMT hit one by one. Specifically, the nhits monitor was run after every $^{241}\text{Am}^9\text{Be}$ calibration run and was used to derive a run-by-run trigger efficiency curve. Fig. 5.2 shows a generally good agreement of the trigger efficiency curve between Monte Carlo and that measured by the nhits monitor.

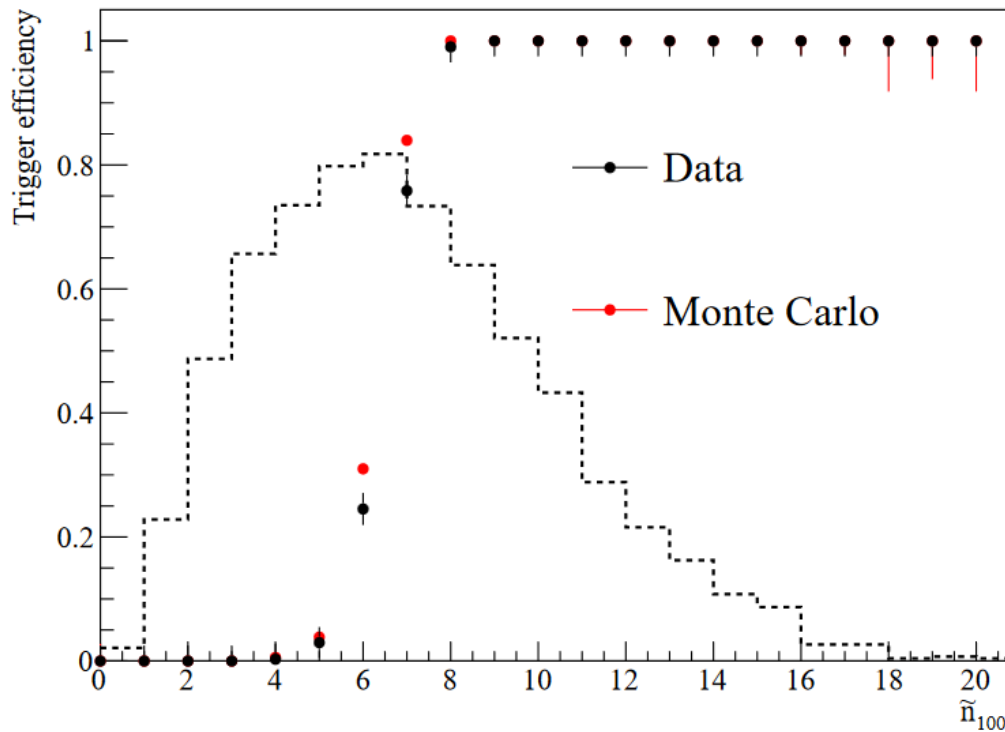


Figure 5.2: The trigger efficiency curve of a central $^{241}\text{Am}^9\text{Be}$ run from the nhits monitor (Data) compared to the realistic trigger model in Monte Carlo. A simulated nhits distribution of the neutron signal with perfect trigger efficiency is overlaid on top. Please note that the x-axis plots the prompt nhits only.

5.1.5 Neutrons Transport in Water

Most of the neutrons of the energy range from 1 to 10 MeV will get absorbed in the water on a fairly small time scale of ~ 0.2 ms. However, some neutrons traversing

in the detector will linger for a long time before they eventually get absorbed and create long-lived isotopes. This causes a problem with the length of the simulation, as sometimes the particle gets stuck in endless loops. Events created by these neutron and secondary particles are of little interest to the $^{241}\text{Am}^9\text{Be}$ analysis. To fix this issue, two cutoff thresholds were implemented on the time and number of steps for the neutrons to be propagated [88]. In order to reduce any possible systematic effects, the two cutoffs were made to be extremely generous, being 1 s and 1000 steps respectively. [88] simulated MCs with and without these two cutoff thresholds were compared and the minimal effect was found.

5.1.6 Data Structure for the $^{241}\text{Am}^9\text{Be}$ Simulation

The data storage scheme in RAT is built upon ROOT [51], a data processing and storage toolkit widely used in the high energy physics field. ROOT organizes its data in a tree-like style, where event information is stored inside a hierarchy of branches and leaves. In SNO+, the main branches include the MC branch which stores Monte Carlo information of initial particles, the MCEV branch which contains uncalibrated raw event information, and the EV branch of calibrated PMT hits as well as event reconstruction properties.

Since the $^{241}\text{Am}^9\text{Be}$ events are generated in pairs, the simulated Monte Carlo file has a different data structure from the actual data. In the data collected from the DAQ system, each entry corresponds to one event. However, in the Monte Carlo one entry can contain zero to two events (particles) depending on how many events trigger the detector. This leads to a structural difference in dealing with the data and MC. For the MC files, entries are pre-scanned to have both events triggering the

detector so that they can be compared to the coincidence pairs in the data.

5.2 Comparison between Data and Monte Carlo

Using the updated $^{241}\text{Am}^9\text{Be}$ Monte Carlo framework, 600,000 coincidence events are simulated for each internal source position (1,800,000 for the detector center). This corresponds to an MC to data ratio of ~ 10 . The nhits and other important reconstructed quantities such as the energy and position are compared. For the calibration data, the nhits distributions are derived using the method described in Chapter 4 and other distributions are taken from the spectral differences between the 0 to 500 μs region and 500 to 1000 μs .

5.2.1 Data-MC Comparison for a Central Run: 109134

The nhits Distribution

Fig. 5.3 shows the data-MC comparison of event nhits for both neutron signals and the 4.4 MeV γ s. Due to the trigger efficiency curve, the nhits distribution of the neutron signal does not follow a Gaussian, but instead is skewed towards higher nhits values. To compare data with MC, the Monte Carlo is normalized to the data for the region $\text{nhits} \geq 10$. A modest agreement in this range is observed. However, the Monte Carlo and data differ significantly as the nhits moves to lower values. This can be attributed to the overestimated trigger efficiency at low nhits regions by the realistic trigger model.

The agreement between data and MC improves substantially for the 4.4 MeV γ s. Immune to the trigger effect for the majority part of the nhits distribution, both data and MC exhibit a Gaussian distribution, with a central value at around 22 nhits.

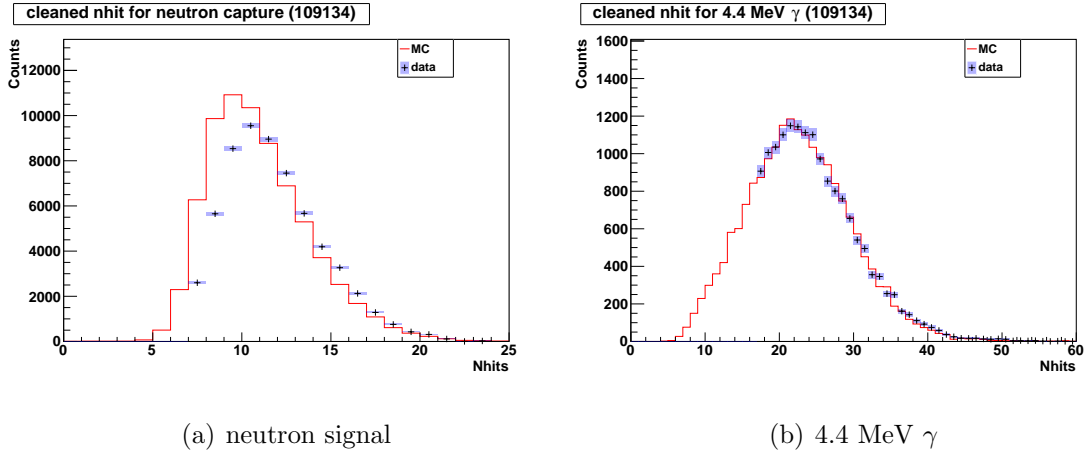


Figure 5.3: Data-MC comparison of nhits for the neutron and 4.4 MeV γ signals for a central $^{241}\text{Am}^9\text{Be}$ run.

Reconstructed Energy and Position Distribution

A water-fitter is used in the SNO+ water phase to reconstruct event position and energy. The fitter [89] was originally developed in SNO, with the basic approach that maximum likelihood techniques are applied to the prompt PMT hit times (and sometimes charges) of the event to look for the best vertex (position and direction of the event). The energy is determined based on the event position and number of prompt PMT hits through an RSP energy estimator [90]. Fig. 5.4 and 5.5 compares reconstructed energy and position.

A significant deviation from data is observed for energy below 2.5 MeV for both the neutron and 4.4 MeV γ signals. Apart from the trigger efficiency discrepancy shown in the nhits distributions (Fig. 5.3), this becomes more serious due to the fact that the RSP function used in SNO+ becomes less ideal for low energy events because of the decreased fraction of prompt PMT hits. For the 4.4 MeV γ s, the Monte Carlo did a decent job reproducing the energy spectrum above 2.8 MeV, providing another

piece of the evidence that the trigger efficiency in this region becomes 100% [43].

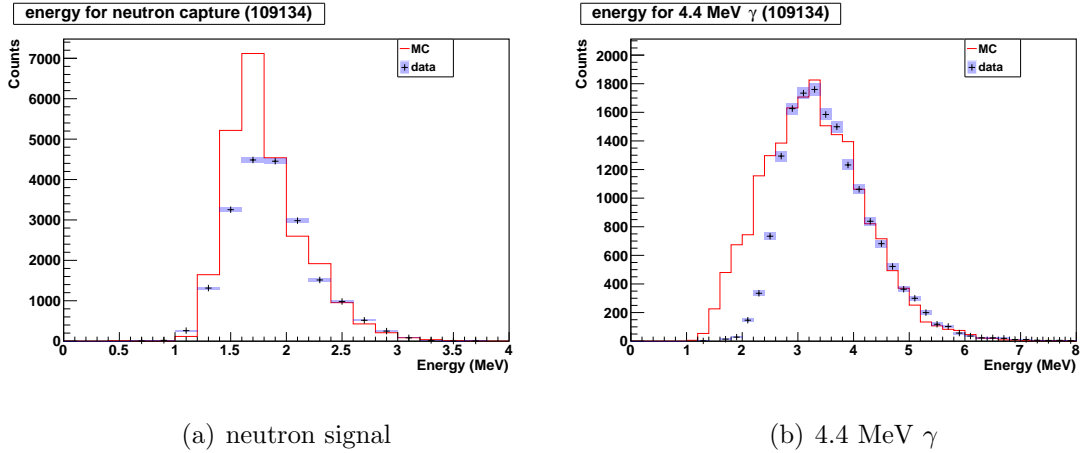


Figure 5.4: Data-MC comparison of reconstructed energy for neutron and 4.4 MeV γ signals for a central $^{241}\text{Am}^9\text{Be}$ run.

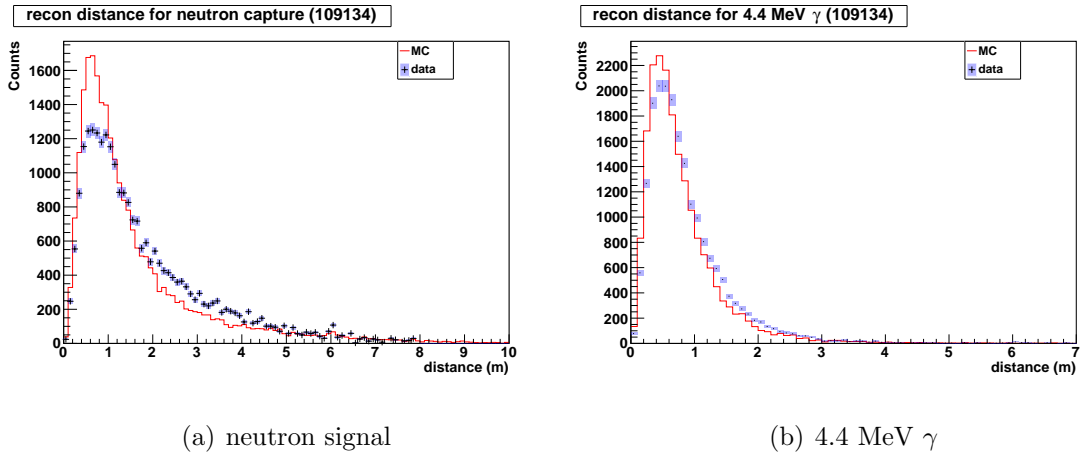


Figure 5.5: Data-MC comparison of reconstructed distance for neutron and 4.4 MeV γ signals.

Fig. 5.5 shows the distribution of the distance between where particles are emitted and their reconstructed positions. γ s of ~ 5 MeV travel approximately 40 cm in water

before Compton scattering. Although data shows that the reconstruction is a little worse than the MC, they agree to a good extent for both the neutron signals and the 4.4 MeV γ s.

Isotropy parameter β_{14}

β_{14} [91] is a sophisticated parameter that was also developed in SNO to measure an event's isotropy. The l^{th} β parameter is defined as the average value of the Legendre polynomial, P_l , of the cosine of the angle with respect to the reconstructed position between each pair of PMT hits in the event. The combination $\beta_{14} = \beta_1 + 4\beta_4$ is found to be the best parameter to estimate the event's isotropy. Events with smaller values of β_{14} are more isotropic.

The MC predicted a bigger value of β_{14} than observed in data for both neutron signals and the 4.4 MeV γ s. Though very small, the bias is consistent with what was seen in ^{16}N calibration data [92]. Several studies [93] [94] have looked into the discrepancy over many aspects of the simulation including the integrity of optics and scattering models but no single source was identified to fully explain this discrepancy.

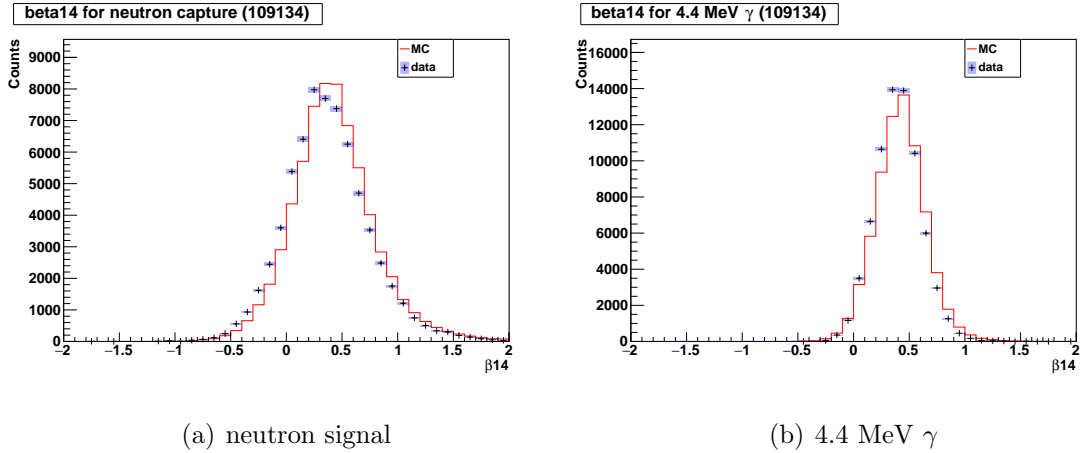


Figure 5.6: Data-MC comparison of β_{14} for neutron and 4.4 MeV γ signals.

ITR

ITR is the acronym of In-Time Ratio. It is defined as the ratio of the number of nhits which have a time residual between -2.5 and 5.0 ns to the total number of nhits of this event. The time residual for each hit PMT is given by:

$$t_{res} = t_{PMT} - \frac{r_{PMT}}{c_{avg}}, \quad (5.1)$$

where t_{PMT} is the PMT hit time, r_{PMT} is the distance from the event to the PMT, and c_{avg} is the weighted average speed of light in water and AV.

A small value of event ITR means that it has very few prompt hits, which could indicate either that the event is not physical (e.g. due to dark noise) or that the event is mis-reconstructed so that ITR is artificially pushed down.

ITR is an important high-level parameter that is conventionally used to remove backgrounds. However, because of the low energy of the events (thus the small number

of PMT hits), the agreement of data and MC for both neutron signals and the 4.4 MeV γ s are suboptimal. At lower energies, events are more likely to have low ITR values because of the scarcity of prompt PMT hits.

5.2.2 Data-MC Comparison Across the Detector

The trend of data-MC comparison across the detector is examined over ~ 20 positions that the $^{241}\text{Am}^9\text{Be}$ source has been deployed at. Fig. 5.8 to 5.15 display the results for nhits, energy, β_{14} and ITR.

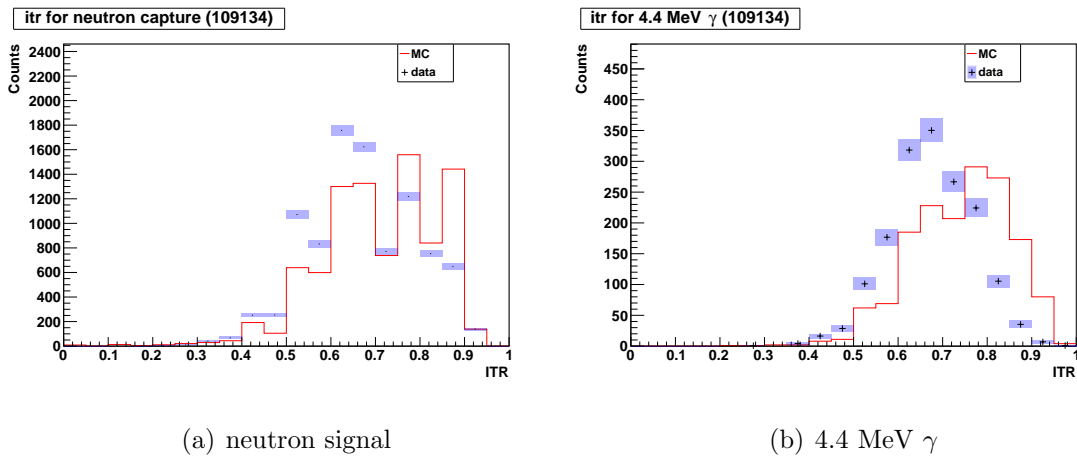


Figure 5.7: Data-MC comparison of ITR for neutron and 4.4 MeV γ signals.

The nhits distributions of the neutron show an overestimation from MC at $\text{nhits} \leq 10$ region consistent for all source positions, but is especially exaggerated for high radii. For the 4.4 MeV γ s, the data and MC are in generally good agreement within 3 m, while the effect from MC overestimation starts to show up from 4.5 m.

The energy distributions of the neutron signal display a strong dependence on the radius of the source position. The ratio of the number of events predicted by MC to

data below 2 MeV significantly decreases as the source moves to higher radii. Data and MC have the best agreement for radius between 3 m and 4.5 m. On the other hand, the 4.4 MeV γ s energy distributions show a consistent MC overestimation in the energy range below 2.5 MeV. Discrepancies between data and MC are also observed at the peak of the distribution for radius ≥ 4.5 m.

β_{14} predicted by the MC is consistently lower than the data, regardless of the energy or position of events. Similarly, a $\sim 10\%$ overestimation of ITR is observed across different source positions.

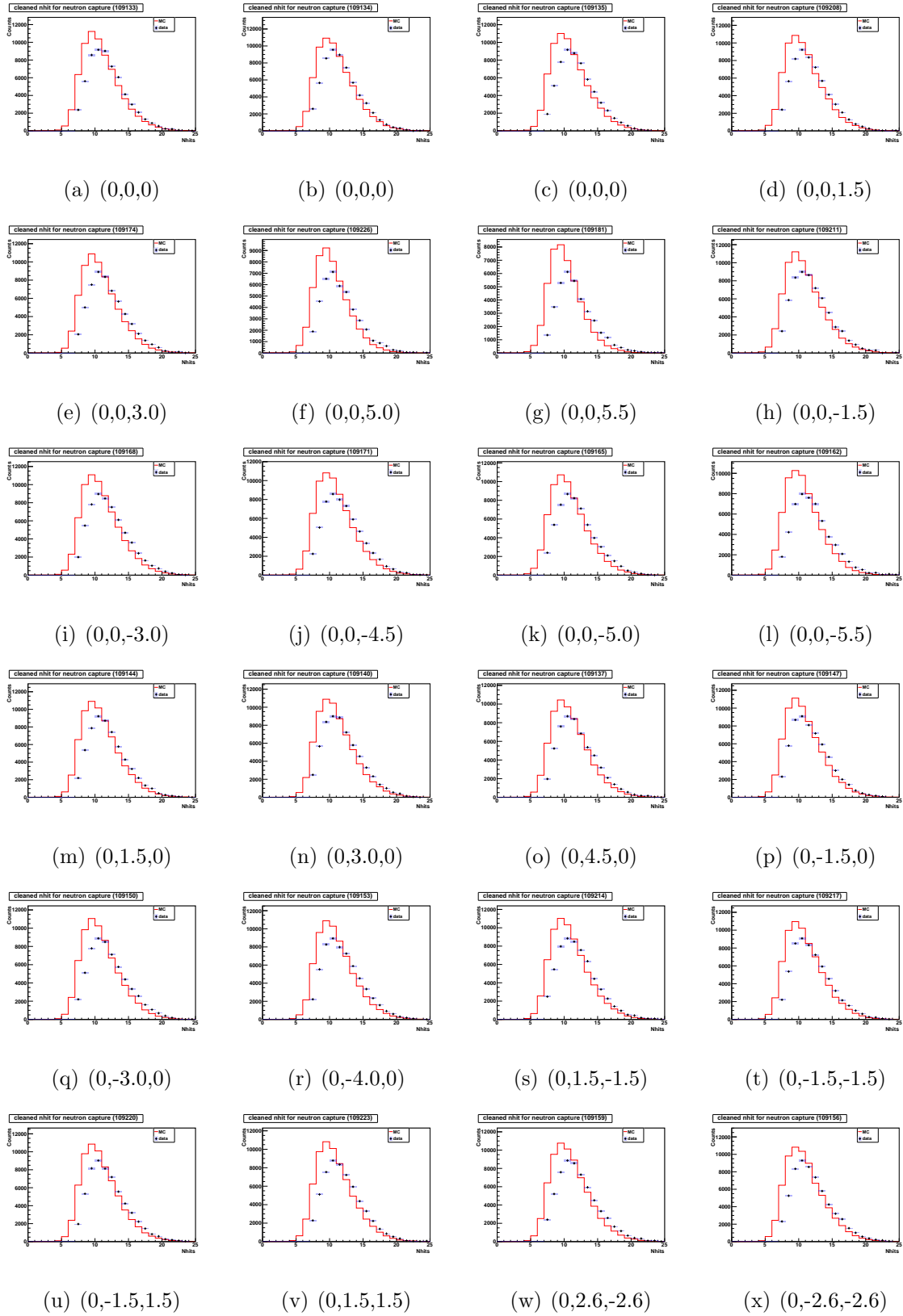


Figure 5.8: Nhits distributions for neutron signals at different positions of the detector.

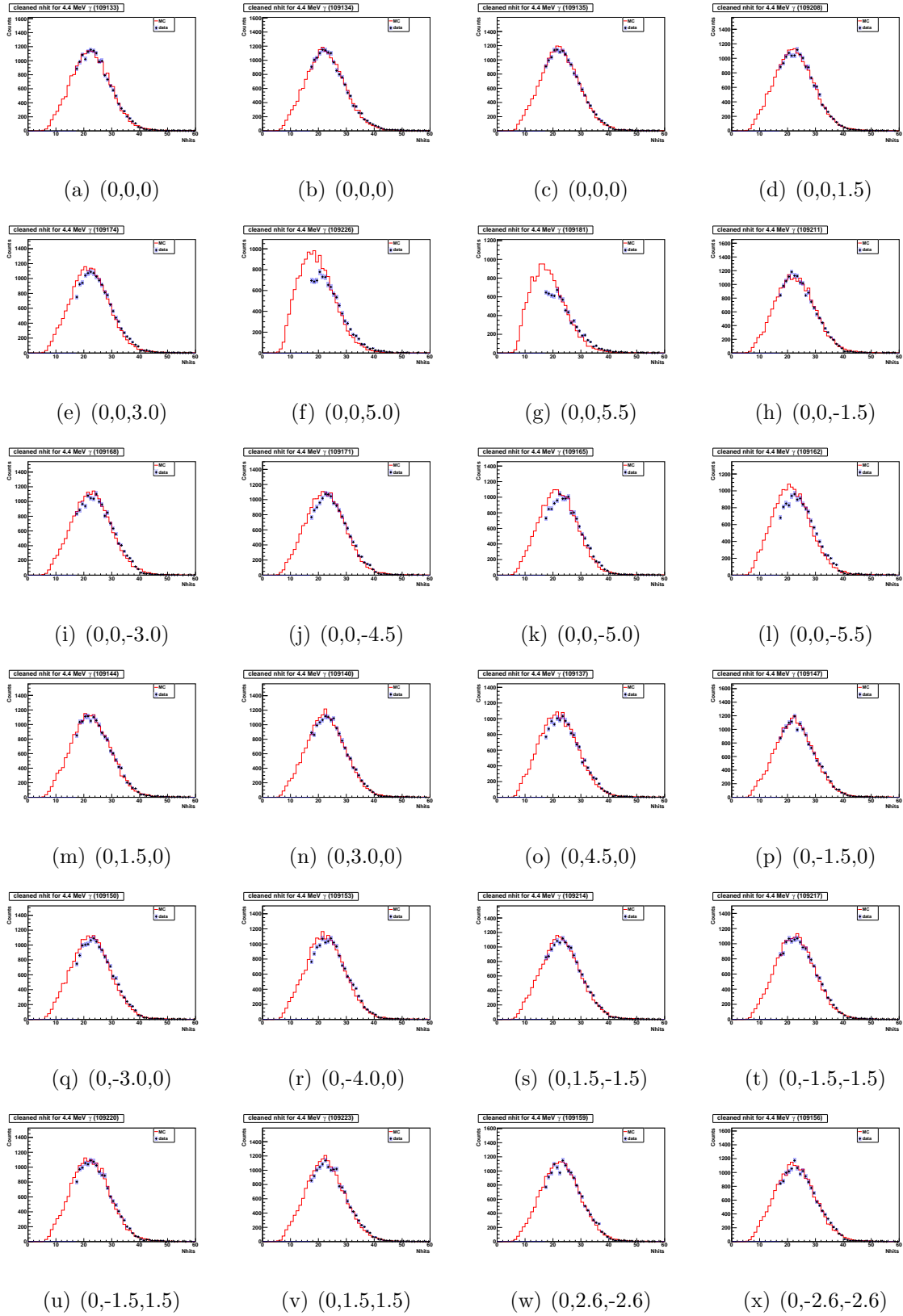


Figure 5.9: Nhits distributions for the 4.4 MeV γ s at different positions of the detector.

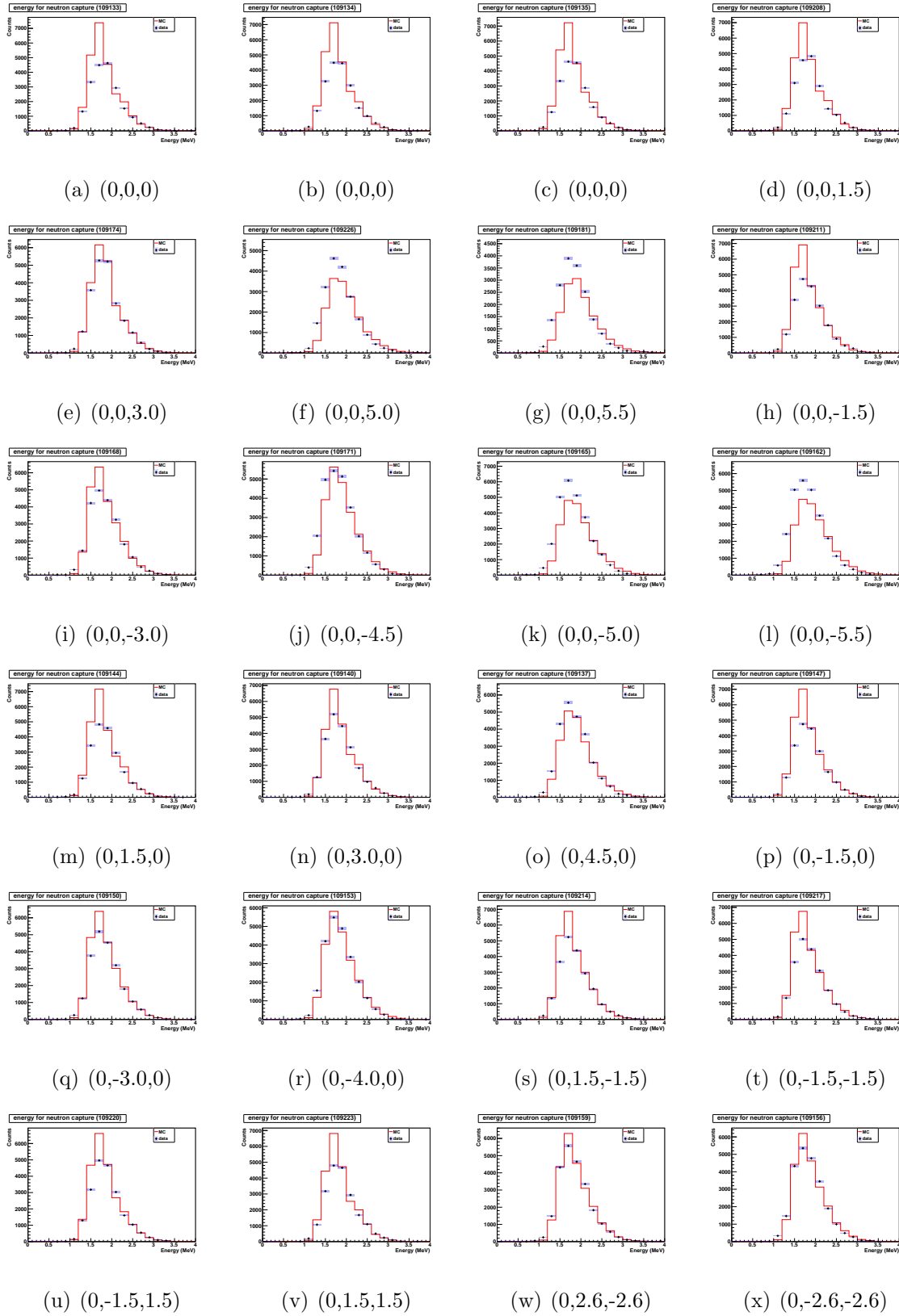


Figure 5.10: Reconstructed energy spectra for neutron signals at different positions of the detector.

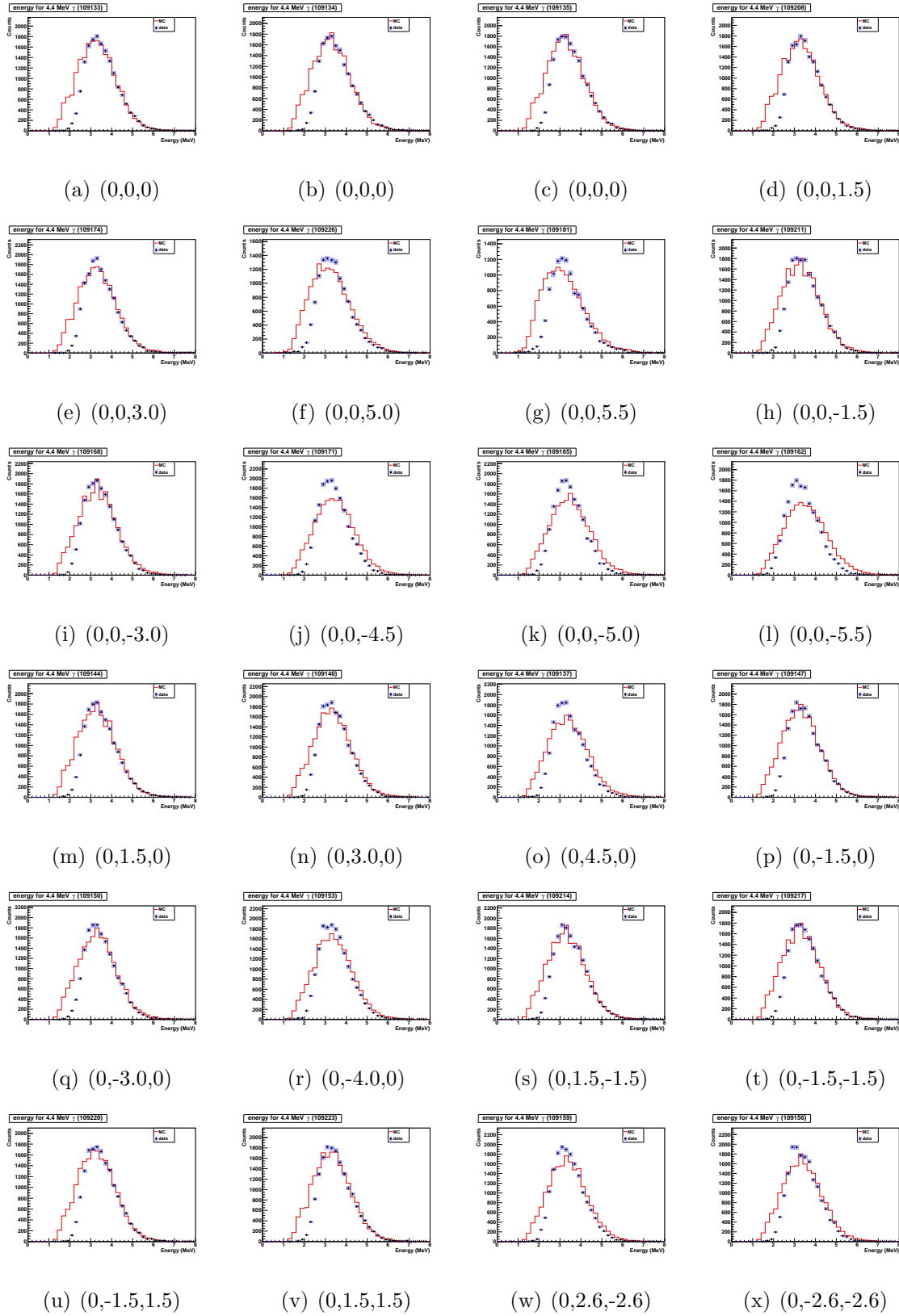


Figure 5.11: Reconstructed energy spectra for the 4.4 MeV γ s at different positions of the detector.

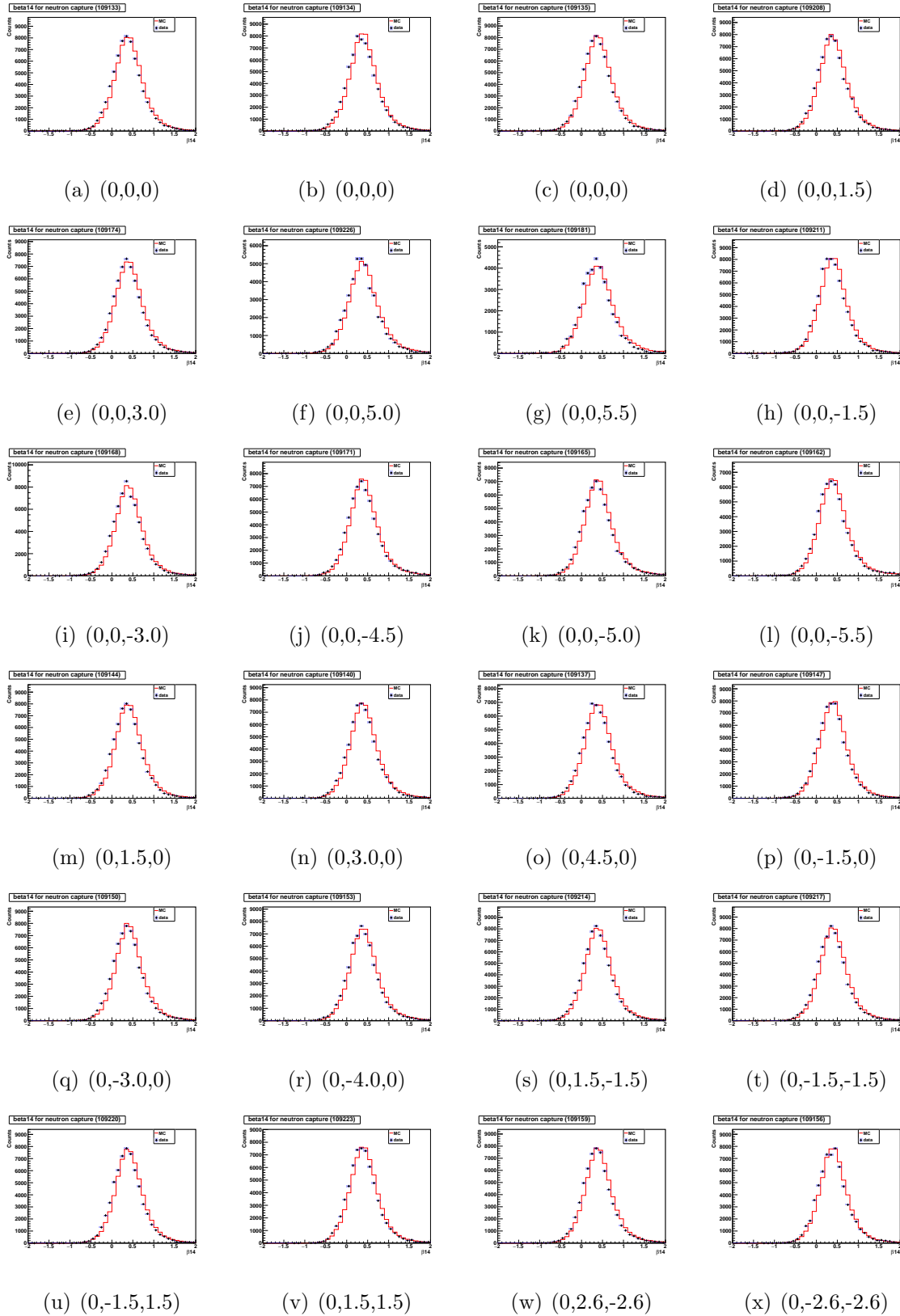


Figure 5.12: β_{14} distributions for neutron signals at different positions of the detector.

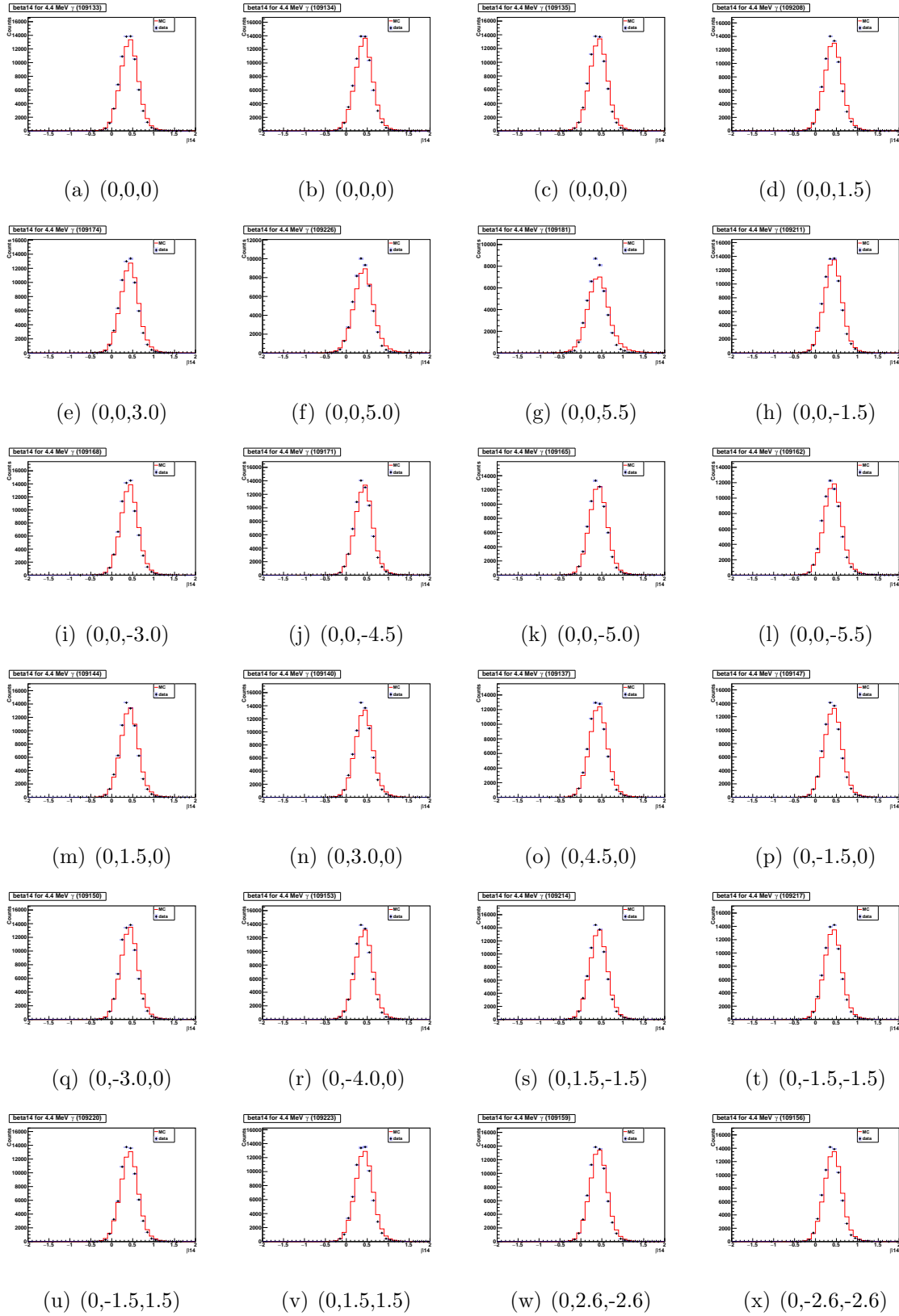


Figure 5.13: β_{14} distributions for the 4.4 MeV γ s at different positions of the detector.

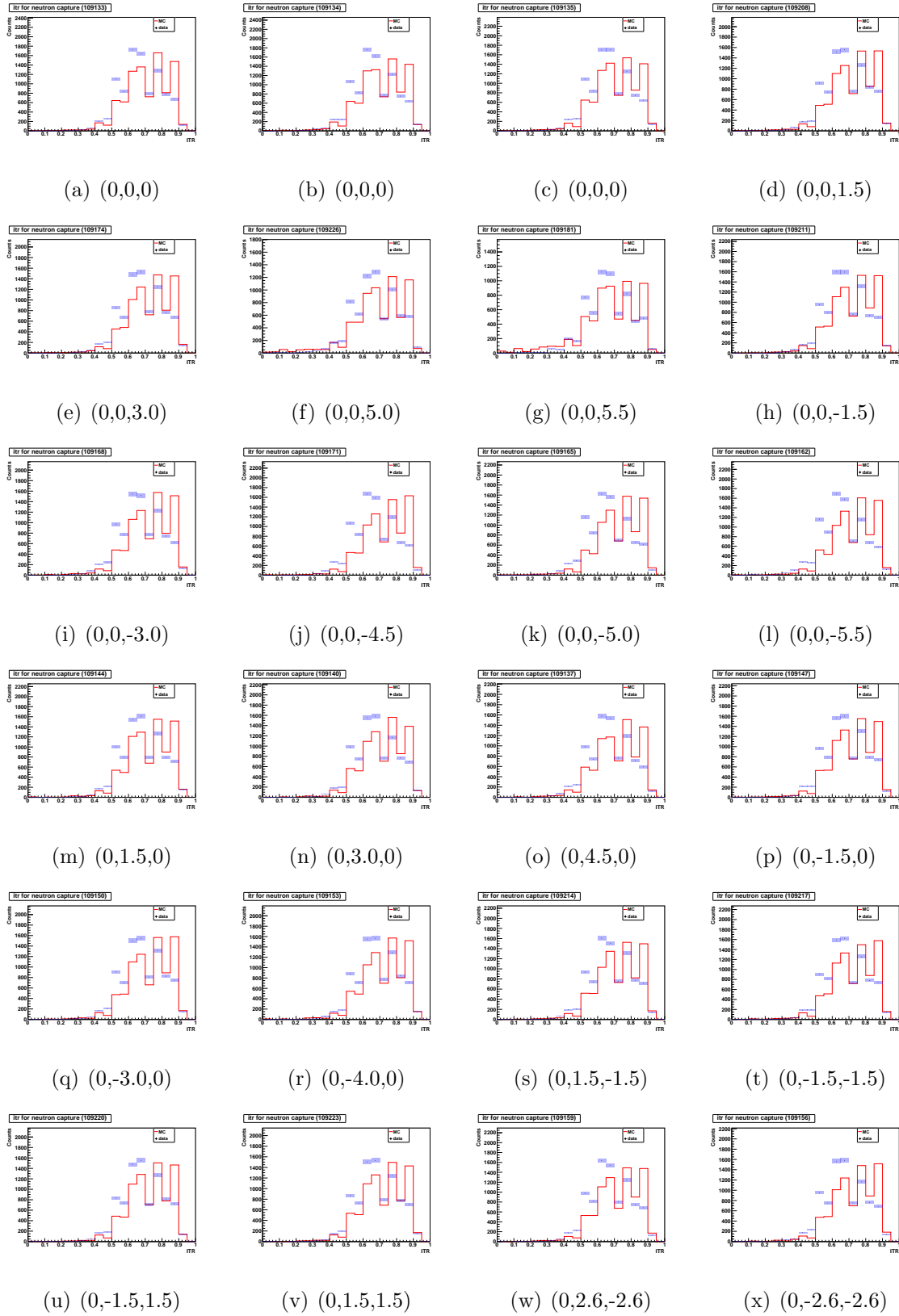


Figure 5.14: ITR distributions for neutron signals at different positions of the detector.

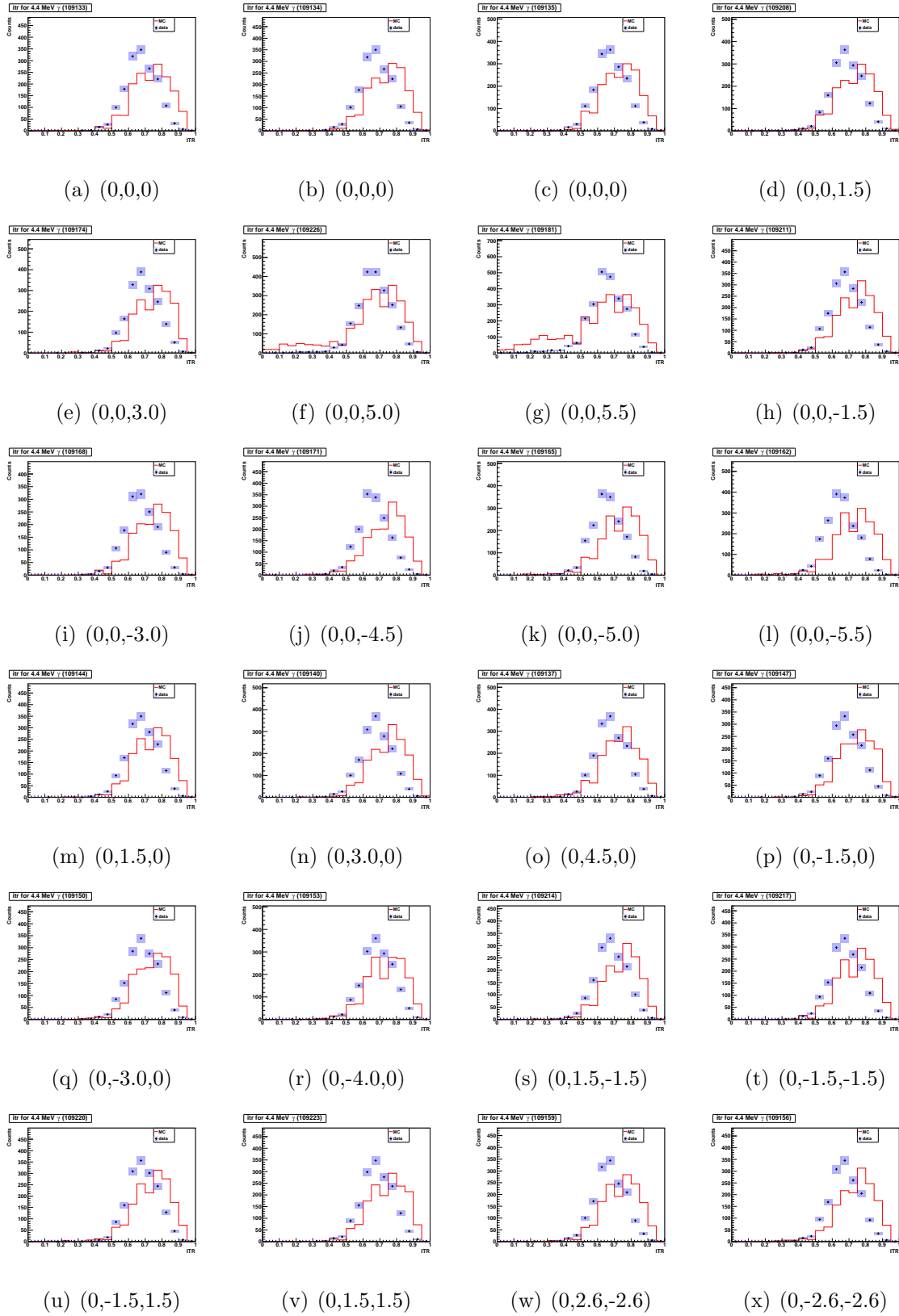


Figure 5.15: β_{14} distributions for the 4.4 MeV γ s at different positions of the detector.

5.3 Volume-weighted Neutron Detection Efficiency

Although over 20 positions inside the AV have been surveyed using the $^{241}\text{Am}^9\text{Be}$ source, the step size of the source movement is too big to accurately calculate a volume-weighted neutron detection efficiency. Using the internal calibration data, variations of the neutron detection efficiency were observed as a function of position. As shown in Fig. 4.9, the neutron detection efficiency drops significantly as the radius increases along the positive z-direction. Other possible position-dependent features can be more subtle and not discovered due to the small number of positions covered. The $^{241}\text{Am}^9\text{Be}$ Monte Carlo can be used to study these features and produce the best estimate of a volume-weighted detection efficiency.

As mentioned in Section 5.1.4, a realistic trigger model was used to simulate trigger efficiency when generating MC data. Due to the complex nature of such modeling, it can be inferred from Fig. 5.8 that for events below 10 nhits the trigger model can have a systematic overestimation of around 10% [95]. Fig. 5.16 shows that a linear relationship can be derived between the neutron detection efficiency simulated in MC and that measured from data. The size of this systematic effect is reflected in the slope, which is fitted to be 0.875 ± 0.037 or about $(\frac{1}{0.875} - 1) = 14\%$.

5.3. VOLUME-WEIGHTED NEUTRON DETECTION EFFICIENCY

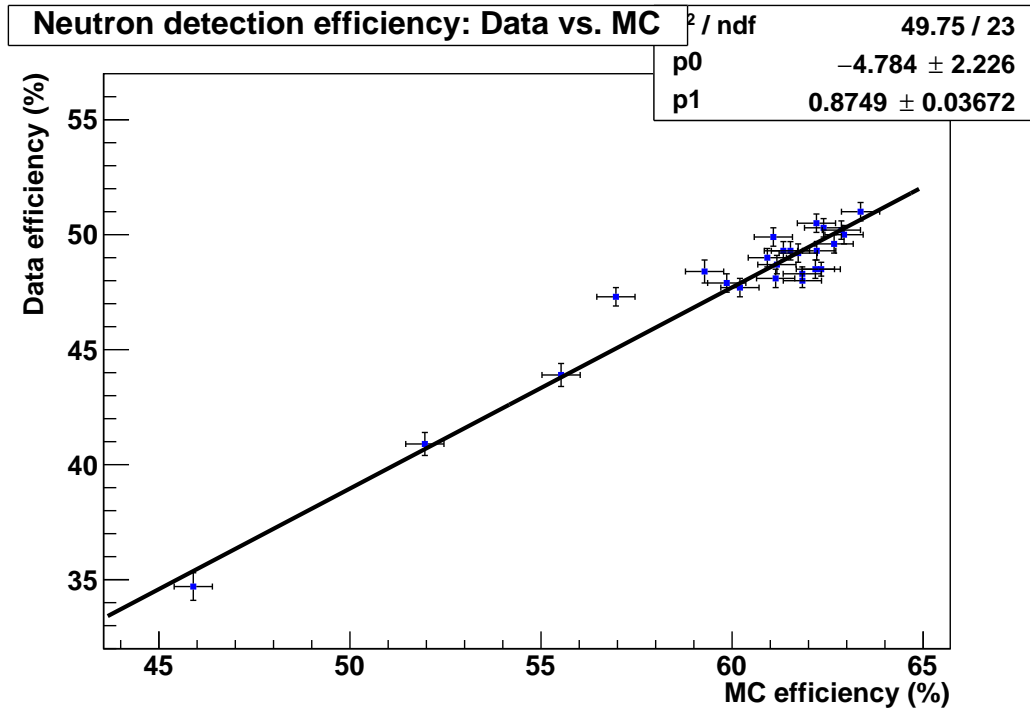


Figure 5.16: The neutron detection efficiency obtained from data vs. the neutron detection efficiency simulated with the realistic trigger model. A linear relationship can be drawn between these two quantities.

To study the position dependence of the neutron detection efficiency, 10,000 $^{241}\text{Am}^9\text{Be}$ neutrons are simulated at each of the grid of positions, on the XZ plane and YZ plane respectively. The obtained neutron detection efficiency is then corrected using Fig. 5.16. The positions are selected so that they are distributed uniformly and can be representative of the full detector volume. The planes are mapped in polar coordinates. On the radial axis, the source position is moved from 0 to 6 m with an incremental size of 0.5 m. On the angular axis, the positions are split with an interval of 10° if the radius is smaller than 3 m and every 5° for radius from 3 m to 6 m.

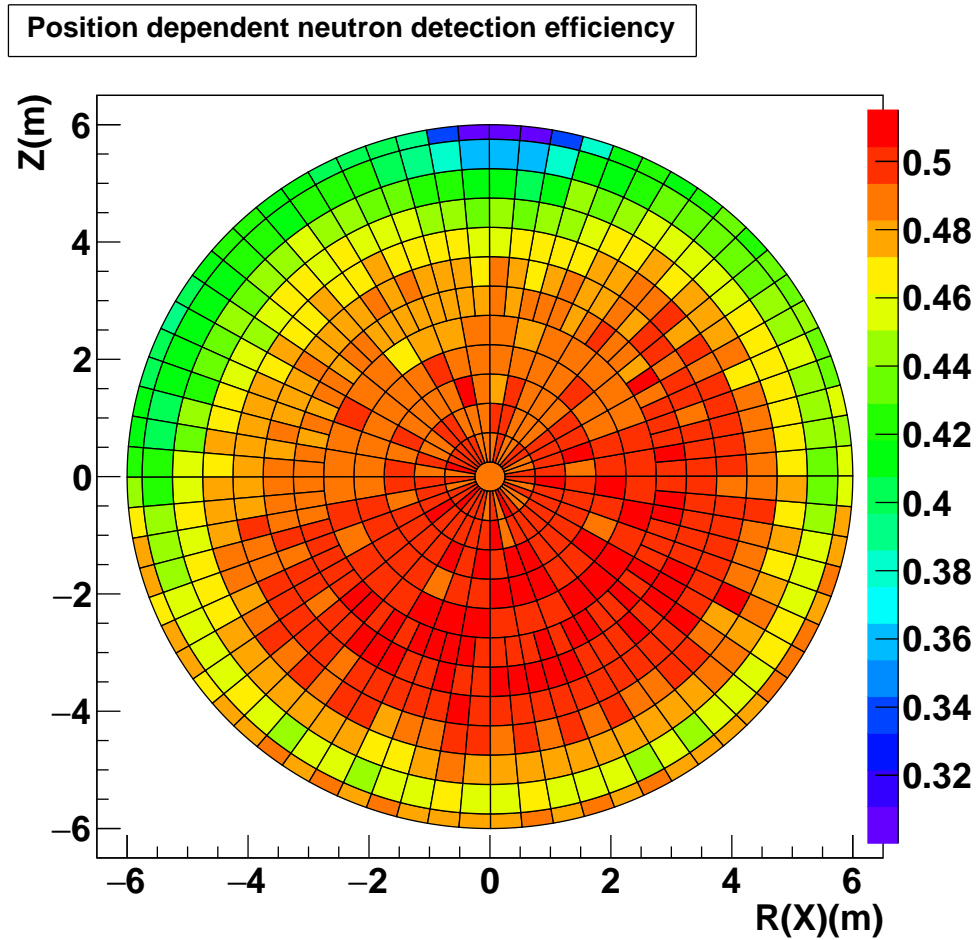


Figure 5.17: A 2D plot of corrected neutron detection efficiency in the XZ plane.

Fig. 5.17 and 5.18 are two polar plots that show the corrected MC neutron detection efficiency as a function of the position, for XZ plane and YZ plane respectively. The color-coded cells show the estimated neutron detection efficiencies for their represented volumes. Each cell occupies approximated a $20 \times 20 \times 20$ cm³ cube, the volume in which most neutrons will be absorbed if emitted from the center of the cell.

The two plots show similar features at the top of the detector volume, where the lowest neutron detection efficiency is found. This is later denoted as the “neck effect”, and can be attributed to the lack of PMT coverage around the neck. In fact, this

5.3. VOLUME-WEIGHTED NEUTRON DETECTION EFFICIENCY

“neck effect” is not constrained to the $z > 4.5$ m region, but rather affects the entire top hemisphere by roughly a drop of 2% compared to the bottom hemisphere.

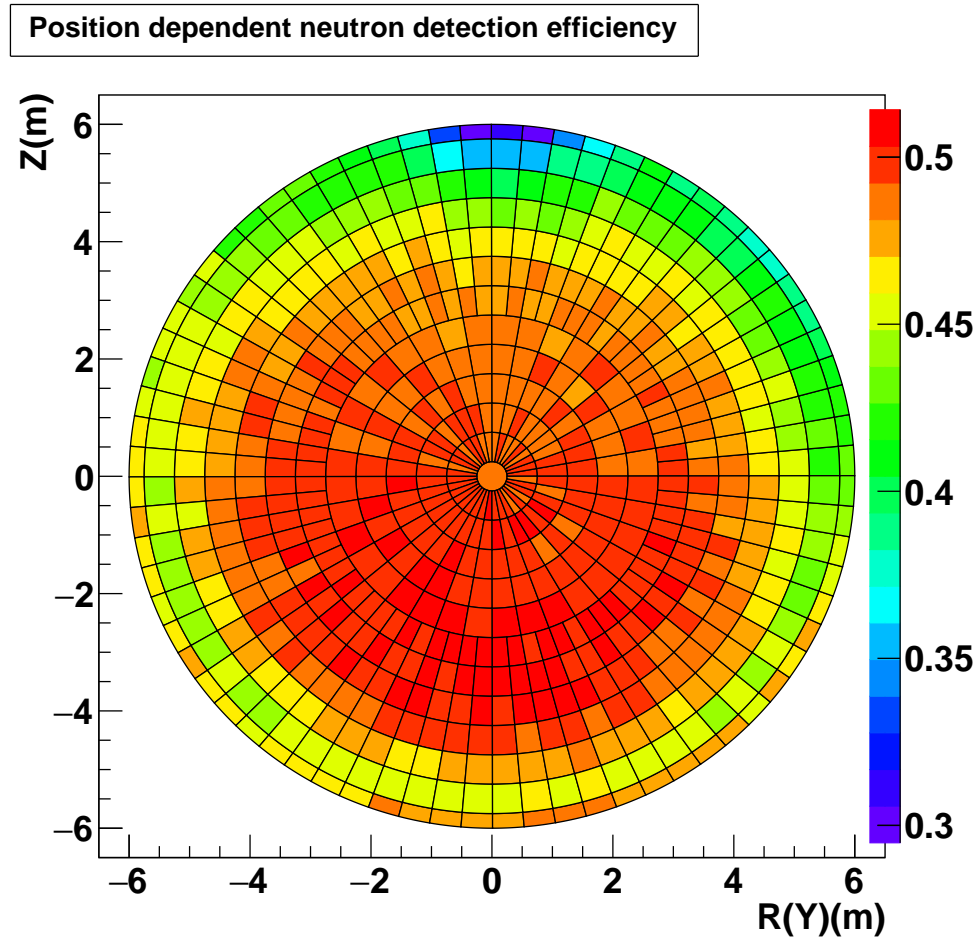


Figure 5.18: A 2D plot of corrected neutron detection efficiency in the YZ plane.

A general trend also exists that the neutron detection efficiency drops as the event position moves outwards. Fig. 5.19 is a plot of neutron detection efficiency as a function of radius. As can be seen in the plot, the neutron detection efficiency remains almost constant with only statistical fluctuation from 0 to 3 m, and drops about linearly as the radius increases. An unexpected feature is found near the edge

5.3. VOLUME-WEIGHTED NEUTRON DETECTION EFFICIENCY

of the AV in the bottom hemisphere, where the neutron detection efficiency has a small boost over its adjacent inner volume. This could be due to the optical effect of the hold-down ropes.

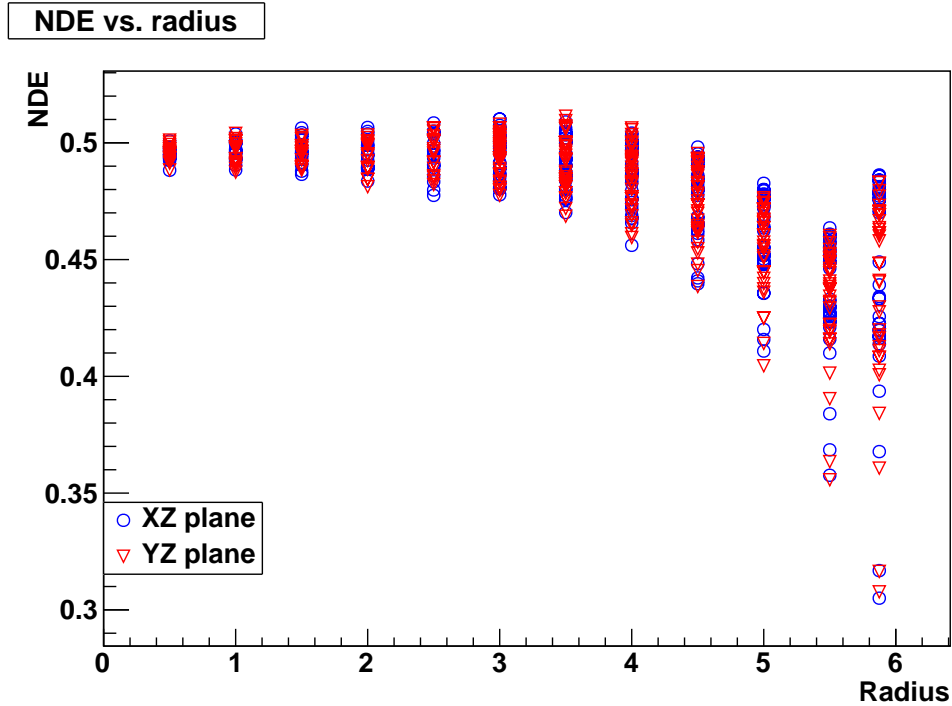


Figure 5.19: The corrected neutron detection efficiency as a function of radius. Each point represents a cell in the detector. NDE in the figure title and y-axis is short for neutron detection efficiency.

A weak asymmetry along the x or y direction is also observed. The neutron detection efficiency tends to be higher in the positive x and negative y hemispheres. This asymmetry can be evaluated quantitatively by calculating the fractional difference between the cell (x,y) and its reflection over the two axes. The distribution of these differences are shown in Fig. 5.20.

5.3. VOLUME-WEIGHTED NEUTRON DETECTION EFFICIENCY

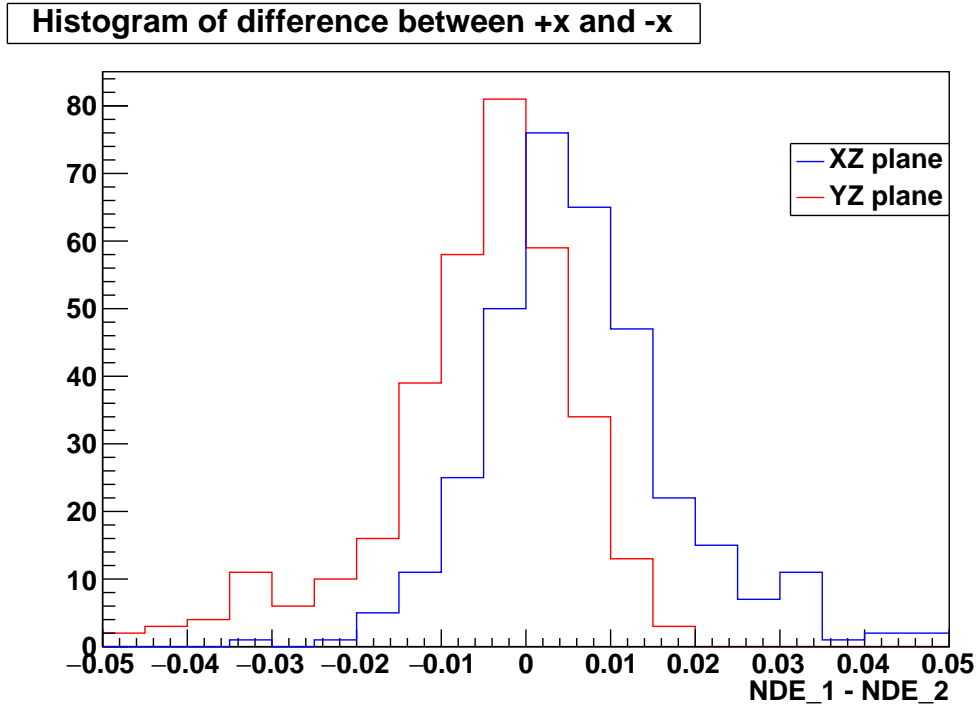


Figure 5.20: There exists a weak asymmetry along the x and y direction. The neutron detection efficiency tends to be higher in the positive x and negative y hemisphere. NDE_1-NDE_2 is the fractional difference between the cell (x,y) and its reflection over the two axes.

Fig. 5.21 and 5.22 displays the 2D neutron detection efficiency distributions over the radius and angle for XZ and YZ planes for complementary visualization. The lowest neutron detection efficiency in both planes appears near the neck to be 29.5%, where the highest neutron detection efficiency occurs close to the center as 51.5%. A global neutron detection efficiency can be extracted by calculating the volume-weighted average of neutron detection efficiency for all cells. Using the data on the XZ plane, the result is $(46.6 \pm 0.7)\%$ for the full detector volume and $(47.0 \pm 0.6)\%$ if applying a 5.5 m fiducial volume cut. For comparison, the YZ plane data give similar results: $(46.4 \pm 0.7)\%$ for full detector volume and $(46.7 \pm 0.7)\%$ with the cut.

5.3. VOLUME-WEIGHTED NEUTRON DETECTION EFFICIENCY 20

Averaging both planes to obtain the final results, $(46.5 \pm 0.5)\%$ ¹ for the full detector volume, turns out to be very close to that of the center, as given in Section 4.3.2.

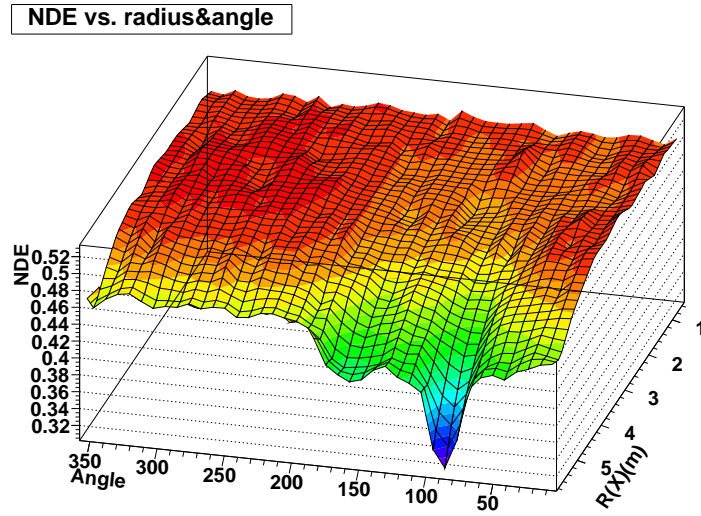


Figure 5.21: A 2D plot of the corrected neutron detection efficiency in radius and angle for XZ plane.

¹prior to systematic considerations

5.3. VOLUME-WEIGHTED NEUTRON DETECTION EFFICIENCY

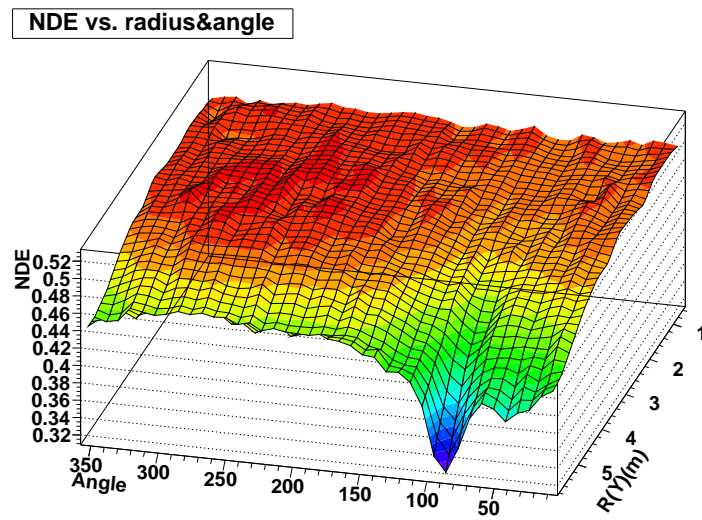


Figure 5.22: A 2D plot of the corrected neutron detection efficiency in radius and angle for YZ plane.

Chapter 6

Energy Calibration with The $^{241}\text{Am}^9\text{Be}$ Calibration Data

As briefly described in Section 2.3, energy calibration is an important part of the overall calibration program in SNO+. Two parameters of importance in energy calibration are the probability that one (or more) photoelectron is produced and detected when a photon strikes the PMT, referred to as the PMT quantum efficiency (see Section 2.2.2), and the collection efficiency which describes an overall relationship between an amount of energy deposited and the total number of detected photoelectrons. Defining the absolute energy scale of the detector, the energy calibration can be performed with a monoenergetic radioactive source. For the SNO+ water phase, the ^{16}N source is used as the primary energy calibration source [34]. One of the most important advantages of the ^{16}N source is the precise selection of source events, which is made possible by placing a scintillation chamber inside the source to tag the accompanying electrons.

However, energy calibrations using monoenergetic γ sources usually do not generate a fixed amount of light in the detector and therefore its reconstructed energy

distribution has a shape that is more complex than a simple Gaussian. γ s in the energy range of 2 to 10 MeV Compton scatter multiple times and create a few relativistic electrons that emit Cherenkov photons to be detected by the PMTs. Due to the Cherenkov threshold for each of the electrons, the total energy deposited in the detector by a γ can vary depending on the number of Compton electrons. The observed energy spectrum has a central value that is typically ~ 1.5 MeV lower than the γ energy, as deduced by comparison to Monte Carlo simulations.

Due to the intrinsic timing resolution of the PMTs (~ 1.5 ns), the multiple electrons created through Compton scattering can be not individually resolved by the detector, and the total deposited energy of all scattered electrons is measured as if it is from one electron. A shared unit, the number of total Cherenkov photons emitted by one event, can be used to relate the apparent electron energy spectrum of the γ s and that of monoenergetic electrons.

γ s emitted from the $^{241}\text{Am}^9\text{Be}$ source, of the energies 2.2 MeV and 4.4 MeV, can be potential additions to the ^{16}N energy calibration program. However, the energy spectrum of 2.2 MeV γ s bears huge uncertainties from the trigger efficiency curve at low nhits values, and little can be learned about the energy scale of the detector. The 4.4 MeV γ s, on the other hand, offers a second data point in the energy space that can be analyzed to check the energy linearity and verify the energy resolution measured by the ^{16}N source. Since the $^{241}\text{Am}^9\text{Be}$ source was only deployed in a handful of positions, the calibration is not integrated with the ^{16}N source but rather is analyzed to provide a cross-check. A global energy calibration strategy with various radioactive sources at different energies is being prepared for later phases of SNO+ [96], when accurate measurement of the energy scale non-linearity becomes essential for physics

6.1. ENERGY CALIBRATION USING A CENTRAL $^{241}\text{Am}^9\text{Be}$ RUN

analyses.

Compared with the ^{16}N calibration, the 4.4 MeV γ energy calibration has added complications in two aspects. Firstly, the selection method used to extract the source events does not produce a pure sample. In fact, the purity of selection is only $\sim 70\%$ if statistics are to be preserved. Contamination from backgrounds on the energy spectrum must then be carefully evaluated. Secondly, the prompt event selection has a nhits threshold of 15 due to the exponential increase of event rate at low nhits region and a practical limit on the CPU time from the data processing side even when events are selectively reconstructed. 4.4 MeV γ s that have lower nhits than 15 are effectively removed and need to be compensated for in the energy spectrum.

This chapter discusses the details of the energy calibration with the $^{241}\text{Am}^9\text{Be}$ source across the detector volume. Started first with calibration for one central run, the analysis extends to all interval $^{241}\text{Am}^9\text{Be}$ runs and the spatial variations are discussed.

6.1 Energy Calibration using a Central $^{241}\text{Am}^9\text{Be}$ Run

6.1.1 Event Processing and Selection

The event selection criteria for the 4.4 MeV γ energy calibration require a subtle balance between the size of the dataset and the purity of signal selection. Additional cuts are applied compared to the minimalistic analysis in Chapter 4 to increase the purity of the prompt candidates. The $^{241}\text{Am}^9\text{Be}$ dataset is processed with a specially designed coincidence processor where events are processed in two passes [97]. The coincidence processor actively selects coincidence pairs for reconstruction during data processing so that the processing power can be spent more efficiently. The first pass

6.1. ENERGY CALIBRATION USING A CENTRAL $^{241}\text{Am}^9\text{Be}$ RUN25

selects and reconstructs every event above 15 nhits, whereas the second pass processes every event that is within a 1 ms time window after a reconstructed event from the first pass. This time difference is chosen so that 99.5% of the source signals are preserved in the data.

Furthermore, events are selected with other additional cuts at the analysis level, which include:

1. valid reconstruction results for position, direction, and energy. This cut effectively applies an implicit nhits cut (15 for prompt events) and a time difference cut since the data processing does not reconstruct events outside of the selection region.
2. $-0.12 < \beta_{14} < 0.95$ and $\text{ITR} > 0.55$;
3. a maximum distance cut of 2.5 m between the prompt and delayed events;
4. a minimum nhits cut of 10 for the delayed events;

Since the size of the $^{241}\text{Am}^9\text{Be}$ source is quite small compared to the ^{16}N source, a proximity cut [98] that was used in the ^{16}N calibration to remove events that are too close to the source is not applied to the 4.4 MeV γ s. The shadowing effect from the $^{241}\text{Am}^9\text{Be}$ source is confirmed using MC to be negligible.

6.1.2 Cherenkov photon spectrum for the prompt γ s

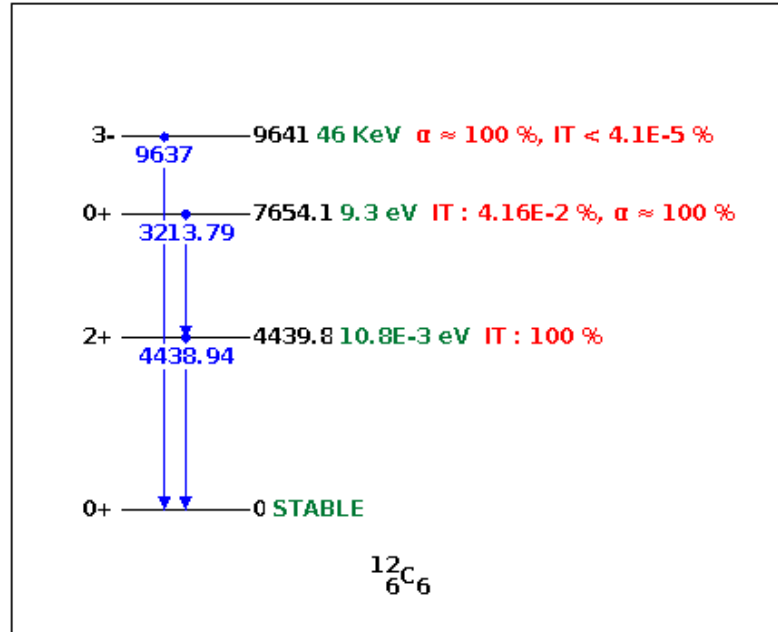


Figure 6.1: The level scheme of ^{12}C . In the context of the analyses presented in this thesis, the prompt γ can be treated as monoenergetic. Figure is from [80].

Monte Carlo simulation is generated to extract the prompt signal's Cherenkov photon distribution. As shown in the ^{12}C level scheme (Fig. 6.1), the prompt γ s' composition can be safely approximated to be purely 4.4 MeV in the context of the energy calibration. Therefore, 4.4 MeV γ s are simulated from within the $^{241}\text{Am}^9\text{Be}$ source at the center of the detector. The Cherenkov photon distribution is insensitive to the position of the source in the detector except when the source is placed next to the AV, where the 4.4 MeV γ or its Compton electrons can travel within the acrylic. As all internal $^{241}\text{Am}^9\text{Be}$ calibration runs are taken with the source at least 50 cm away from the AV, this effect is not considered further. Fig. 6.2 shows the obtained Cherenkov photon distribution. As discussed earlier, non-Gaussian features due to the multi-energy electron nature of the γ s on both sides of the spectrum are evident.

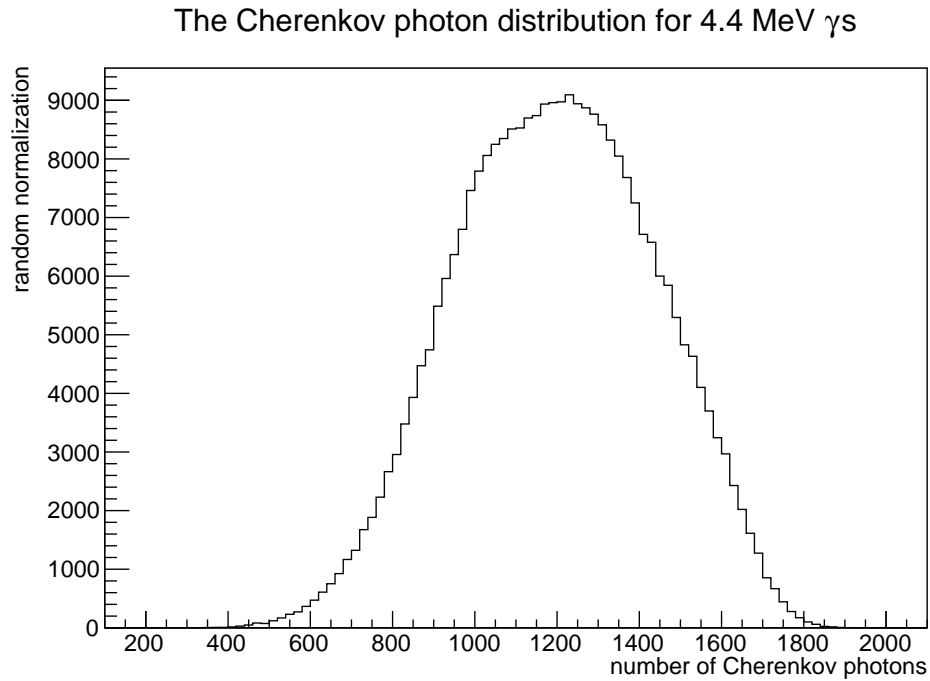


Figure 6.2: The distribution of number of Cherenkov photons produced by 4.4 MeV γ s.

6.1.3 Simulations of the Electrons

Similarly, monoenergetic electrons are simulated with a 0.05 MeV step size from 0.05 MeV to 8 MeV at the center of the detector. Fig. 6.3 shows an example of the Cherenkov photon distribution for 3.5 MeV electrons. As illustrated in Eqn. 2.4, the number of Cherenkov photons produced by an electron is proportional to the path length of the electrons.

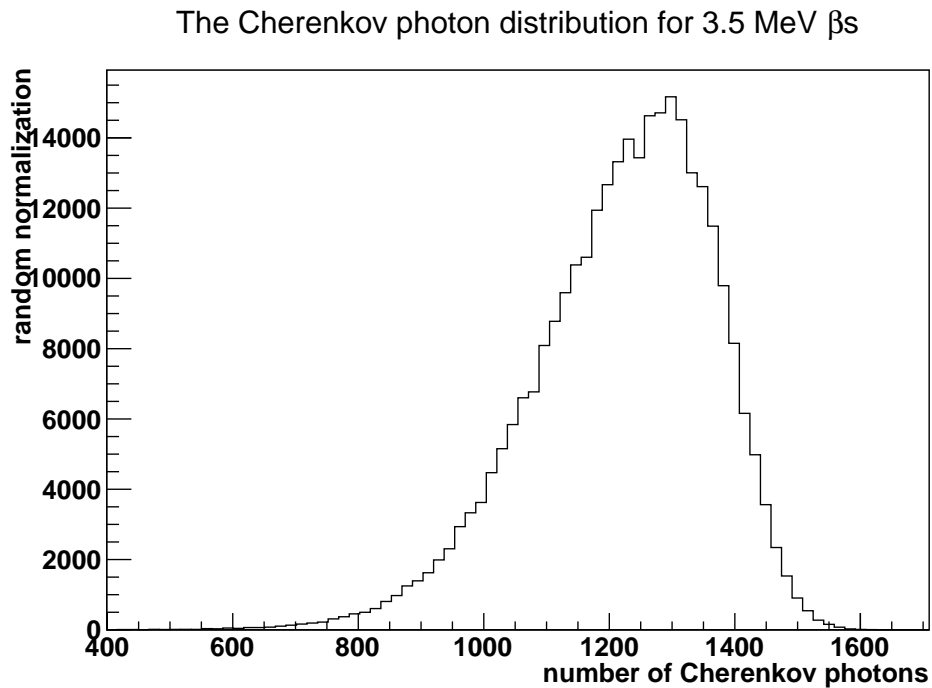


Figure 6.3: The distribution of number of Cherenkov photons produced for monoenergetic electrons of 3.5 MeV. The non-Gaussian shape is evident.

The Cherenkov photon spectra of different electron energies can be combined to produce a 2D plot (Fig. 6.4) that relates the number of Cherenkov photons of an event to its Monte Carlo energy. As expected, the two variables have a strong positive correlation. The y-axis slice of Fig. 6.4 shows the energy distribution of events with a fixed number of Cherenkov photons emitted. For example, events with 1000 Cherenkov photons could have an energy in the range from 2.4 to 6.5 MeV (note the logarithm scale).

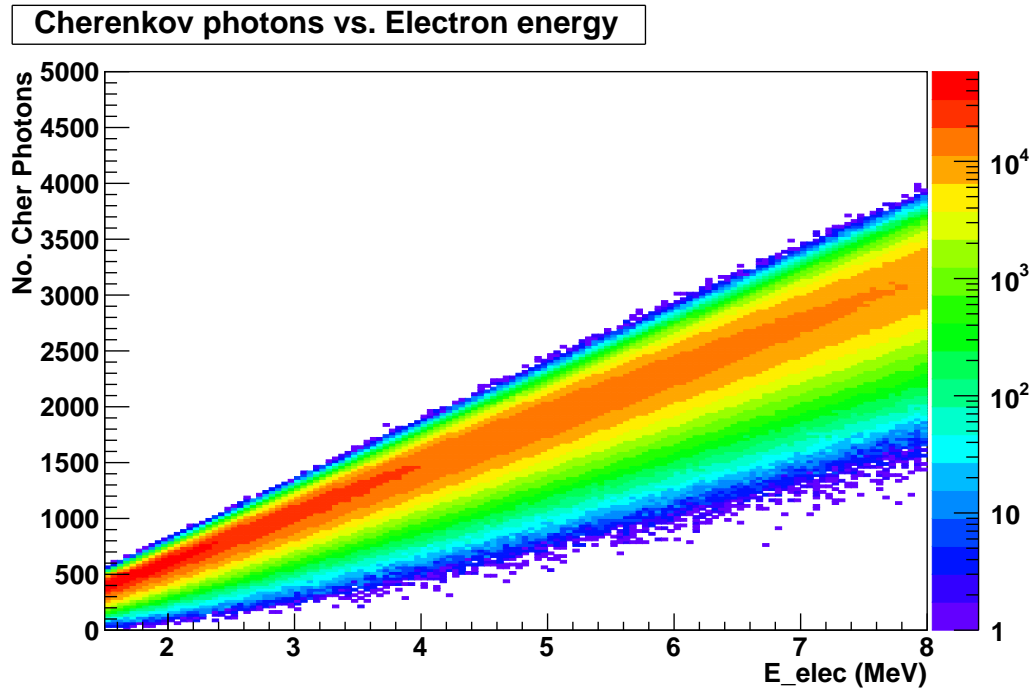


Figure 6.4: 2D histogram of number of Cherenkov photons and Monte Carlo event kinetic energy (E_{elec} in the x-axis). Individual plots such as Fig. 6.3 is in fact an x-axis slice of Fig. 6.4 at different energies.

6.1.4 The Electron Equivalent Energy Spectrum of the 4.4 MeV γ s

The number of Cherenkov photons of an event can then be used as the shared unit to relate the γ energy and energy as seen by the detector (electron energy). The electron equivalent energy spectrum of the 4.4 MeV γ s, shown in Fig. 6.5, is obtained by mapping the Cherenkov photon distribution of the 4.4 MeV γ s (Fig. 6.2) onto the 2D plot (Fig. 6.4). Random numbers are drawn from a probability density function same as the 4.4 MeV γ s Cherenkov photon distribution, and an energy is assigned according to the projected distribution Fig. 6.4 along the x-axis.

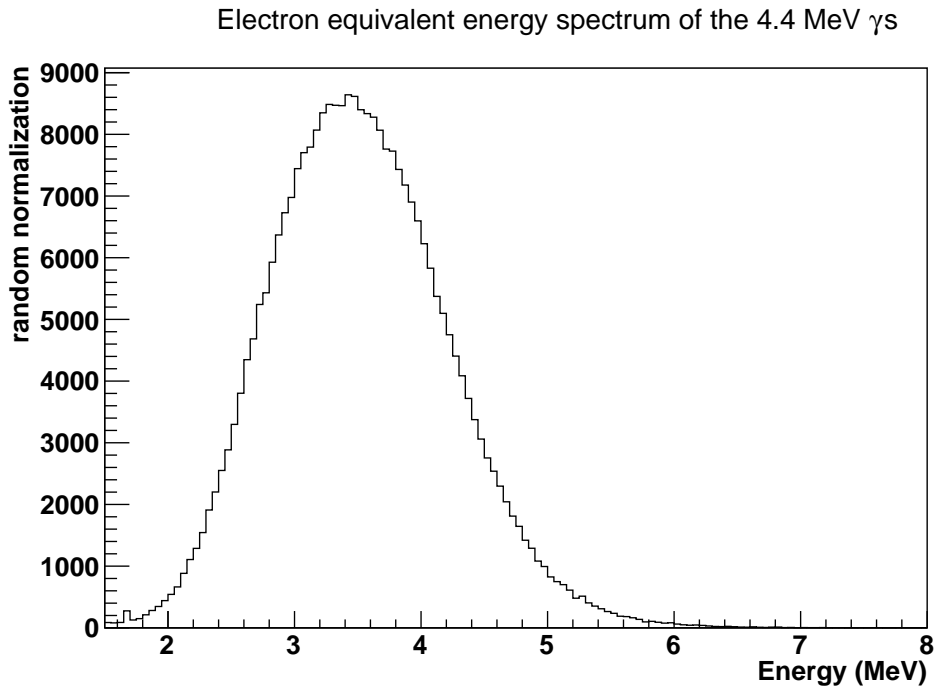


Figure 6.5: The electron equivalent energy spectrum of the 4.4 MeV γ s.

Embedded in Fig. 6.5 is the intrinsic energy resolution of the SNO+ detector for the 4.4 MeV γ s, if every Cherenkov photon produced is detected and the reconstruction is perfect. The spread in energy is due to the multi-electron nature of the Compton scattering of the γ s. This is used as the basis when comparing to the reconstructed energy distribution to gauge important parameters such as the energy scale and the energy resolution.

6.1.5 4.4 MeV γ s Reconstructed Energy Spectrum from Calibration

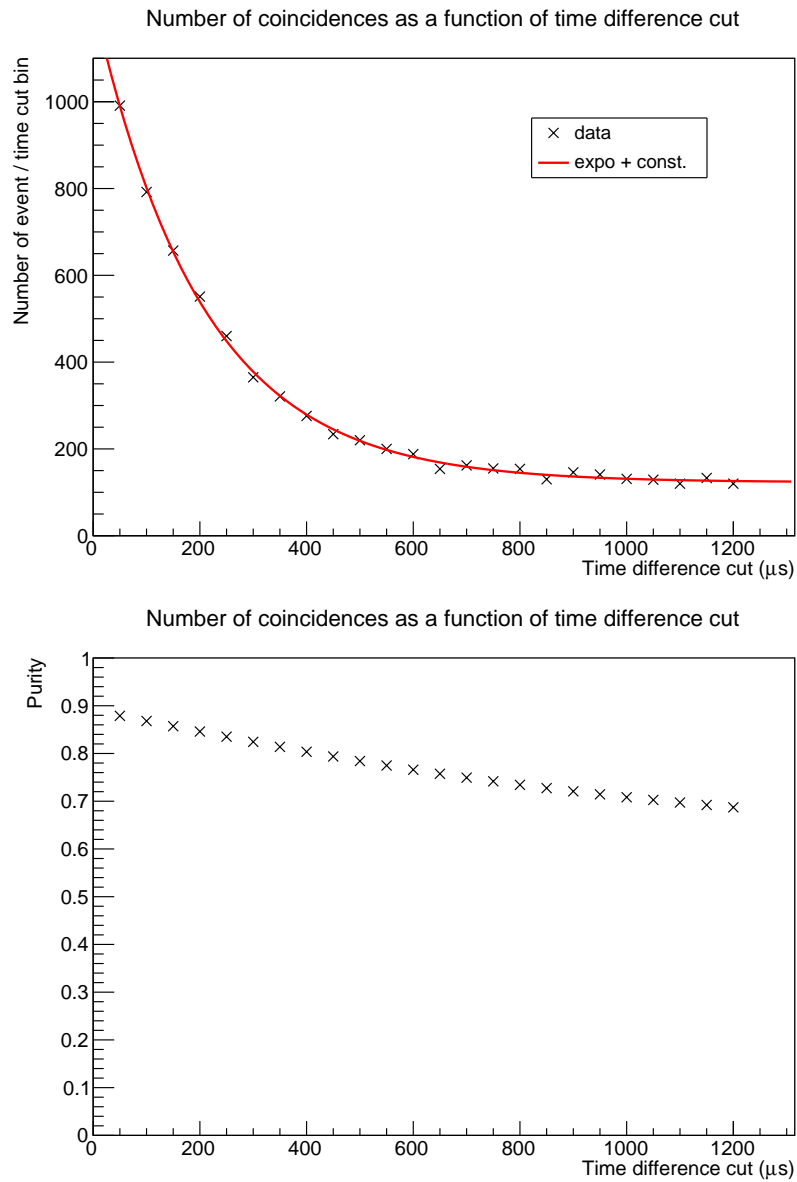


Figure 6.6: Top: number of coincidences as a function of time difference cut. The plot can be fitted with a sum of an exponential and a constant, corresponding to the $^{241}\text{Am}^9\text{Be}$ signals and backgrounds, respectively. Bottom: purity as a function of time difference cut.

The Background Energy Spectrum

The reconstructed energy spectrum of the 4.4 MeV γ s is derived by calculating the difference between that of the prompt events and backgrounds. Both the size (number of events) and the shape (spectrum) are needed for such calculations. The energy spectrum of the prompt events can be easily obtained from Section 6.1.1. Both the number and the energy spectrum of backgrounds need to be determined.

To determine the purity of the prompt selection, a series of time difference cuts with an incremental size of 50 μs are used to slice the data into portions. Fig. 6.6 shows the number of events as a function of the time difference cut. Above 800 μs the number of events per 50 μs becomes roughly a constant, indicating that there are few $^{241}\text{Am}^9\text{Be}$ coincidence events left. Fig. 6.6 can be fitted with a sum of an exponential and a constant (shown in red), corresponding to the $^{241}\text{Am}^9\text{Be}$ signals and backgrounds, respectively. The fitted capture time constant is found to be $(204.1 \pm 3.4) \mu\text{s}$, which is consistent with the result obtained from the minimalistic statistical analysis (Eqn. 4.11).

Therefore, the purity of the sample can be calculated by integrating individual parts of the fit function, which is also given in Fig. 6.6 as a function of the time difference cut. As expected, the purity drops as the time difference cut relaxes. With a $<1000 \mu\text{s}$ time cut, $\sim 70\%$ of the prompt events are the *True* 4.4 MeV γ s.

On the other hand, a data sample of pure backgrounds is selected to evaluate the shape of the background spectrum, by requiring the time difference of the candidates pairs to be bigger than 1000 μs . The source signal leakage with this time difference cut is less than 0.5%. Fig. 6.7 compares the distribution with a data sample selected with even more stringent cut ($>5000 \mu\text{s}$) and no significant deviation is observed.

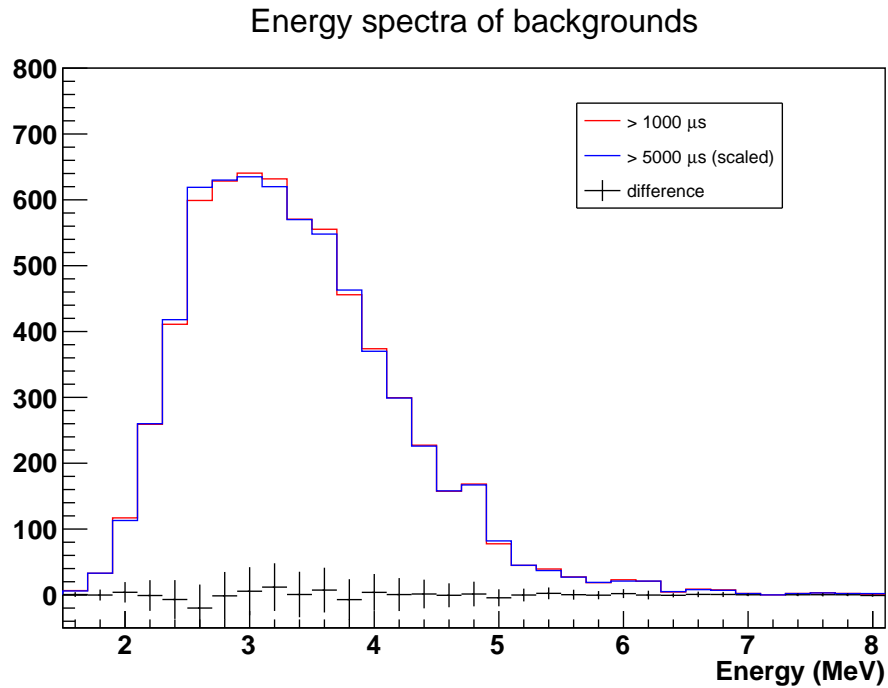


Figure 6.7: The background energy spectrum. The two spectra with different time cuts are shown to be identical with each other.

Nhits Correction Effect

The nhits correction effect arises from the nhits cut of 15 for the reconstruction of prompt events during data processing. 4.4 MeV γ s with fewer than 15 nhits that would have been reconstructed are removed by this cut.

To evaluate this effect, an assumption is made that the 4.4 MeV γ s and backgrounds with the same nhits values share similar reconstructed energy spectrum. A one hour $^{241}\text{Am}^9\text{Be}$ run was locally processed where every event with at least 10 nhits is reconstructed. Fig. 6.8 shows the energy spectrum for events with nhits=10, 12, and 14. These events mainly contribute to the low energy end of the spectrum - effects above 2.5 MeV are minimal.

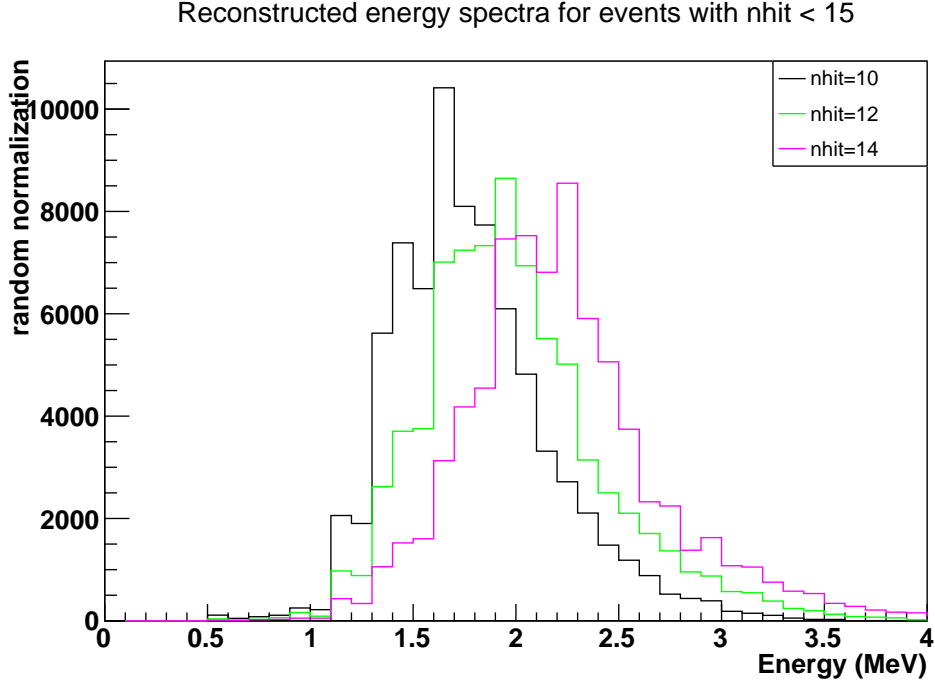


Figure 6.8: The reconstructed energy spectra for events with nhits values of 10, 12, and 14. These events tend to be reconstructed in the energy range from 1.5 MeV to 2.5 MeV.

The MC nhits spectra (Fig. 5.9) are used to predict the fraction of events that are lost due to the 15 nhits cut. Convolved with the energy spectrum for each nhit, the nhits effect correction is calculated and shown in red in Fig. 6.9.

The final reconstructed energy spectrum (Fig. 6.9) is calculated as a combination of individual spectra:

$$P(T_{\text{eff}}) = P_{\text{prompt}} - P_{\text{bg}} + P_{\text{nhit}}, \quad (6.1)$$

where P_{prompt} , P_{bg} and P_{nhit} are the energy spectra of the prompt candidates, the background portion in the prompt candidates, and the nhits effect correction, respectively.

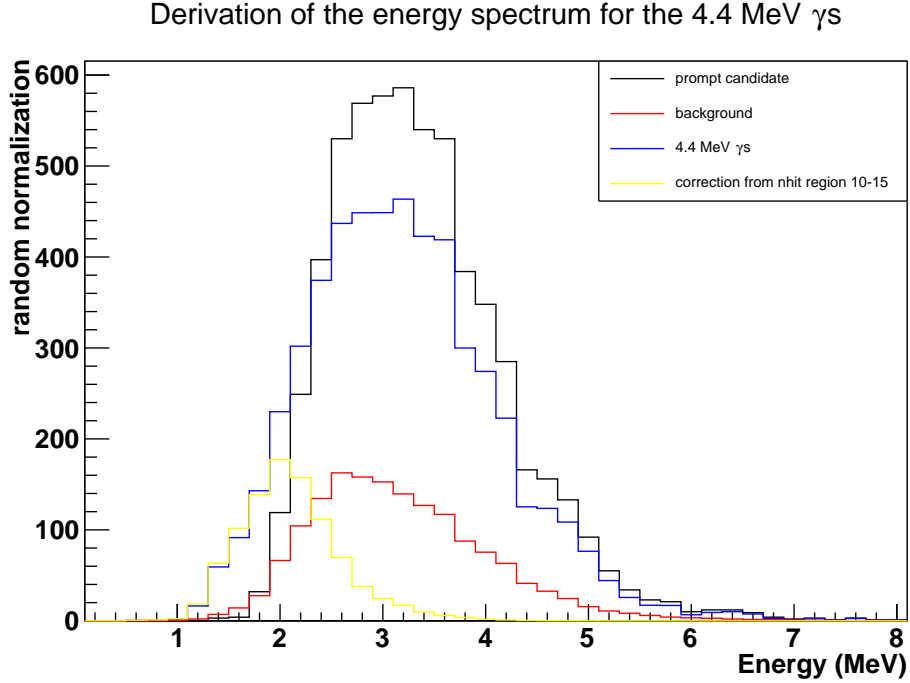


Figure 6.9: The reconstructed spectrum of the 4.4 MeV γ s (blue curve). It is derived by subtracting the background spectrum from the prompt . The purity of the selection is evaluated to be 72.9%.

6.1.6 Fit Results

The reconstructed energy spectrum of the 4.4 MeV γ s ($P(T_{\text{eff}})$) is fitted with the MC-derived apparent electron energy spectrum $P_{\text{source}}(T_e)$ convolved with a Gaussian, which represents the broadening in energy due to limited photon statistics (not all photons are detected) and detector mis-modeling (not perfect reconstruction). The fit function is shown in Eqn. 6.2 [98] [99]:

$$P(T_{\text{eff}}) = N \int P_{\text{source}}(T_e) \frac{1}{\sqrt{2\pi}\sigma} e^{-\frac{((1 + \delta_E)T_{\text{eff}} - T_e)^2}{2\sigma^2}} dT_e, \quad (6.2)$$

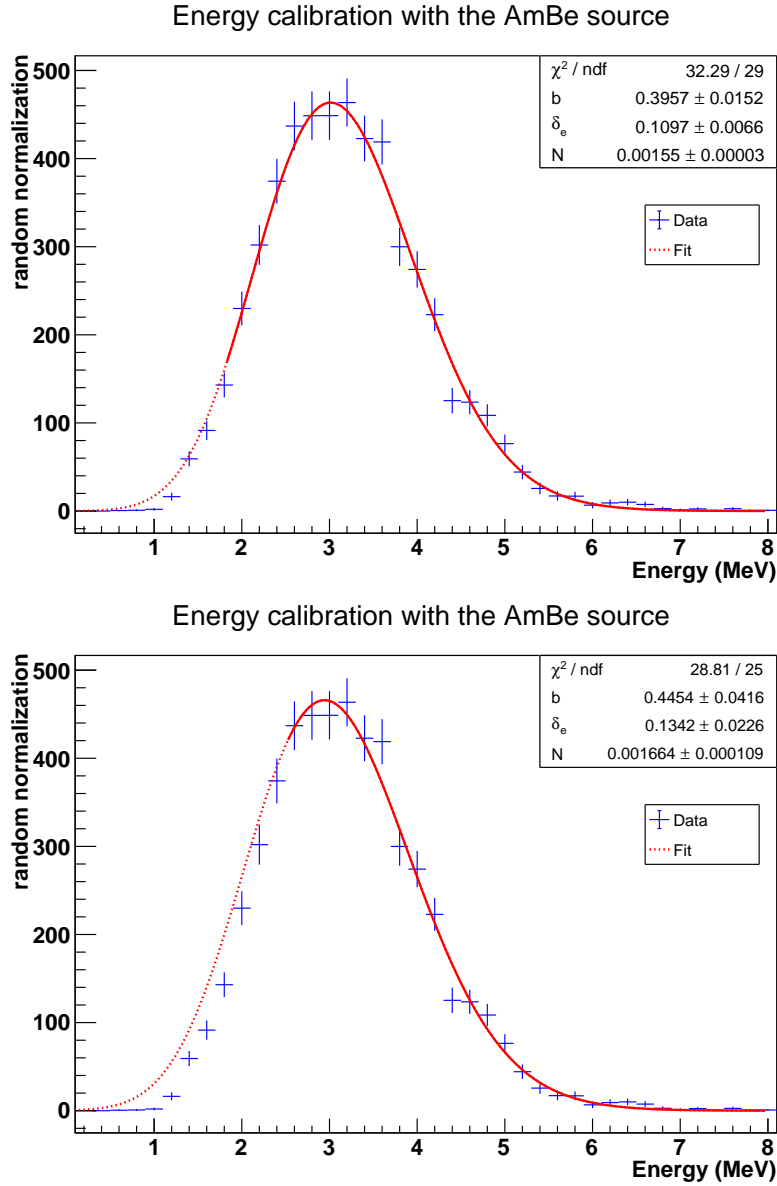


Figure 6.10: Fitted energy spectrum for 4.4 MeV γ s for a central $^{241}\text{Am}^9\text{Be}$ run. Two different fit regions ([1.8, 8.0] MeV and [2.5, 8.0] MeV) are shown.

where δ_E is the relative energy scale that represents an offset in the energy scale. σ is the detector-only energy resolution, excluding effects from the intrinsic Cherenkov photon distribution. σ has an energy dependence term that is proportional to the

6.1. ENERGY CALIBRATION USING A CENTRAL $^{241}\text{Am}^9\text{Be}$ RUN 37

square root of E :

$$\sigma(E) = b\sqrt{E} + c, \quad (6.3)$$

where b and c are parameters to be fitted. Since the detector resolution is dominated by the light collection at the PMT level, the constant term c is fixed to 0 for the robustness of the fit.

Fig. 6.10 shows the fit results of a central $^{241}\text{Am}^9\text{Be}$ run. The fit was performed on two different ranges, [1.8, 8.0] MeV and [2.5, 8.0] MeV, to show the size of possible systematic effects at the low-end tail from trigger efficiency and the nhits effect correction. 1.8 MeV is the lowest energy that the detector operates at with 100% trigger efficiency [43] (estimated with 1σ uncertainty) and 2.5 MeV is where the energy reconstruction begins to diverge in mean energy [99]. Both fits are in general agreement with the reconstructed energy spectrum. The fit at [1.8, 8.0] MeV returns lower values of both b and δ_E , but is consistent with [2.5, 8.0] MeV if taken into account the statistical errors.

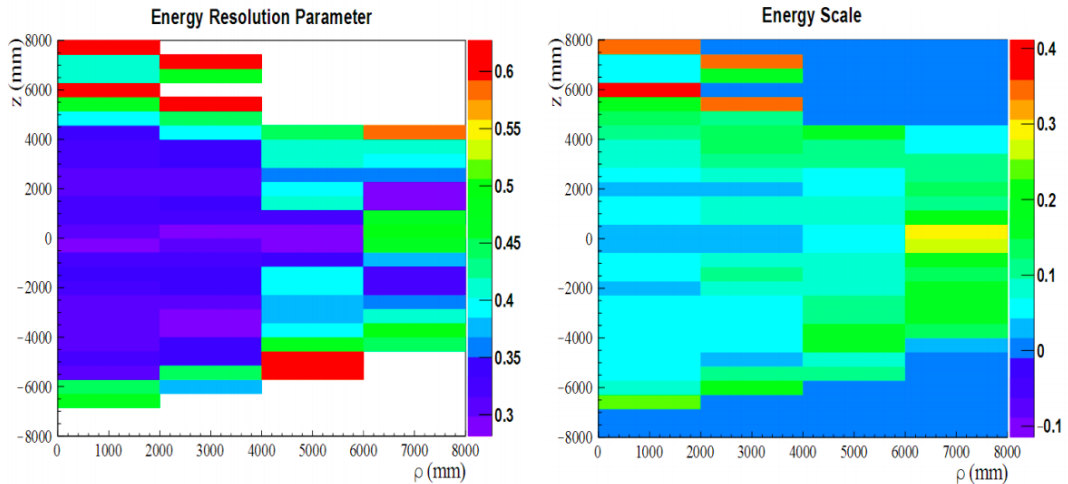


Figure 6.11: The energy resolution and scale across the detector, as measured using an ^{16}N source. ρ is the radius the on x-y plane. Figure is from [99].

For reference, the ^{16}N calibration (Fig. 6.11) estimated $b = 0.3$ and $\delta_E = 0.03$ at the center of the detector [99].

6.2 Spatial Variation of the Energy Scale and Energy Resolution

Fig. 6.12 and Fig. 6.13 show the distribution of the energy scale and resolution as a function of radial position, with two different fit regions. Two data points for the fit region [1.8, 8.0] MeV failed to obtain a valid fit and are removed from the figures.

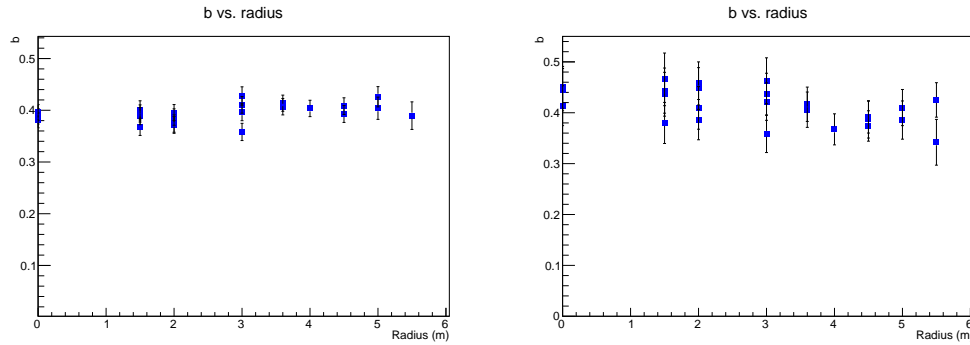


Figure 6.12: The energy resolution as a function of radial position. Left: [1.8, 8.0] MeV; Right: [2.5, 8.0] MeV.

The energy resolution remains flat across the detector, which is also observed in the ^{16}N calibrations. However, $^{241}\text{Am}^9\text{Be}$ consistently measures a higher b value than ^{16}N , indicating that the detector resolution deteriorates faster than photon statistics predict. A $\sim 10\%$ increase of b close to the neck is also not observed in the 4.4 MeV γ calibration.

The absolute value of the relative energy scale offset shows better agreement between $^{241}\text{Am}^9\text{Be}$ and ^{16}N . However, the $^{241}\text{Am}^9\text{Be}$ energy calibration measures a weaker, but contradictory trend compared to the ^{16}N . Independent of the fit region variation, δ_E steadily decreases from ~ 0.13 as the source moves outwards. Above 5 m

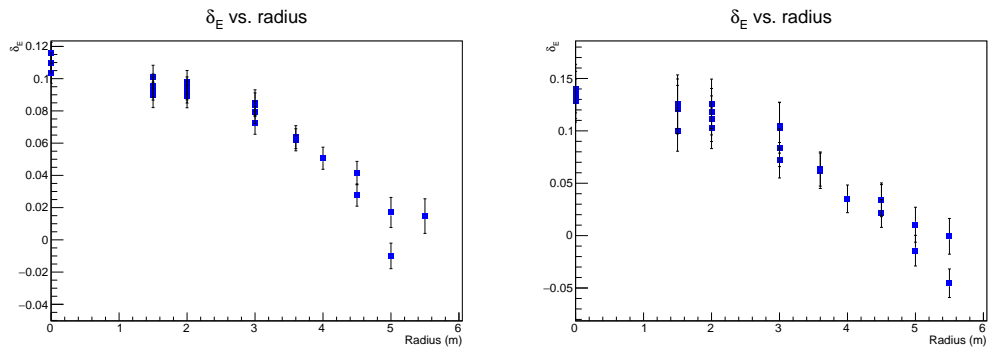


Figure 6.13: The energy scale as a function of radial position. Left: [1.8, 8.0] MeV; right: [2.5, 8.0] MeV.

from the offset becomes negative.

Chapter 7

Searching for Reactor Antineutrinos in Water

Antineutrinos emitted from nearby nuclear reactors sometimes leave a mark in the SNO+ detector through the IBD reaction (Eqn. 1.1), of which the unique coincidence signature can be captured in the data. Different from the $^{241}\text{Am}^9\text{Be}$ signals, the prompt event of the IBD reaction is an energetic positron, generating Cherenkov radiations itself while traversing the detector. In the end the positron will be annihilated with an electron, emitting two γ s with the energy of its rest mass (511 keV) that is only just above the Cherenkov threshold (257 keV, kinetic energy). The photon contribution from the annihilation process is very limited as energetic electrons above the Cherenkov thresholds need to be produced from Compton scattering. Calculations based on the reactor antineutrino flux and IBD cross-section show that ~ 115 [24] antineutrino events per year are expected to occur within the SNO+ detector. However, the number of antineutrino events that are expected to both trigger the detector and therefore form a coincidence shrinks sharply for the water phase, as the neutron detection efficiency is only $\sim 50\%$ and the e^+ signals inherit an energy spectrum similar to that of the incoming antineutrinos (see Fig. 1.1). The counting further worsens as more stringent selection criteria are applied to reduce accidental

backgrounds.

Searching for reactor antineutrinos in the SNO+ water phase has always been an interesting potential physics topic for the experiment. Several feasibility studies [24] [100] [101] [102] [103] (some before the deployment of the $^{241}\text{Am}^9\text{Be}$ source!) were carried out to evaluate the possibility, yet the results have been suboptimal. The combination of the low energy nature of the signal, relatively high background levels of the detector in the water phase due to higher amounts of radon, and the handful number of events expected in a reasonable timeframe pose major challenges to the search. With a one year dataset and depending on the signal selection techniques and background levels, modest estimates predict 1 to 5 antineutrino events per year will be observed with backgrounds on the same order of magnitude. Unless improvements are made either from hardware side (e.g. lower radon levels in the water, better energy and position resolution) or software (better reconstruction, more efficient signal extraction), the discovery potential of such analysis and the probability to produce an informative result is dim.

Instead of another feasibility study, this chapter takes the available water data that was primarily processed for the nucleon decay search and performs a hypothesis test. An extended binned maximum likelihood analysis is presented to derive an upper limit of signal events observed in the dataset and reactor antineutrino flux.

7.1 Dataset

The SNO+ detector started collecting water data from May 5th, 2017 and the first data-taking period lasted until December 25, 2017. This 235-day dataset [104] was processed and analyzed to produce physics results on a search for nucleon decay [34]

and measurement of the ^8B solar neutrinos flux [35].

7.1.1 Run Selection and Live Time

During this time period, the detector was configured to run in physics mode approximately 78.9% of the time. Each physics run (~ 1 hour) was passed through a semi-automated run selection framework where it is scrutinized with a series of run-level data quality checks. These checks make use of a wide range of detector monitoring tools, and include high-level and low-level criteria. The high-level data quality criteria checks for PMT coverage, run type, event rate, and clock synchronization, whereas the low-level data quality checks include run duration, PMT high voltage status, and slow control. Additionally checks also take into account the detector state, PMT occupancy, muon rate, and shift report. As shown in Fig. 7.1, about 29.3% of the physics data was discarded by run selection. Data cleaning further reduces the dataset size by 2.4% [73]. The final analyzed dataset has a live time of 114.7 days with an uncertainty of 0.04% [34].

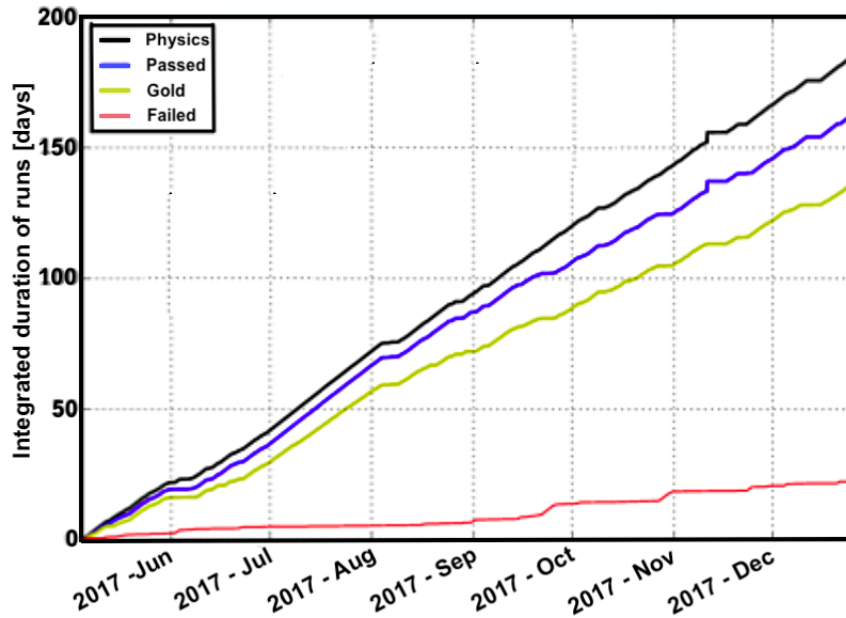


Figure 7.1: The fraction of good data for physics analyses (labelled with "Gold") as a function of time. Figure is from [105].

7.1.2 Detector Event Rate

This analysis utilizes the readily available dataset that was processed with RAT-6.5.0 to 6.5.4. The event reconstruction is calibrated with an ^{16}N source deployment in November 2017. A soft nhits cut of 15 is applied as the processing threshold to reduce the size of data (below 15 nhits only 10% of the events are processed and reconstructed).

The overall detector rate over this period experienced some systematic variations. Shown in Fig. 7.2 is the number of events per hour as a function of the time since the start of data-taking. Artificial drops along the rate curve originate from the fact that some runs are sporadically removed by run selection.

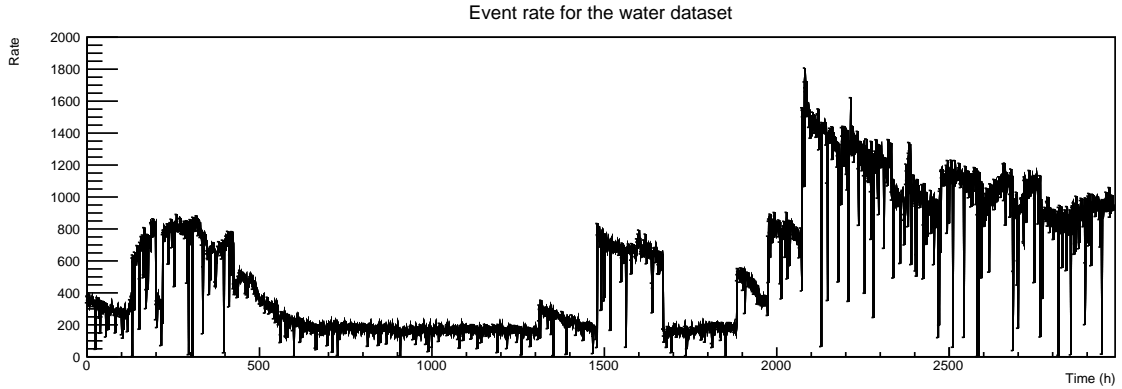


Figure 7.2: Detector event rate plotted in continuous hours. The event rate are plotted after applying a set of loose cut including fit validity, β_{14} , ITR, and $\mathbf{u}\cdot\mathbf{R}$.¹

The commissioning and operations of detector subsystems (e.g. the water recirculation plant and the calibration system) impacted the detector event rate. Other common causes for significant changes in the event rate include regular maintenance of PMTs and the trigger system, and background assays. In general, the detector rate remained at fairly low levels for the first 2000 hours, where a significant rate jump occurred around September 28th, 2017. This increase in event rate coincided with a couple of operations taking place at the same time, including a disruptive AV recirculation which potentially brought in Rn into the AV, some calibration work on the top of the neck to install the side rope box, and electronic work to replace a crate trigger card. The rate decreased almost exponentially after the surge, and back to the previous level in about two weeks, indicating that the spike was most likely caused by an introduction of Radon.

¹A positive $\mathbf{u}\cdot\mathbf{R}$ value selects outward-going events, which are less likely to be coming from external regions where background level is high. \mathbf{u} is the normalized direction vector of the event and \mathbf{R} is the normalized reconstructed vertex.

7.1.3 Trigger Thresholds

Additionally, there was a dramatic change in trigger thresholds and efficiencies on September 1st, 2017, resulting in a persistent event rate bump near the 1978th hour in Fig. 7.2. The primary nhits trigger threshold was lowered from 15 to 7 in an attempt to be more sensitive to low energy events, especially reactor antineutrinos. The energy threshold corresponding to 100% trigger efficiency dropped from 4.1 MeV to 1.8 MeV [43].

The detector continued to take more water data after the first time period, collecting events at similar rates after the trigger threshold change. As the cover gas system came online in September 2018, the background level started to drop by a factor of ~ 5 following Rn's half-life. In October 2018, less than a tonne of LAB was added to the neck, corresponding to a LAB-water interface level about 1.5 m above the PSUP. Filling of LAB was soon suspended until May 2019. This time period, summing to approximately 120 days of detector live time, enjoys a much-improved background level that is suitable for a more dedicated reactor antineutrino search. However, these data will not be included in this analysis as they were put under a data blindness scheme and were not processed at the time of writing.

7.2 Selection Algorithm for Antineutrino Candidates

Among a list of observables from the dataset, the time difference and distance between prompt and delayed candidates speak the most about the events' probability of being an antineutrino pair. Other variables such as β_{14} , ITR, and the energy/nhits spectra of prompt and delayed candidates, provide little to no information on the event identity, especially when the data-MC comparison over these variables reveals

substantial differences. Therefore, only time difference and distance are used to select antineutrino candidates.

The dataset was prescreened with a set of loose global cuts that is used to produce Fig. 7.2 and 7.3:

1. valid reconstruction results for position, direction, and energy.
2. a positive $\mathbf{u} \cdot \mathbf{R}$ value if an event is more than 3 m away from the detector center.

This further removes backgrounds from external region.

3. $-0.12 < \beta_{14} < 0.95$ and $\text{ITR} > 0.55$;

To select coincidence pairs, a two-pass algorithm is adopted. The first pass evaluates each event from the dataset to determine whether it can be a prompt or delayed candidate. Selection criteria for both candidates include low bounds for energy and nhits, but the delayed candidate cuts have an additional maximum nhits cut of 25. It is possible that an event can be labeled with both types.

The second pass then looks to pair the prompt and delayed candidates. For each prompt candidate, the events following it will be checked to see if it has a delayed label. The loop will continue until a delayed candidate is found or the maximum allowed time difference is reached. The pairs are then output to a new file together with their time and position difference calculated. The selection algorithm permits the scenario where backgrounds can get in between the positron and neutron signals but the probability of it occurring is negligible given the low background rates (Fig. 7.3). It also allows an event to be the prompt candidate for one pair and delayed candidate for another pair.

As shown in Table 7.1 the cuts applied in the selection algorithm are made as

	Global cuts							Individual cuts			Coincidence cuts	
	Trigger word	Data cleaning	Fit validity	Fiducial volume	u.R	β_{14}	ITR	Energy (MeV)	nhits	nhits max	Time difference	Distance
Prompt	SNO+	SNO+	True	5.3 m	>0	>-0.12	>0.55	2.5	0	N/A	N/A	N/A
Delayed	standard	standard				&&<0.95		1.0	10	25		

Table 7.1: Summary of selection criteria in sequential order for the water dataset. Even though the nominal energy and nhits cuts for the delayed candidates are 1.0 MeV and 10 nhits, due to the processing threshold the effective thresholds are substantially higher. No time difference and distance cuts are applied.

inclusive as possible. In total 145801 coincidence pairs are found, of which most, if not all, will be accidental backgrounds.

7.3 Background Characteristics

Coincidence pairs that passed the selection algorithm can be used to evaluate the background characteristics, including time difference and distance distributions. To eliminate possible signal events from the coincidence pairs when evaluating backgrounds, coincidence pairs with a time difference smaller than 1 ms are removed from the dataset to perform a sideband estimation.

7.3.1 Time difference distribution

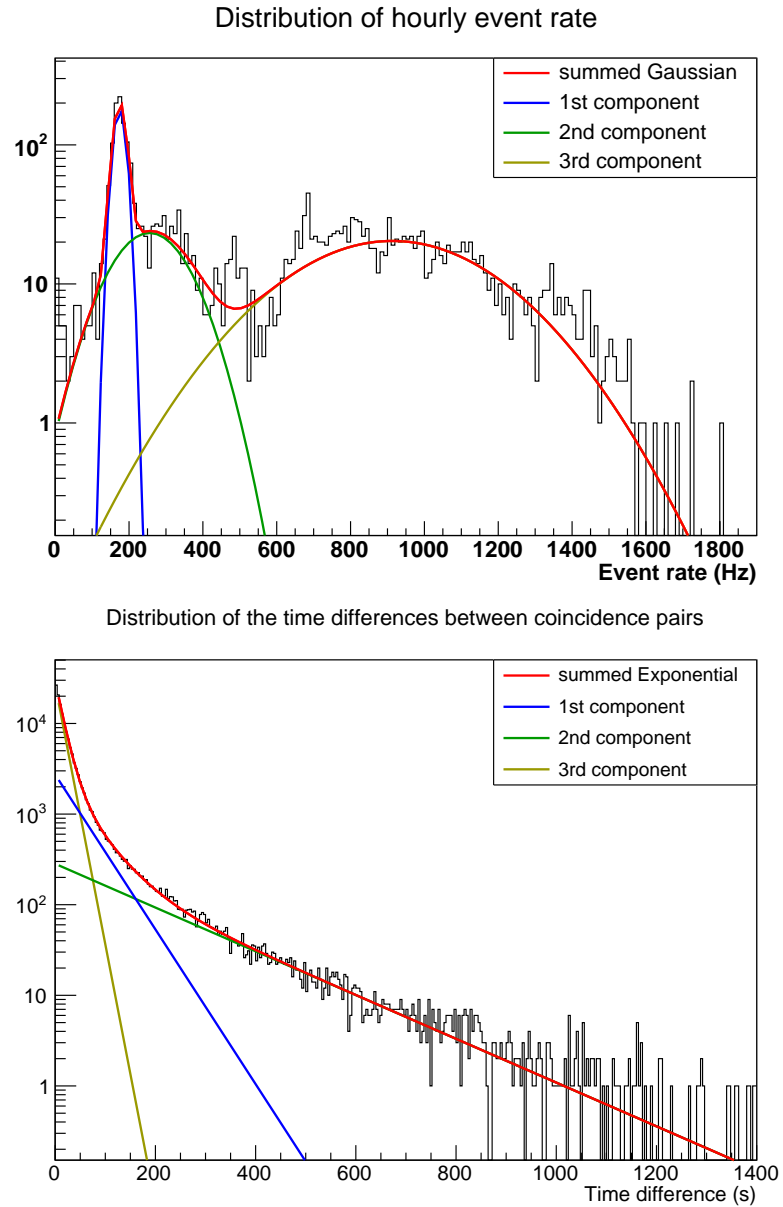


Figure 7.3: Top: event rate distribution fitted with three independent Gaussians; Bottom: distribution of time difference of coincidence pairs, fitted with three independent exponentials.

Fig. 7.3 shows the distribution of the detector event rate for the whole dataset. The sum of three independent Gaussian distributions is also fitted to the distribution. The three Gaussian means (174 Hz, 256 Hz, and 913 Hz, respectively) correspond to the three event rates that the detector spent most of the time operating with.

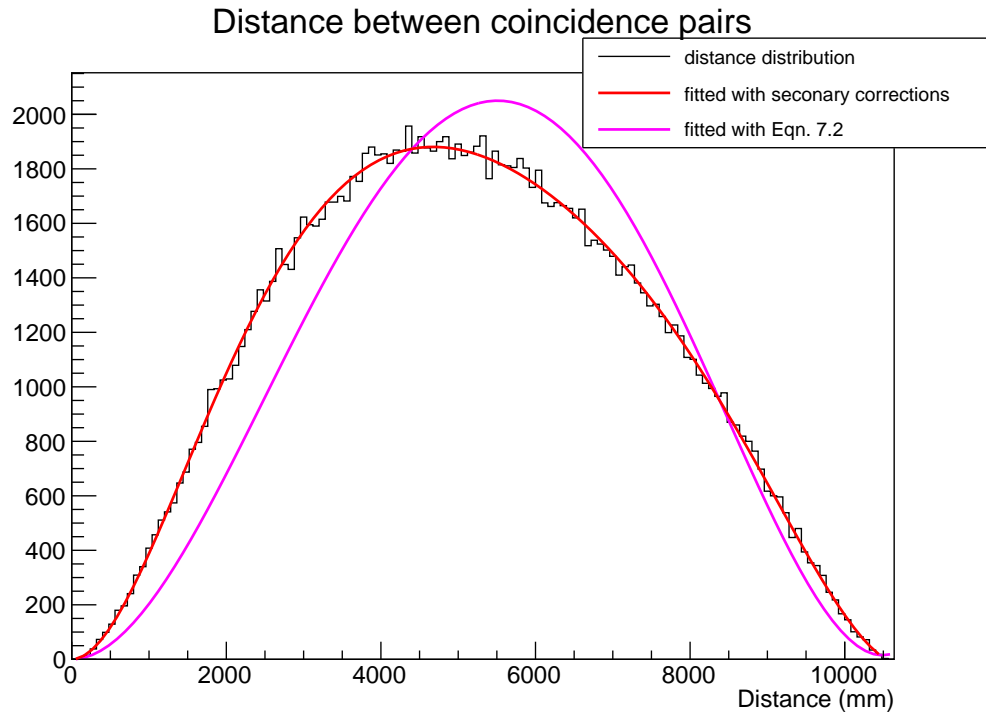


Figure 7.4: Distances between coincidence pairs. The distribution can be fitted with an analytical function describing distance between random points within a ball. Higher order corrections can significantly improve the goodness of fit.

Accordingly, the time difference distribution between coincidence pairs, also shown in Fig. 7.3, is fitted with the sum of three exponentials. As is with a Poisson process, different event rates give rise to different exponential constants in time difference distributions. In our case, the exponentials are not directly related to the Gaussian means as more cuts are applied before making the time difference distribution. The

fitted exponential time constants are 15.1 s, 50.9 s, and 179.9 s respectively.

7.3.2 Distance distribution

The distribution of distances between randomly distributed points within a spherical ball of radius R is described by a polynomial [106]:

$$F(r) = \frac{3r^2}{R^3} - \frac{9r^3}{R^4} + \frac{3r^5}{16R^6}, \quad (7.1)$$

Fig. 7.4 shows the distance distribution between coincidence pairs, and the purple curve represents a fit using Eqn. 7.1 with the coefficients of the polynomial left free in the fit. The less-than-ideal goodness of fit originates from the fact that backgrounds in the detector are not uniformly distributed. Fig. 7.5 shows the event position distribution along the three axes, where significant distortions in z-positions are observed. Backgrounds are mostly clustered in two regions: the $z > +4$ m region which results from sustained feeding of Rn contamination due to the absence of a cover gas system on top of the neck; and the $z = -4$ m bump which originates from periodical AV water recirculation, where Rn, possibly carried by air bubbles, was injected through the pipes.

In light of Fig. 7.5, higher order corrections are applied to Eqn. 7.1 to account for the background non-uniformity. The red curve in Fig. 7.4 shows an improved fit with the addition of r^4 and r^6 terms.

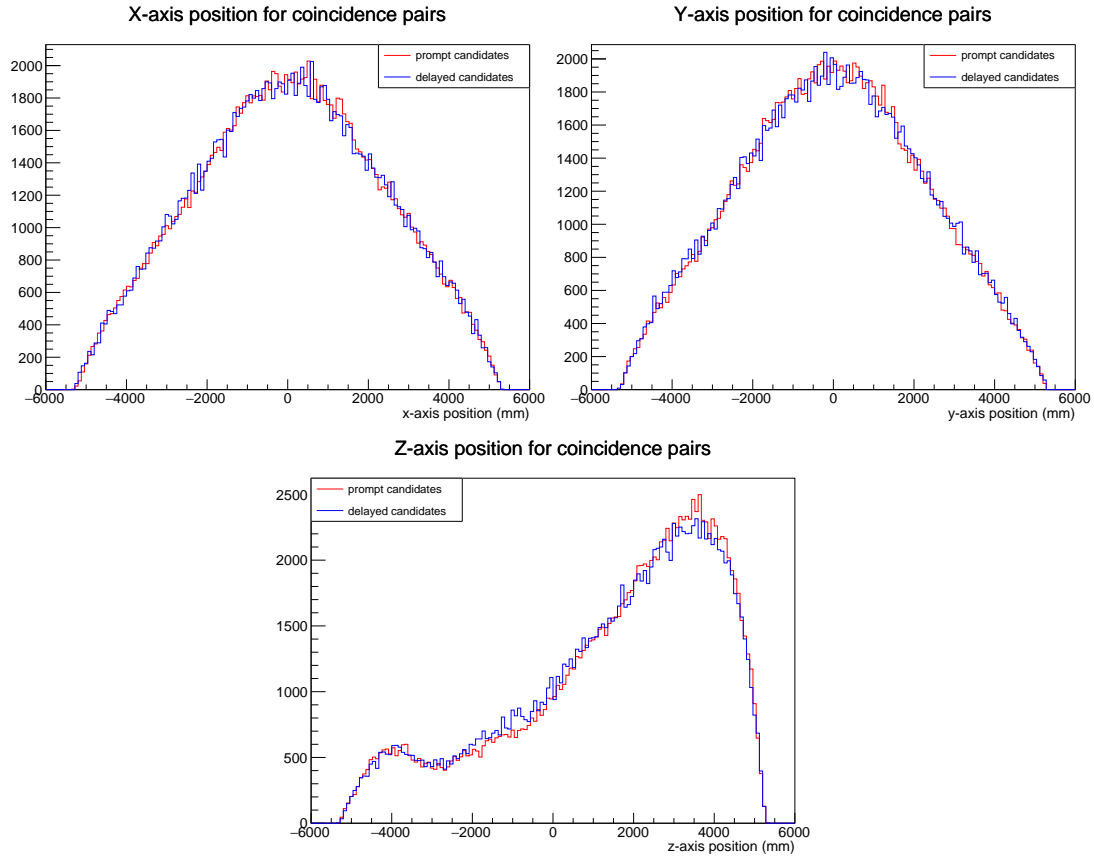


Figure 7.5: Position distributions along the x-, y-, z-axis. The z-axis shows significant distortion.

7.4 Signal Characteristics

Signal characteristics in time difference and distance are evaluated with run-by-run reactor antineutrino Monte Carlo, where the signals are configured to be uniformly distributed within the detector. Same selection algorithm (Section 7.2) is adopted to process the antineutrino MC. As there are no coincidence cuts applied to the dataset, coincidence pairs can be mistakenly selected even for antineutrino MC and create a long tail in time difference distribution of around 30 s, characterized by the signal rate. Most of these mis-selected coincidence pairs are due to untriggered neutrons in the

MC. To extract the antineutrino signals, a time difference cut of 2 ms is additionally applied to the candidate pairs.

Fig. 7.6 shows the time difference and distance distributions of the antineutrino events from Monte Carlo. The time distribution can be fitted with a simple exponential and yields a time constant of $(200.45 \pm 0.18) \mu\text{s}$. The signal distance distribution peaks at around 0.7 m, with few outliers reaching beyond 2 m.

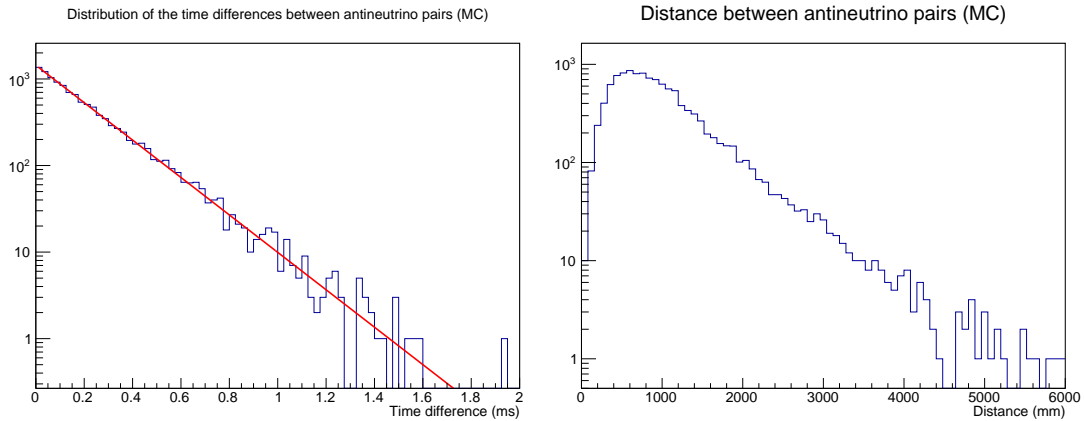


Figure 7.6: Distribution of time difference and distance of antineutrino pairs.

7.5 Hypothesis Testing

A hypothesis test is conducted under the assumption that all backgrounds are accidental:

H_0 : There is no reactor antineutrino event in the dataset;

H_1 : There are reactor antineutrino events in the dataset.

A quantity that combines the time difference and distance information and properties is designed for a maximum likelihood analysis, which is proven to yield similar results as a 2D likelihood analysis performed on the two observables. \mathbf{p} is defined as

the common logarithm of the product of the cumulative probabilities of time difference and distance distributions:

$$\begin{aligned} \mathbf{p} &= c.d.f._T(t) \cdot c.d.f._L(l), \\ &= \int_0^t p.d.f._T(t) dt \cdot \int_0^l p.d.f._L(l) dl, \end{aligned} \quad (7.2)$$

where t and l are the time difference and distance of a coincidence pair, respectively. $p.d.f._T(t)$ and $p.d.f._L(l)$ are the probability density functions of time difference and distance for backgrounds, as given in the analytical fit functions shown in Fig. 7.3 and Fig. 7.4.

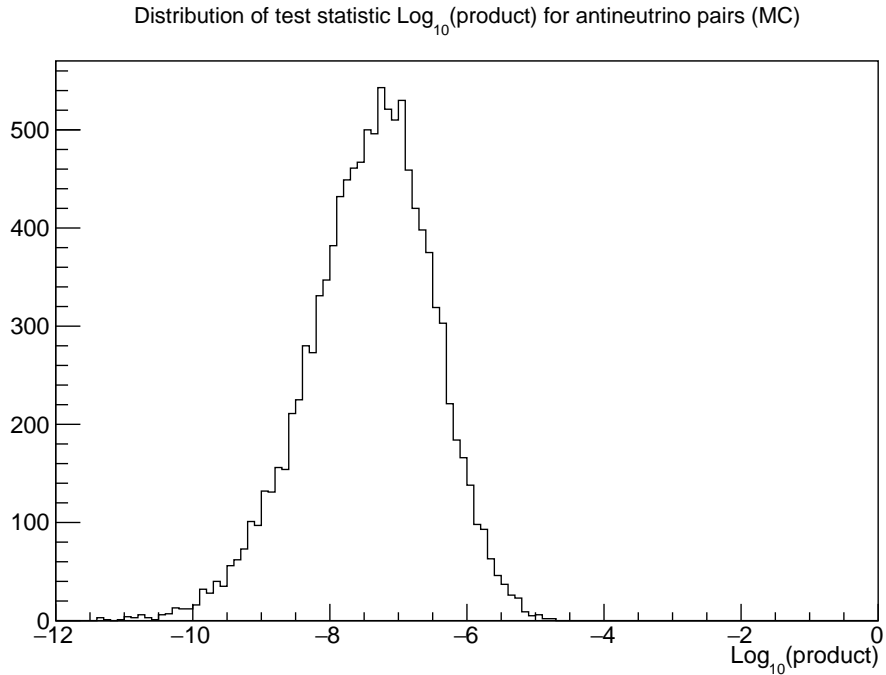


Figure 7.7: The product of the cumulative probability of the time difference and distance distributions for the antineutrino pairs.

\mathbf{p} can be calculated for each MC antineutrino event using Eqn. 7.2 and the resulting

distribution is given in Fig. 7.7. On the other hand, background \mathbf{p} values have a distribution identical to that of the common logarithm of the product of two variables uniformly distributed in $[0,1]$. This is given by:

$$p.d.f.\cdot_{\mathbf{p},bg}(\mathbf{p}) = -\mathbf{p} \cdot 10^{\mathbf{p}}. \quad (7.3)$$

An extended binned maximum likelihood fit is performed in each bin of the \mathbf{p} distribution, fitting for the number of signals and backgrounds. The \mathbf{p} distribution of the signal is converted to a histogram with same number of bin as Fig. 7.7. The resulting likelihood function is given by:

$$\begin{aligned} L(\mathbf{p}; s, b) &= \prod_{i=1}^M \text{Pois}(N_i; s_i + b_i) \prod_{j=1}^{N_i} \left(\frac{s}{s+b} \mathbf{p}_{s,i} + \frac{b}{s+b} \mathbf{p}_{b,i} \right), \\ &= \prod_{i=1}^M \frac{(s\mathbf{p}_{s,i} + b\mathbf{p}_{b,i}) e^{-(s_i+b_i)}}{N_i!}, \end{aligned} \quad (7.4)$$

where s and b are the numbers of antineutrino signals and backgrounds. M is the number of bins (120) of the \mathbf{p} distribution and N_i is the number of observed events in a given bin i .

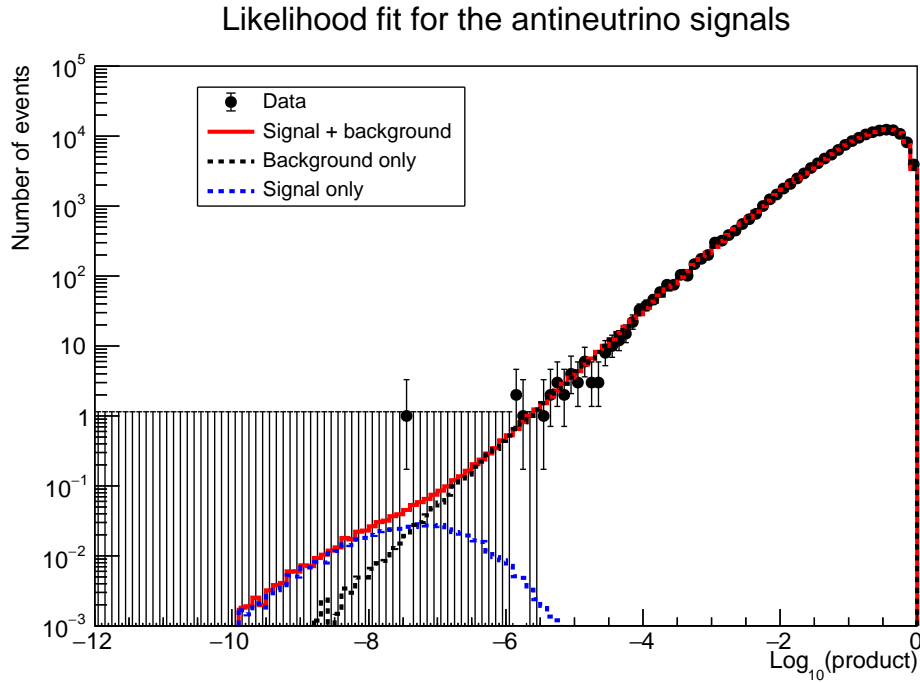


Figure 7.8: The likelihood fit on \mathbf{p} and the profile log-likelihood plot.

The final best fit for the number of signals is $0.609_{-1.134}^{+1.134}$, indicating the result is consistent with the null hypothesis within 1σ significance.

Fig. 7.9 shows the likelihood ratio and its normalized cumulative. The (profile) likelihood ratio is defined as the maximum likelihood as a function of the number of signals divided by its best fit (maximum) value. Also show in the plot is a 1σ upper limit on the number of signals, at 2.134 events. Converting to a rate of reactor antineutrino events that trigger the detector and passes the event selection, this corresponds to 6.78 events/year (1σ C.I.), or 25.2 events/year (3σ C.I.).

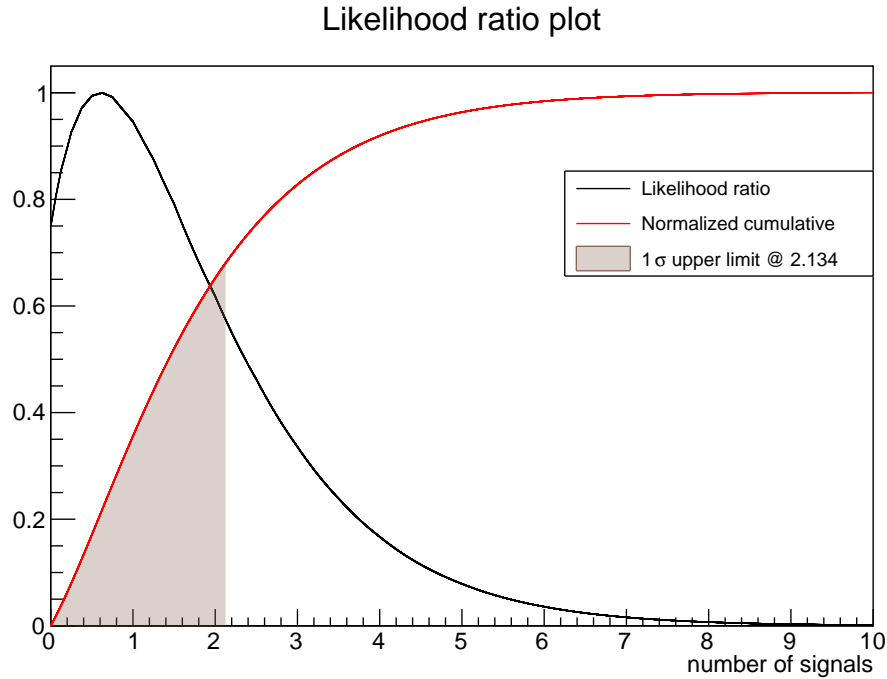


Figure 7.9: The likelihood ratio plot. Overlaid is the normalized cumulative and the 1σ upper limit of 2.13 events for the number of signals observed.

7.6 Systematic Considerations

Thanks to the set up of the likelihood analysis, almost all systematic effects manifest in the shape of the \mathbf{p} distribution for the antineutrino signals, \mathbf{p}_s . Possible sources of systematic effects are:

1. The neutron capture time constant implemented in RAT is found to be $\sim 1\%$ lower than what was measured in the $^{241}\text{Am}^9\text{Be}$ statistical analysis (Section 4.5). This creates a bias towards smaller \mathbf{p} values.
2. Systematics of the antineutrino distance distribution can be estimated from Fig. 5.5, where both neutrons and 4.4 MeV γ s are shown to travel further than

what MC predicts. This affects the distance distribution by less than 2%. It also results in a bias towards smaller \mathbf{p} .

3. The coefficients of the analytical functions of the background time difference and distance distributions have fit errors less than 0.5% and 0.03%, respectively.
4. The time-dependent feature (e.g events tends to cluster close to AV pipes when AV recirculation is on) of background positions is not considered. Local clustering events in a short time period that are overlooked in deriving the background distance distribution will have a bias towards higher \mathbf{p} .
5. Effect of (bin-by-bin) statistical uncertainties in the \mathbf{p}_s distribution.

Because there is no systematic correlation within the likelihood function, the systematic uncertainty can be propagated by running the likelihood fit multiple times with adjusted shapes of \mathbf{p}_s . To derive a conservative estimate, a 10% (the systematic sources discussed above are expected to have an effect of less than 5%) standard Gaussian distributed perturbation is added to each non-zero value bin of \mathbf{p}_s , before \mathbf{p}_s is taken as the signal *p.d.f.* for the likelihood fit. The process is repeated 4000 times to obtain distributions of the best fit value and 1σ upper limit, shown in Fig. 7.10.

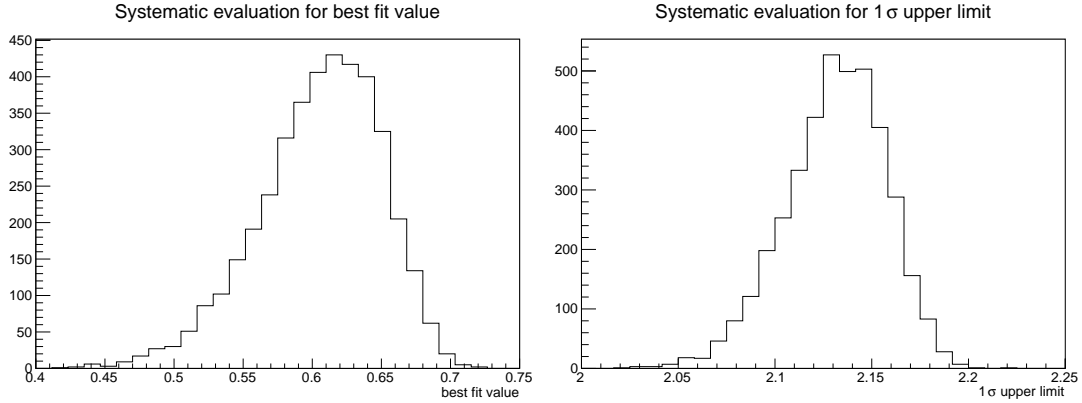


Figure 7.10: Distributions of the best fit value and 1σ upper limit with a 10% perturbation on \mathbf{p}_s . The average and corrected standard deviation of the best fit value and 1σ upper limit are 0.605 ± 0.045 and 2.131 ± 0.026 .

Since the differences between the averaged value and the unperturbed value for both best fit and 1σ upper limit are very small, no systematic correction is needed. The systematic uncertainty is determined to be the corrected standard deviation calculated from the 4000 perturbation test. The final result is given below:

$$\begin{aligned} \text{best fit value} &: 0.61_{-1.13}^{+1.13}(\text{stat.})_{-0.05}^{+0.05}(\text{syst.}), \\ 1\sigma \text{ upper limit} &: 2.13_{-0.03}^{+0.03}. \end{aligned} \tag{7.5}$$

The final results are statistically limited.

One last but not least systematic effect arises from the assumption made when constructing the hypothesis test, that all backgrounds are accidental. However, as captured on ^{18}O emit a time-correlated signal that can be indistinguishable from reactor antineutrino events. Another possible source of coincidence background comes from atmospheric neutrino interactions. While most of them are removed by data cleaning, a small leakage can be significant for the antineutrino analysis. However,

when placing an upper limit on the signal rate or reactor antineutrino flux, it is conservative to assume that these time-correlated background rate to be zero.

7.7 IBD Interaction Rate

An upper limit on the IBD interaction rate can be derived from:

$$R = \frac{s}{\varepsilon t} \quad (7.6)$$

where s is the number of signals, ε is the signal selection probability and t is the detector live time.

ε is determined by passing the antineutrino MC through the selection algorithm and calculating the fraction of remaining antineutrino pairs from those generated, which is found to be $(0.770 \pm 0.104)\%$. Trigger thresholds stand out as the most significant bottleneck, especially in the first 1978 hours of the dataset where trigger thresholds were high. The fraction increases from $(0.594 \pm 0.140)\%$ for the first 1978 hours to $(0.974 \pm 0.150)\%$ after the threshold change. Other significant limiting factors for low selection efficiency include fit validity (reconstruction tends to fail towards low nhits) and a high delayed nhits cut (from data processing).

The fraction passing the selection algorithm is further corrected by a factor associated with the data-MC neutron detection efficiency discrepancy (see Fig. 5.16) to obtain the final selection efficiency ε . The positron detection efficiency does not suffer from this effect because of the prompt energy cut. The final signal survival probability is determined to be $(0.626 \pm 0.095)\%$.

An upper limit on the rate of IBD interactions in SNO+ is given at $(5.51 \pm 0.84) \times 10^{-8}$ event/(cm³·s), or (1083 ± 165) events per year for the full

detector volume. This is approximately a factor of 9 higher than the expected rate ((115 ± 6) event per year) in SNO+ [24].

7.8 Reactor Antineutrino Flux

The reactor antineutrino flux can be related to the rate of IBD interactions in the detector:

$$\begin{aligned} R &= N_p \int \Phi_{\bar{\nu}_e}(E) \sigma(E) dE, \\ &= N_p \hat{\Phi}_{\bar{\nu}_e}(E) \cdot \hat{\sigma}(E), \end{aligned} \quad (7.7)$$

where $N_p = 3.02 \times 10^{32}$ is the number of protons in a 6 m radius AV (the fiducial volume cut is accounted for in the signal survival efficiency). $\hat{\Phi}_{\bar{\nu}_e}$, $\Phi_{\bar{\nu}_e}(E)$, $\hat{\sigma}(E)$ and $\sigma(E)$ are the averaged or energy-dependent fluxes and cross-sections. $\sigma(E)$ is given in Eqn 1.22.

Calculation of $\Phi_{\bar{\nu}_e}(E)$ is complicated as information of the power, distance, $\bar{\nu}_e$ spectrum and time variations of hundreds of reactors needs to be taken into account. An easier option, although double counting the uncertainties, is to calculate an upper limit for the averaged flux, $\hat{\Phi}_{\bar{\nu}_e}$ from the expected rate [107] and flux [108] [24] for SNO+:

$$\hat{\Phi}_{\bar{\nu}_e, \text{ult}} = \frac{R_{\text{ult}}}{R_{\text{SNO+}}} \hat{\Phi}_{\bar{\nu}_e, \text{SNO+}}, \quad (7.8)$$

where R_{expected} and $\hat{\Phi}_{\bar{\nu}_e, \text{expected}}$ are the expected interaction rate and antineutrino flux for the SNO+ detector.

Using Eqn. 7.8, an upper limit for the reactor antineutrino flux is derived to be $(1.76 \pm 0.29) \times 10^6 \bar{\nu}/(\text{cm}^2 \cdot \text{s})$, which is again about a factor of 9 higher than the expected flux of $(1.87 \pm 0.12) \times 10^5 \bar{\nu}/(\text{cm}^2 \cdot \text{s})$.

Chapter 8

Conclusions

An $^{241}\text{Am}^9\text{Be}$ calibration source was deployed in the SNO+ detector both inside and outside of the AV. The internal calibration data was analyzed to measure a few quantities:

- The neutron capture (on proton) time constant:

$$\tau = 202.35 \pm 0.42 \text{ (stat.) } {}^{+0.38}_{-0.31} \text{ (syst.) } \mu\text{s}. \quad (8.1)$$

- The neutron capture (on proton) cross-section:

$$\sigma_{H,t} = 336.3 {}^{+1.2}_{-1.5} \text{ mb}, \quad (8.2)$$

which is the third most accurate measurement to date with a different methodology from previous dedicated measurements.

- The neutron detection efficiency at the center of the detector:

$$E_{\text{center}} = (50.8 \pm 0.6)\%, \quad (8.3)$$

where the uncertainty includes both statistical and systematic effects. And,

- The volume-averaged neutron detection efficiency for SNO+ (6 m radius):

$$E_{\text{detector}} = (46.5 \pm 0.5 \text{ (stat. only)})\%, \quad (8.4)$$

which is the highest neutron detection efficiency for pure water Cherenkov detectors to date. It is also the first detection of neutrons in pure water Cherenkov detectors with continuous triggers.

- The energy resolution at the center of the detector:

$$\begin{aligned} \sigma(E) &= b \cdot \sqrt{E}, \text{ where} \\ b &= 0.44 \pm 0.04 \text{ (stat. only)}, \end{aligned} \quad (8.5)$$

and,

- The relative energy scale at the center of the detector:

$$\delta_E = 0.13 \pm 0.02 \text{ (stat. only)}. \quad (8.6)$$

Additionally, an attempt to search for the reactor antineutrinos resulted in an upper limit on the antineutrino flux for SNO+:

$$\hat{\Phi}_{\bar{\nu}_e, \text{ult}} = (1.76 \pm 0.29) \times 10^6 \bar{\nu}/(\text{cm}^2 \cdot \text{s}), \quad (8.7)$$

which is a factor of ~ 9 higher than what is actually expected.

Bibliography

- [1] W Pauli. Address to the group on radioactivity. *Tübingen, Germany*, 4:324, 1930. unpublished.
- [2] W Pauli. Rapports du septieme conseil de physique solvay. *Brussels (Gauthier Villars, Paris, 1934)*, 1933.
- [3] F Reines and CL Cowan Jr. A proposed experiment to detect the free neutrino. *Physical Review*, 90(3):492, 1953.
- [4] G Danby, JM Gaillard, K Goulianos, LM Lederman, N Mistry, M Schwartz, and J Steinberger. Observation of high-energy neutrino reactions and the existence of two kinds of neutrinos. *Physical Review Letters*, 9(1):36, 1962.
- [5] DONUT Collaboration. Observation of tau neutrino interactions. *Physics Letters B*, 504(3):218–224, 2001.
- [6] Super-Kamiokande Collaboration. Evidence for oscillation of atmospheric neutrinos. *Physical Review Letters*, 81(8):1562, 1998.
- [7] SNO Collaboration. Measurement of the rate of $\nu_e + d \rightarrow p + p + e^-$ interactions produced by ^8B solar neutrinos at the Sudbury Neutrino Observatory. *Physical Review Letters*, 87(7):071301, 2001.

-
- [8] Troitsk Collaboration. Upper limit on the electron antineutrino mass from the Troitsk experiment. *Physical Review D*, 84(11):112003, 2011.
- [9] Planck Collaboration. Planck 2015 results-xiii. cosmological parameters. *Astronomy & Astrophysics*, 594:A13, 2016.
- [10] F Reines. The early days of experimental neutrino physics. *Science*, 203(4375):11–16, 1979.
- [11] KamLAND Collaboration. First results from KamLAND: evidence for reactor antineutrino disappearance. *Physical Review Letters*, 90(2):021802, 2003.
- [12] YF Li, J Cao, Y Wang, and L Zhan. Unambiguous determination of the neutrino mass hierarchy using reactor neutrinos. *Physical Review D*, 88(1):013008, 2013.
- [13] AC Hayes and P Vogel. Reactor neutrino spectra. *Annual Review of Nuclear and Particle Science*, 66:219–244, 2016.
- [14] AA Hahn, K Schreckenbach, W Gelletly, F Von Feilitzsch, G Colvin, and B Krusche. Antineutrino spectra from ^{241}Pu and ^{239}Pu thermal neutron fission products. *Physics Letters B*, 218(3):365–368, 1989.
- [15] P Vogel, GK Schenter, FM Mann, and RE Schenter. Reactor antineutrino spectra and their application to antineutrino-induced reactions. ii. *Physical Review C*, 24(4):1543, 1981.
- [16] Particle Data Group. Review of particle physics. *Phys. Rev. D*, 98:030001, 2018.

- [17] G. Mention et al. The Reactor Antineutrino Anomaly. *Phys. Rev. D*, 83:073006, 2011.
- [18] C Giganti, S Lavignac, and M Zito. Neutrino oscillations: the rise of the PMNS paradigm. *Prog. Part. Nucl. Phys.*, 98:1–54, 2018.
- [19] C. Giunti, CW Kim, and UW Lee. When do neutrinos really oscillate? quantum mechanics of neutrino oscillations. *Phys. Rev. D*, 44:3635–3640, Dec 1991.
- [20] YL Chan, MC Chu, K Tsui, C Wong, and J Xu. Wave-packet treatment of reactor neutrino oscillation experiments and its implications on determining the neutrino mass hierarchy. *The European Physical Journal C*, 76, 06 2016.
- [21] V Barger, K Whisnant, and RJN Phillips. Three-neutrino oscillations and present experimental data. *Physical Review D*, 22(7):1636, 1980.
- [22] MUNU Collaboration. The MUNU experiment, general description. *Nuclear Instruments and Methods in Physics Research Section A: Accelerators, Spectrometers, Detectors and Associated Equipment*, 396(1-2):115–129, 1997.
- [23] AG Beda, VB Brudanin, VG Egorov, DV Medvedev, MV Shirchenko, and AS Starostin. GEMMA experiment: Three years of the search for the neutrino magnetic moment. *Physics of Particles and Nuclei Letters*, 7(6):406–409, 2010.
- [24] P Mekariski. *Electron Antineutrinos in the water Phase of the SNO+ experiment*. PhD thesis, University of Alberta, 2018.
- [25] SNO+ Collaboration. Current status and future prospects of the SNO+ experiment. *Advances in High Energy Physics*, 2016, 2016.

- [26] IAEA. IAEA website. <https://www.iaea.org/>, accessed on 2019-09-14.
- [27] Particle Data Group. Review of particle physics. *Chin. Phys.*, 40:100001, 2016.
- [28] Super-Kamiokande Collaboration. Solar neutrino measurements in Super-Kamiokande-IV. *Physical Review D*, 94(5):052010, 2016.
- [29] KamLAND Collaboration. Precision measurement of neutrino oscillation parameters with KamLAND. *Physical Review Letters*, 100(22):221803, 2008.
- [30] KamLAND Collaboration. Reactor on-off antineutrino measurement with KamLAND. *Physical Review D*, 88(3):033001, 2013.
- [31] M Chen. The SNO+ Experiment. In *Proceedings, 34th International Conference on High Energy Physics (ICHEP 2008): Philadelphia, Pennsylvania, July 30-August 5, 2008*, 2008.
- [32] A Bialek, M Chen, B Cleveland, P Gorel, A Hallin, PJ Harvey, J Heise, C Kraus, CB Krauss, I Lawson, et al. A rope-net support system for the liquid scintillator detector for the SNO+ experiment. *Nuclear Instruments and Methods in Physics Research Section A: Accelerators, Spectrometers, Detectors and Associated Equipment*, 827:152–160, 2016.
- [33] R Alves et al. The calibration system for the photomultiplier array of the SNO+ experiment. *JINST*, 10(03):P03002, 2015.
- [34] SNO+ Collaboration. Search for invisible modes of nucleon decay in water with the SNO+ detector. *Physical Review D*, 99(3):032008, 2019.

- [35] SNO+ Collaboration. Measurement of the ^8B solar neutrino flux in SNO+ with very low backgrounds. *Physical Review D*, 99(1):012012, 2019.
- [36] M Depatie. AV camera photos - Oct 18 2018. SNO+ internal document, DocDB5417, 2018.
- [37] F Capozzi, E Lisi, A Marrone, and A Palazzo. Current unknowns in the three-neutrino framework. *Progress in Particle and Nuclear Physics*, 102:48–72, 2018.
- [38] PF de Salas, DV Forero, CA Ternes, M Tortola, and JWF Valle. Status of neutrino oscillations 2018: 3σ hint for normal mass ordering and improved cp sensitivity. *Physics Letters B*, 782:633–640, 2018.
- [39] I Esteban, MC Gonzalez-Garcia, A Hernandez-Cabezudo, M Maltoni, and T Schwetz. Global analysis of three-flavour neutrino oscillations: synergies and tensions in the determination of θ_{23} , δ_{CP} , and the mass ordering. *Journal of High Energy Physics*, 2019(1):106, 2019.
- [40] GS Smith. Human color vision and the unsaturated blue color of the daytime sky. *American Journal of Physics*, 73(7):590–597, 2005.
- [41] CJ Jillings, RJ Ford, AL Hallin, PJ Harvey, RW MacLeod, HB Mak, P Skensved, and RL Stevenson. The photomultiplier tube testing facility for the Sudbury Neutrino Observatory. *Nuclear Instruments and Methods in Physics Research Section A: Accelerators, Spectrometers, Detectors and Associated Equipment*, 373(3):421–429, 1996.
- [42] F Duncan, P Harvey, and P Skensved. *SNO calibration operator manual*, 2 edition, 2017.

- [43] A LaTorre. Measurement of the trigger efficiency in SNO+. SNO+ internal document, DocDB4723, 2017.
- [44] J Maneira. URM design for SNO+ by LIP-Coimbra. SNO+ internal document, DocDB1949, 2019.
- [45] C Holmberg. Side rope motor boxes. SNO+ internal document, DocDB1645, 2012.
- [46] B.A. Moffat, R.J. Ford, F.A. Duncan, K. Graham, A.L. Hallin, C.A.W. Hearn, J. Maneira, P. Skensved, and D.R. Grant. Optical calibration hardware for the sudbury neutrino observatory. *Nucl. Instrum. Meth. A*, 554:255–265, 2005.
- [47] M.R. Dragowsky et al. The N-16 calibration source for the Sudbury Neutrino Observatory. *Nucl. Instrum. Meth. A*, 481:284–296, 2002.
- [48] Z Barnard. Update to N16 geometry. SNO+ internal document, DocDB4414, 2017.
- [49] F Descamps et al. Cherenkov source review. SNO+ internal document, DocDB3492, 2018.
- [50] GEANT4 Collaboration. GEANT4—a simulation toolkit. *Nuclear instruments and methods in physics research section A: Accelerators, Spectrometers, Detectors and Associated Equipment*, 506(3):250–303, 2003.
- [51] R Brun and F Rademakers. ROOT—an object oriented data analysis framework. *Nuclear Instruments and Methods in Physics Research Section A: Accelerators, Spectrometers, Detectors and Associated Equipment*, 389(1-2):81–86, 1997.

- [52] G Horton-Smith et al. Introduction to GLG4sim, 2006. <https://www.phys.ksu.edu/personal/gahs/GLG4sim/GLG4sim-intro-2006-05-19.pdf>, accessed on 2019-09-14.
- [53] R Brun, F Carminati, and G Galli-Carminati. *From the Web to the Grid and Beyond: Computing Paradigms Driven by High-Energy Physics*. Springer., 2012.
- [54] KW Geiger and L Van der Zwan. Radioactive neutron source spectra from ${}^9\text{Be}$ (α , n) cross section data. *Nuclear Instruments and Methods*, 131(2):315–321, 1975.
- [55] S Croft. The use of neutron intensity calibrated ${}^9\text{Be}$ (α , n) sources as 4438 keV gamma-ray reference standards. *Nuclear Instruments and Methods in Physics Research Section A: Accelerators, Spectrometers, Detectors and Associated Equipment*, 281(1):103–116, 1989.
- [56] Y Liu, B Krar, and P Skensved. Review package for the AmBe source. SNO+ internal document, DocDB4725, 2018.
- [57] K Galipeau. SNOLAB sources inventory. SNOLAB internal document, 2019.
- [58] K Galipeau. SNOLAB radiological source encapsulation policy. SNOLAB internal document, 2018.
- [59] J Loach. *Measurement of the flux of ${}^8\text{B}$ solar neutrinos at the sudbury neutrino observatory*. PhD thesis, University of Oxford, 2008.
- [60] C Lin. AmBe source encapsulation for scintillator phase. SNO+ internal document, DocDB5768, 2019.

- [61] Federal Aviation Administration. Acceptable methods, techniques, and practices aircraft inspection and repair, 1998.
- [62] Alconox Inc. Alconox website. <https://alconox.com/alconox/>, accessed on 2019-09-14.
- [63] Gamma Gurus Inc. Radiac wash website. <https://gammagurus.com/products/radiacwash>, accessed on 2019-09-14.
- [64] Y Liu. Final AmBe source run plan. SNO+ internal document, DocDB4771, 2018.
- [65] A LaTorre. Private communication. email, 2018.
- [66] Y Liu and S Andringa. Proposal for the AmBe external calibration in the SNO+ water phase. SNO+ internal document, DocDB5868, 2018.
- [67] Super-Kamiokande Collaboration. Supernova relic neutrino search with neutron tagging at Super-Kamiokande-iv. *Astroparticle Physics*, 60:41, 2015.
- [68] Super-Kamiokande Collaboration. First measurement of radioactive isotope production through cosmic-ray muon spallation in Super-Kamiokande IV. *Physical Review D*, 93(1):012004, 2016.
- [69] Y Zhang. The write-up of n-tag. SNO+ internal document, DocDB5535, 2019.
- [70] R Heaton, H Lee, P Skensved, and BC Robertson. Neutron production from thick-target (α , n) reactions. *Nuclear Instruments and Methods in Physics Research Section A: Accelerators, Spectrometers, Detectors and Associated Equipment*, 276(3):529–538, 1989.

-
- [71] S Nae. Water-phase alpha-n analysis. SNO+ internal document, DocDB5774, 2019.
- [72] A Li. Ambe data nhit burst cut. SNO+ internal document, DocDB5403, 2018.
- [73] SNO+ Water Physics Group. Water physics unidoc v2.1.0. SNO+ internal document, 2019.
- [74] T Pershing. Neutron data cleaning sacrifice estimates - values and plots. SNO+ internal document, DocDB5540, 2019.
- [75] T Pershing. Update on neutron sacrifice calculation for AmBe calibration. SNO+ internal document, DocDB5530, 2019.
- [76] R Heaton. Neutron shielding calculations for the SNO detector. Master's thesis, Queen's University, 1988.
- [77] Y Zhang. Thermal neutron physics: capture life time vs temperature. SNO+ internal document, DocDB5467, 2019.
- [78] Engineering ToolBox. Water - density, specific weight and thermal expansion coefficient, 2003.
- [79] SNO+ Collaboration. Cavity temperature monitoring webpage. SNO+ internal document, 2017.
- [80] MB Chadwick et al. Endf/b-vii.0: next generation evaluated nuclear data library for nuclear science and technology. *Nuclear Data Sheets*, 107:2931–3060, 2006.

- [81] A.E. Cox, S.A.B. Wynchank, and Collie C.H. The proton-thermal neutron capture cross section. *Nuclear Physics*, 74:497–507, 1965.
- [82] D Cokinos and E Melkonian. Measurement of the 2200 m/sec neutron-proton capture cross section. *Phys. Rev. C*, 15:1636–1643, 1977.
- [83] D.A. Brown et al. Endf/b-viii.0: The 8th major release of the nuclear reaction data library with CIELO-project cross sections, new standards and thermal scattering data. *Nucl. Data Sheets*, 148:1–142, 2018.
- [84] K Singh, P Gorel, et al. Underwater photometry system of the SNO+ experiment. *J. Phys. Conf. Ser.*, 1342(1):012130, 2020.
- [85] P Skensved. Private communication. email, 2018.
- [86] M Stringer. Z position of the AV relative to the PSUP. SNO+ internal document, DocDB4742, 2017.
- [87] P Khaghani. AV position and tuning the neck sense ropes. SNO+ internal document, DocDB5955, 2019.
- [88] M Nirikko. AmBe simulations for scintillator phase. SNO+ internal document, DocDB4896, 2018.
- [89] M Boulay. *Direct evidence for weak flavour mixing with the Sudbury Neutrino Observatory*. PhD thesis, Queen’s University, 2001.
- [90] R MacLellan. RSP for the NCD phase. SNO technical report, 2007.
- [91] J Dunmore. *The separation of CC and NC events in the Sudbury Neutrino Observatory*. PhD thesis, University of Oxford, 2004.

-
- [92] L Lebanowski and M Luo. Brief look at ITR and beta14 inside and outside the AV. SNO+ internal document, DocDB5359, 2018.
- [93] R Bayes. Beta14 and G4 electron step size. SNO+ internal document, DocDB5471, 2019.
- [94] Y Zhang. A summary of beta14 tuning. SNO+ internal document, DocDB5629, 2019.
- [95] T Kaptanoglu. Trigger model in RAT. SNO+ internal document, DocDB5430, 2018.
- [96] R Bayes. Global calibration analysis. SNO+ internal document, DocDB5907, 2019.
- [97] S Nae. Data processing for coincidence analyses. SNO+ internal document, DocDB5151, 2018.
- [98] M Dunford. *Measurement of the 8B solar neutrino energy spectrum at the sudbury neutrino observatory*. PhD thesis, University of Pennsylvania, 2006.
- [99] L Lebanowski and M Luo. Sno+ calibration with the N16 source. SNO+ internal document, DocDB5003, 2018.
- [100] K Singh. AmBe source in water phase. SNO+ internal document, DocDB3286, 2016.
- [101] Z Yang. Sensitivity on reactor nu search. SNO+ internal document, DocDB6219, 2020.

-
- [102] T Kaptanoglu. Selecting antineutrino candidates using a likelihood approach. SNO+ internal document, DocDB5793, 2019.
- [103] S Nae. Water-phase reactor antineutrino analysis. SNO+ internal document, DocDB5816, 2019.
- [104] V Lozza. Physics lists for ND analysis. SNO+ internal document, DocDB4820, 2018.
- [105] E Falk. Data quality and run selection. SNO+ internal document, DocDB5136, 2018.
- [106] MG Kendall and PAP Moran. *Geometrical Probability*. Charles Griffin And Company Limited., 1963.
- [107] S Asahi. Expected number of antineutrino events at SNO+. SNO+ internal document, DocDB3763, 2016.
- [108] S Asahi. Reactor neutrino flux uncertainties. SNO+ internal document, DocDB2944, 2015.
- [109] McMaster-Carr Supply Company. Engineering drawing, 2015.

Appendix A

Drawings for Parts Used in the $^{241}\text{Am}^9\text{Be}$ Encapsulation

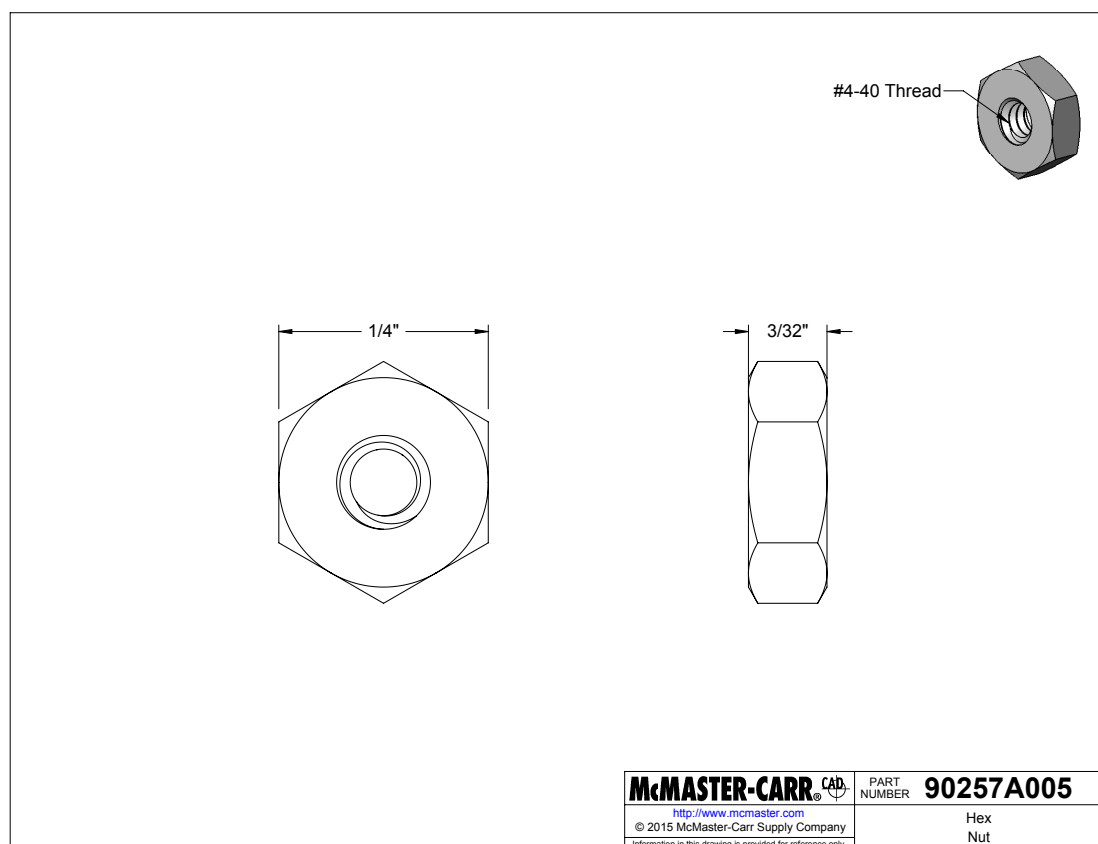


Figure A.1: Drawing of the nuts (part no. 90257A005) used in the new encapsulation for the $^{241}\text{Am}^9\text{Be}$ source. Figure is from [109].

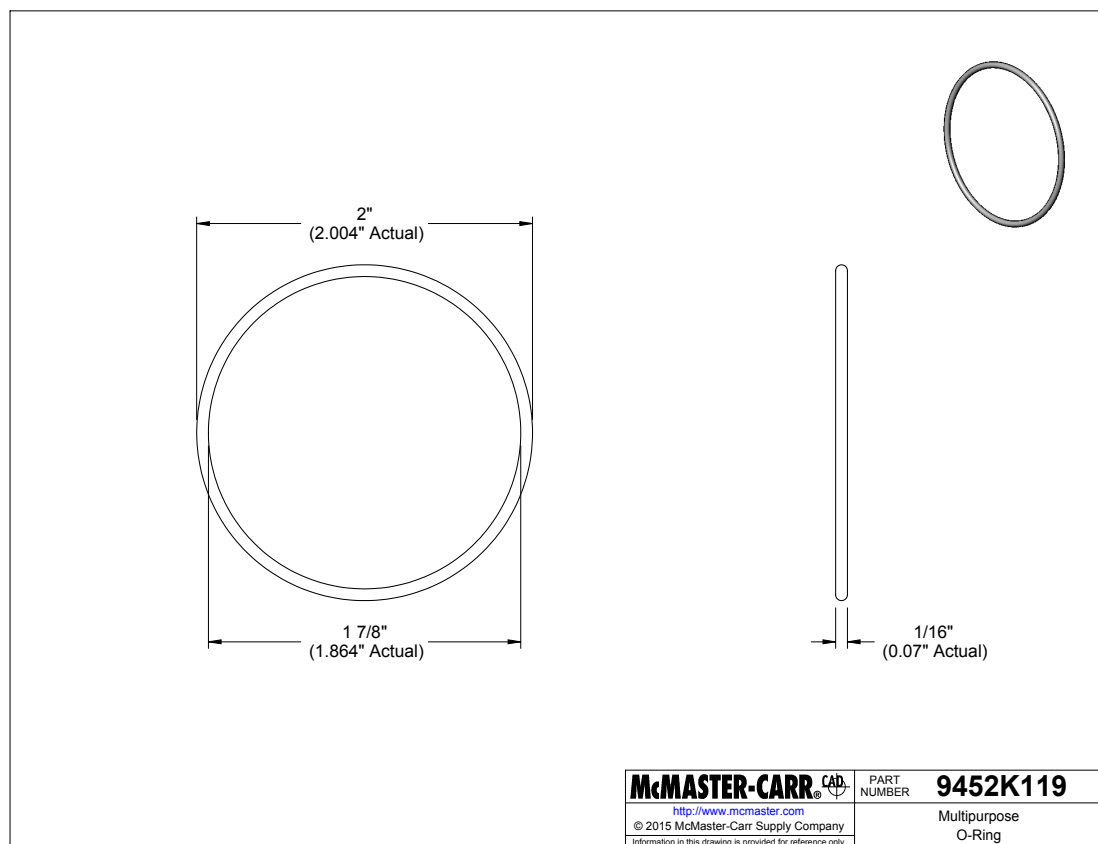


Figure A.2: Drawing of the O-ring (part no. 9452K119) used in the new encapsulation for the $^{241}\text{Am}^9\text{Be}$ source. Figure is from [109].

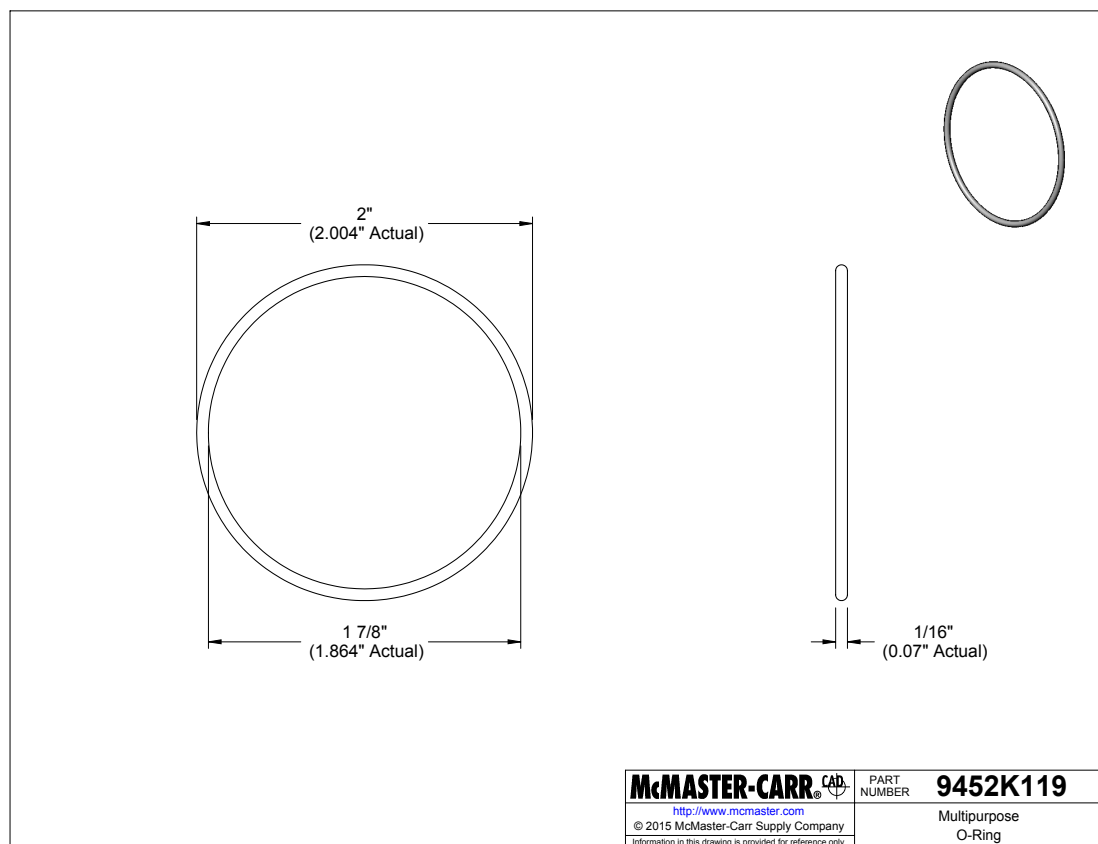


Figure A.3: Drawing of the O-ring (part no. 90152A116) used in the new encapsulation for the $^{241}\text{Am}^9\text{Be}$ source. Figure is from [109].

Appendix B

Acronyms

ΛCDM	Lambda Cold Dark Matter
ADC	Analog to Digital Converter
AV	Acrylic Vessel
BWR	Boiling Water Reactor
CANDU	CANada Deuterium Uranium
ECA	Electronics CALibration
ELLIE	Embedded LED/Laser Light Injection En- tity
DCR	Deck Clean Room
IBD	Inverse Beta Decay
ITR	In Time Ratio
LAB	Linear Alkylbenzene

MTC	Master Trigger Card
nhits	number of PMT hits of an event
OCA	Optical CALibration
PCA	PMT CALibration
PMT	PhotoMultiplier Tube
PSUP	PMT SUPport structure
PWR	Pressurized Water Reactor
RAT	Reactor Analysis Tools
RATDB	RAT DataBase
UI	Universal Interface
UPW	Ultra Pure Water
URM	Umbilical Retrieval Mechanism
ZDAB	ZEBRA Data Analysis Banks